TECHNICAL REPORT CERC-85-5

**US Army Corps of Engineers**

AN INVESTIGATION OF HURRICANE-INDUCED FORERUNNER SURGE IN THE GULF OF MEXICO

by

Mahunnop Bunpapong, Robert O. Reid
Robert E. Whitaker

Department of Oceanography
Texas A&M University
College Station, Texas 77843

September 1985
Final Report

Approved For Public Release; Distribution Unlimited

TECHNICAL REPORT CERC-85-5

AN INVESTIGATION OF HURRICANE-INDUCED FORERUNNER SURGE IN THE GULF OF MEXICO

by

Mahunnop Bunpapong, Robert O. Reid
Robert E. Whitaker

Department of Oceanography
Texas A&M University
College Station, Texas 77843

US Army Corps of Engineers

September 1985
Final Report

Approved For Public Release; Distribution Unlimited
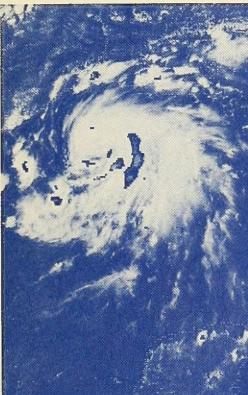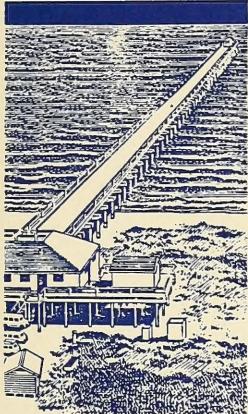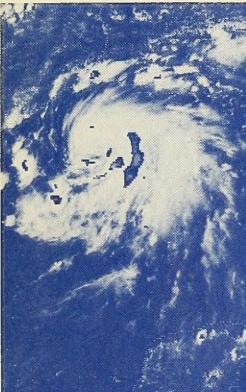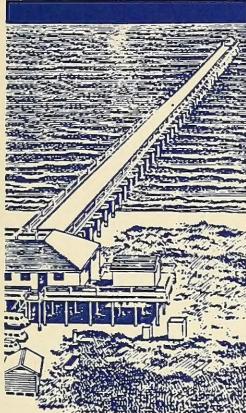
REPORT DOCUMENTATION PAGE		READ INSTRUCTIONS BEFORE COMPLETING FORM
1. REPORT NUMBER Technical Report CERC-85-5	2. GOVT ACCESSION NO.	3. RECIPIENT'S CATALOG NUMBER
4. TITLE *(and Subtitle)* AN INVESTIGATION OF HURRICANE-INDUCED FORERUNNER SURGE IN THE GULF OF MEXICO		5. TYPE OF REPORT & PERIOD COVERED Final report
		6. PERFORMING ORG. REPORT NUMBER
7. AUTHOR(s) Mahunnop Bunpapong, Robert O. Reid, Robert E. Whitaker		8. CONTRACT OR GRANT NUMBER(s) Contract No. DACW39-82-K-0001
9. PERFORMING ORGANIZATION NAME AND ADDRESS Department of Oceanography Texas A&M University College Station, Texas 77843		10. PROGRAM ELEMENT, PROJECT, TASK AREA & WORK UNIT NUMBERS
11. CONTROLLING OFFICE NAME AND ADDRESS DEPARTMENT OF THE ARMY US Army Corps of Engineers Washington, DC 20314-1000		12. REPORT DATE September 1985
		13. NUMBER OF PAGES 217
14. MONITORING AGENCY NAME & ADDRESS(*if different from Controlling Office*) US Army Engineer Waterways Experiment Station Coastal Engineering Research Center PO Box 631, Vicksburg, Mississippi 39180-0631		15. SECURITY CLASS. *(of this report)* Unclassified
		15a. DECLASSIFICATION/DOWNGRADING SCHEDULE

16. DISTRIBUTION STATEMENT *(of this Report)*

Approved for public release; distribution unlimited.

17. DISTRIBUTION STATEMENT *(of the abstract entered in Block 20, if different from Report)*

18. SUPPLEMENTARY NOTES

Available from National Technical Information Service, 5285 Port Royal Road, Springfield, Virginia 22161.

19. KEY WORDS *(Continue on reverse side if necessary and identify by block number)*

Storm surges--Mathematical Models (LC)
Storm surges--Gulf of Mexico (LC)

20. ABSTRACT *(Continue on reverse side if necessary and identify by block number)*

A system of coupled, normal mode equations describing a two-layer ocean basin of variable depth was derived from the quasi-hydrostatic equations of motion using a general form of the method of Veronis and Stommel (1956). A finite difference, time marching, numerical model for the normal mode equations, employing an Alternating Direction Implicit (ADI) scheme, on a space-staggered grid has been developed. The model is quasi-linear and allows for
(Continued)

DD FORM 1473 EDITION OF 1 NOV 65 IS OBSOLETE
1 JAN 73

20. ABSTRACT (Continued).

variable bathymetry and variable Coriolis parameter. The model domain in-
cludes the Gulf of Mexico and the Cayman Sea with a resolution of 15'. A no-
flow condition is taken at all solid boundaries and the inverted barometer
term is used to stipulate barotropic height anomalies on the open boundaries.
Hurricanes Carla (1961) and Allen (1980) are used as historical storms to
verify the model by comparing numerical and observed hydrographs.

A parametric study utilizing three forward speeds, two radii to maximum
winds, and five paths characterizing Gulf hurricanes is presented. The
results of the study show that volume transports through Florida and Yucatan
Straits consisted of in-phase (both in or both out) and out-of-phase com-
ponents. The in-phase volume transport excites a volume mode, η_G , in the
Gulf of Mexico having periods of about 28 h and 3.4 days. The η_G mode of
oscillation can produce a forerunner surge for many storm tracks. Although
all the model storms generated η_G , not all had an associated positive
forerunner. The hurricane path and evolution play important roles in gener-
ating a forerunner.

The out-of-phase volume transport through the ports was found to produce
a Gulf-wide quasi-geostrophic tilt mode of about 6.5-day period. Surges
on the shelf including the forerunner are primarily a barotropic response.
The quasi-linear model transmitted only a fraction of the baroclinic energy
onto the shelf.

Results of a limited area model (no wind in deep water) showed that
either wind or pressure forcing generates η_G . The limited area model
simulations also demonstrate clearly that the use of a simple inverted
barometer boundary condition at the shelf break will always underestimate
the peak surge at the coast.

This study was conducted by the Department of Oceanography at Texas A&M University, Reference 85-2-T. The research was conducted through Texas A&M Research Foundation Project 4667.

This study was motivated by the fact that existing storm surge models which are generally restricted to a limited reach of the continental shelf do not adequately simulate the forerunner surge. In the Gulf of Mexico the forerunner stage of a surge event (which can have an amplitude as large as 1 m) can precede the peak surge by more than 24 hours.

It is common practice, in employing coastal surge models for design purposes, to start computations with an initial non-zero constant water level field over the shelf in recognition of the influence of forerunners. This procedure makes no allowance for initial flows or gradient thereof which must exist during the forerunner stage. On the other hand, starting local coastal models well in advance of the arrival of the hurricane at the shelf break cannot simulate the forerunner surge since the latter is ex-cited by mechanisms acting over the adjacent deep basin seaward of the coastal zone being modeled.

The objectives of this research were to determine for the Gulf of Mexico the space and time scales of forerunners, examine possible excita-tion processes, and evaluate the role of baroclinic modes in surge events at the coast and shelf break. A numerical approach was used in this study which modeled hurricane-forced responses of the barotropic and first baro-clinic modes over a computing domain representing the Northwest Cayman Sea and Gulf of Mexico. The inclusion of the baroclinic response adds a degree of realism lacking in previous studies on hurricane effects in the Gulf of Mexico.

It should be stressed that the model includes only wind and atmospheric pressure forcing. Tidal forcing was not included. Moreover, the model is quasi-linear (only the bottom and interface stresses are nonlinear). The model was verified by simulating the Gulf's response to hurricanes Carla and Allen. Although the focus of the study was on forerunner surge events, the results also provide insight into fundamental concepts concerning the large-scale, low-frequency free modes in the Gulf of Mexico and Cayman Sea.

This study also constitutes the doctoral dissertation research of one of the authors, Mahunnop Bunpapong.

TABLE OF CONTENTS

LIST OF FIGURES

LIST OF TABLES

CHAPTER I

INTRODUCTION

1. Background

Redfield and Miller (1957) considered the changes in water level
associated with hurricanes as consisting of three successive stages;
the forerunner surge, the hurricane surge and the resurgence. The
forerunner surge is the gradual rise in water level along the coast
which precedes the arrival of the hurricane. It occurs while the
storm center is at a great distance from the coast, irrespective of
whether the storm reaches the point of observation. The gradual
buildup of water level may reach one meter. This may seem
unimportant in a destructive sense when compared to the hurricane
surge itself, but it is an important initial boundary condition for
local storm surge models.

The salient feature of forerunners is that local atmospheric
forcing is not required for this phase of the surge. Cline (1920)
reported the existence of forerunner surges in the Gulf of Mexico.
He analyzed water levels and winds associated with hurricanes from
the 1900-1919 period and found that some storms clearly produced
increasing sea level within 24 h of the disturbance entering the
Gulf. Cline postulated that forerunners are related to swell
generated by Gulf hurricanes. Based on a simple wind model, Cline
showed that the storm generated swell (forerunner) would be
significant only in the direction of the hurricane motion. The data
presented by Cline, however, suggest the nearly simultaneous

1

appearance of forerunners over a long stretch of the United States Gulf coast.

Forerunners in a basin like the Gulf of Mexico may be explained in terms of the large scale barotropic normal gravity modes of the Gulf. Even though the Gulf is relatively small, the size of hurricanes still gives a mismatch of forcing and response scales. However, normal mode excitation is not limited to open ocean atmospheric forcing in the Gulf of Mexico. Platzman (1972) obtained a long-period Helmholtz mode of 21.2 h in a numerical study of the Gulf. Reid and Whitaker (1981) also obtained a Helmholtz mode for the Gulf, but with a period of 28.5 h. This mode is characterized by nearly uniform phase and amplitude, except near the ports.[1] This is indicative of a co-oscillating port-driven Gulf-Caribbean system. Conceivably, some hurricanes could provide port forcing to elicit this long period motion.

Another possible large scale barotropic response of the Gulf to hurricane forcing typically has relatively small surface expressions but large vorticity (circulation). These are the vorticity modes generated by planetary or topographic vortex stretching and they have been observed in enclosed basins. Saylor et. al (1980) found that the observed oscillation in Southern Lake Michigan with a period of 4 days was a lake-wide barotropic topographic vortex mode. Calculations show that if the response of the Gulf of Mexico to a hurricane was a Gulf-wide barotropic vortex mode it would have a period of about 5 days. Muller and Frankignoul (1981) however, showed that realistic topography causes the vorticity modes to have

---

[1] The term "ports" denotes the model representation of the Yucatan and Florida Straits.

smaller space scales compared to the gravity modes.

The development of forerunners in the Gulf might be caused by the strong baroclinic response of the sea to hurricane winds. Stevenson and Armstrong (1965) and Leipper (1967) presented descriptions of hurricane induced upwelling in the Gulf and provided qualitative depictions of the causative mechanisms. Oceanic baroclinic responses to hurricane forcing have been the subject of numerous theoretical and numerical investigations (Ichiye, 1955). In addition, Veronis and Stommel (1956) speculated that a two-layer ocean with constant depth would exhibit a baroclinic response to a distant storm. However, changes in the interface elevation would be small provided that there were no other effects such as resonance. The only noticeable effect would be changes in the free surface anomaly contributed by barotropic Rossby waves.

The single study on forerunner surges in the Gulf by Cline (1920) leaves several fundamental questions unanswered. It is not clear that all hurricanes traversing the Gulf generate forerunners. If not, under which conditions are forerunners excited? What are the time and space scales of forerunners? Conflicting evidence suggests both local and Gulf wide occurrences. Finally, are forerunners barotropic or baroclinic in origin? To date, only the barotropic response on the perimeter of the Gulf to hurricane forcing has been sufficiently studied.

As already pointed out, the forerunner questions are important in establishing *initial* conditions in hurricane surge prediction at the coastline. Most hurricane surge models employ limited area

domains, namely a section of the continental shelf extending from shore to the shelf break at about the 200 m depth contour and extending several hundred kilometers along shore on either side of the coastal location for which surge prediction is sought. A second problem with such models is that of specifying appropriate boundary conditions at the open boundaries, particularly along the seaward shelf break positions. A common seaward boundary condition is to set the water level along the shelf break equal to the static barometrically-induced anomaly appropriate to the position relative to the hurricane center. However, this ignores any dynamically-induced water level anomaly by the storm in the deep region of the sea or Gulf.

2. Objectives

There are three objectives of this research effort. First, the investigation is directed toward establishing the cause as well as the time and space scales of forerunners in the Gulf of Mexico. Second, the relation between hurricane generated barotropic and baroclinic modes and forerunners is sought. Third, the clarification of conditions at the shelf break is addressed. All of these objectives will be carried out within the framework of a basin wide model which includes the Gulf of Mexico and the Cayman Sea.

3. Procedure

As a result of uncertainty in the type of response, it is prudent to include the effect of density stratification in the formulation of the problem. To allow for the first baroclinic mode in the solutions, a two-layer model with variable depth was chosen. An analytic approach to the problem of hurricane forcing in a basin with realistic bathymetry and shape is not possible. Therefore, a numerical approach was used in this study. An existing linear numerical model for astronomical tides in the Gulf of Mexico ,GOMT, (c.f. Reid and Whitaker, 1981) was adapted to include both the barotropic and baroclinic computations and atmospheric forcing. Information obtained from the numerical model, which is usually unavailable from the recorded data, allows a detailed investigation of the dynamics and other characteristics of the response. Another important advantage of the numerical model is its predictive capability.

Instead of using the primitive equations describing the two-layer system, normal mode equations were derived using a generalization of the method employed by Veronis and Stommel (1956). There are several advantages in working with the modal form of the equations. In this system the dynamics and energetics of each mode can be examined separately. Interaction between modes, due to coupling caused by varying depth, can be investigated in terms of energy transfer. Open boundary conditions are facilitated in terms of the modes, particularly if outward radiation of wave energy is allowed. In addition, the layer variables such as the free surface

and interface anomalies can be easily retrieved from the modal variables. Therefore, analyses can be made both in terms of layers and modes.

CHAPTER II

THEORETICAL AND NUMERICAL MODEL

1. Theoretical model

a) Basic equations

The vertically integrated momentum and mass conservation
equations for quasi-hydrostatic (large scale) disturbances in a two-
layer variable depth basin are, for the upper layer,

$$\partial\vec{M_1}/\partial t + f\vec{k}\times\vec{M_1} + \rho_1 gH_1\nabla(h_1+h_2) = \vec{F_1}, \tag{1}$$

$$\rho_1\ \partial h_1/\partial t + \nabla\cdot\vec{M_1} = 0, \tag{2}$$

and for the lower layer,

$$\partial\vec{M_2}/\partial t + f\vec{k}\times\vec{M_2} + gH_2\nabla(\rho_1 h_1+\rho_2 h_2) = \vec{F_2}, \tag{3}$$

$$\rho_2\ \partial h_2/\partial t + \nabla\cdot\vec{M_2} = 0, \tag{4}$$

where $\vec{M}$ is the mass transport per unit width, f is the Coriolis
parameter, $\vec{k}$ is the vertical unit vector, ρ is the water density,
g is the gravitational acceleration, H is the mean depth, H+h is the
instantaneous depth, $\vec{F}$ is the external forcing and dissipation
defined as:

$$\vec{F_1} = \vec{\tau}_s - \vec{\tau}_i - H_1\nabla P_a,$$

$$\tag{5}$$

$$\vec{F_2} = \vec{\tau}_i - \vec{\tau}_b - H_2\nabla P_a.$$

Here $\vec{\tau}$ is the stress vector where subscripts s, i, and b stand for surface, interface, and bottom, respectively. The atmospheric pressure at the sea surface is P_a.

The normal mode form of the equations can be derived from these primitive equations by a method similar to that employed by Veronis and Stommel (1956). To transform (1) and (2) into normal mode form, we multiply (1) and (2) by α and (3) and (4) by β and add the corresponding momentum and mass conservation equations, respectively, to obtain

$$\partial\vec{M}/\partial t + f\vec{k}x\vec{M} + g\{\nabla[\alpha H_1(\rho_1 h_1 + \rho_1 h_2) + \beta H_2(\rho_1 h_1 + \rho_2 h_2)]$$
$$-[(\rho_1 h_1 + \rho_1 h_2)\nabla(\alpha H_1) + (\rho_1 h_1 + \rho_2 h_2)\nabla(\beta H_2)]\} = \vec{G}, \qquad (6)$$

$$\partial\phi/\partial t + \alpha\nabla\cdot\vec{M}_1 + \beta\nabla\cdot\vec{M}_2 = 0, \qquad (7)$$

where

$$\vec{M} \equiv \alpha\vec{M}_1 + \beta\vec{M}_2,$$

$$\phi \equiv \alpha\rho_1 h_1 + \beta\rho_2 h_2, \qquad (8)$$

$$\vec{G} \equiv \alpha\vec{F}_1 + \beta\vec{F}_2.$$

Note that α and β are non-dimensional and, for the case of variable depth, may depend upon x and y (this is the generalization of the Veronis and Stommel analysis).

The constraint imposed on α and β to make the elevation anomalies in (6) and (7) proportional, is

$$\alpha H_1(\rho_1 h_1 + \rho_1 h_2) + \beta H_2(\rho_1 h_1 + \rho_2 h_2) = \Gamma\phi, \qquad (9)$$

where Γ, a factor of proportionality, is an equivalent depth to be determined. Since $\phi = \alpha\rho_1 h_1 + \beta\rho_2 h_2$, then (9) will be valid for all combinations of h_1 and h_2 if

$$\alpha H_1 + \beta H_2 = \Gamma\alpha, \text{ and} \tag{10a}$$

$$\alpha H_1(\rho_1/\rho_2) + \beta H_2 = \Gamma\beta. \tag{10b}$$

It can be readily shown that (6) and (7) can be written in the form

$$\partial\vec{M}/\partial t + f\vec{k}x\vec{M} + g\Gamma\nabla\phi - \vec{B} = \vec{G}, \tag{11}$$

$$\partial\phi/\partial t + \nabla\cdot\vec{M} - C = 0, \tag{12}$$

where

$$\vec{B} \equiv g\Gamma(\rho_1 h_1 \nabla\alpha + \rho_2 h_2 \nabla\beta), \text{ and} \tag{13}$$

$$C \equiv \vec{M}_1 \cdot \nabla\alpha + \vec{M}_2 \cdot \nabla\beta.$$

For the case of constant layer depth H_1, H_2, the α and β are constant and $\vec{B}$, C vanish. In general these terms produce coupling of the modes in the presence of bottom topography.

Eqs. (10a,b) can be written in matrix form as

$$\begin{bmatrix} H_1 - \Gamma & H_2 \\ \\ (\rho_1/\rho_2)H_1 & H_2 - \Gamma \end{bmatrix} \begin{bmatrix} \alpha \\ \\ \beta \end{bmatrix} = \begin{bmatrix} 0 \\ \\ 0 \end{bmatrix} \tag{14}$$

and hence the eigenvalues of Γ are the roots of the characteristic equation

$$\Gamma^2 - D\Gamma + \epsilon H_1 H_2 = 0 , \tag{15}$$

where D is the total depth at rest (H_1+H_2), and ϵ is the relative density difference, $(\rho_2-\rho_1)/\rho_2$.

The two roots of (15), which correspond to the equivalent depths for external and internal modes, are

$$\Gamma_e = D[1-\epsilon(H_1 H_2/D^2) + O(\epsilon^2)] , \text{ and}$$

$$\tag{16}$$

$$\Gamma_i = \epsilon(H_1 H_2/D)[1+\epsilon(H_1 H_2/D^2) + O(\epsilon^2)].$$

Since $H_1 H_2/D^2 < 1$ and $\epsilon \ll 1$ for the general ocean basin, then

$$\Gamma_e \simeq D , \text{ and}$$

$$\tag{17}$$

$$\Gamma_i \simeq \epsilon(H_1 H_2/D)$$

are the equivalent depths for external and internal modes as obtained by Veronis and Stommel (1956). In general these may depend on x,y.

The ratio of a and β can be determined from (10a,b) as

$$\beta/a = \Gamma - H_1/H_2 = (\rho_1/\rho_2)H_1/\Gamma - H_2. \tag{18}$$

Substituting (17) in (18), the ratio (a/β) for each mode is

$$(\beta/a)_e = 1 - \epsilon(H_1/D) - \epsilon^2(H_1^2 H_2/D^3) , \text{ and}$$

$$\tag{19}$$

$$(\beta/a)_i = -H_1/H_2 + \epsilon(H_1/D) + \epsilon^2(H_1^2 H_2/D^3).$$

Note that a_e and β_e are of like sign, but a_i and β_i are of opposite sign. a_e, β_e, a_i are chosen to be positive and β_i to be negative.

Veronis and Stommel (1956) took $a_e = a_i = 1$ for a constant depth basin. However, the presence of coupling terms $\vec{B}$ and C in (11) and (12) due to varying depth in the present study precludes an arbitrary choice of a. Notice that both a and β are functions of x and y.

The procedure used to determine the individual values of a and β for both modes is based on energy considerations. In essence the energy equations derived from the primitive equations and the normal mode equations must be consistent.

The two energy equations formed from the primitive equations and the normal mode equations, respectively, are

$$\partial(E_k+E_p)/\partial t + \nabla\cdot\vec{J} = S, \qquad (20)$$

where

$$E_k = \tfrac{1}{2}g(\rho_1 h_1^2 + 2\rho_1 h_1 h_2 + \rho_2 h_2^2),$$

$$E_p = \tfrac{1}{2}[(M_1^2/\rho_1 H_1) + (M_2^2/\rho_2 H_2),$$

$$\qquad (21)$$

$$\vec{J} = g[(h_1+h_2)\vec{M}_1 + 1/\rho_2(\rho_1 h_1+\rho_2 h_2)\vec{M}_2],$$

$$S = \vec{M}_1\cdot\vec{F}_1/\rho_1 H_1 + \vec{M}_2\cdot\vec{F}_2/\rho_2 H_2.$$

and

$$\partial(E_k+E_p)/\partial t + \nabla\cdot\vec{J} - T = S. \qquad (22)$$

Equation (22) contains not only the additional term T, but the expressions for the kinetic energy per unit area, E_k, the potential energy per unit area, E_p, the energy flux per unit width, $\vec{J}$, and the net energy supply per unit width per unit time, S, are also different from those given in (21). The added term, T, which defines the

energy transfer between modes, and the other terms in (22) are defined as follows:

$$T = 1/\rho_2[(\vec{M}_e \cdot \vec{B}_e/\Gamma_e) + \epsilon(\vec{M}_i \cdot \vec{B}_i/\Gamma_i) + g(\phi_e C_e + \epsilon \phi C_i)]. \quad (23)$$

$$E_k = 1/\rho_2[(M_e^2/\Gamma_e) + \epsilon(M_i^2/\Gamma_i)], \quad (24a)$$

$$E_p = 1/\rho_2 g(\phi_e^2 + \epsilon \phi_i^2), \quad (24b)$$

$$\vec{J} = g/\rho_2(\phi_e \vec{M}_e + \epsilon \phi_i \vec{M}_i), \quad (24c)$$

$$S = 1/\rho_2[(\vec{M}_e \cdot G_e/\Gamma_e) + \epsilon(\vec{M}_i \cdot G_i/\Gamma_i)], \quad (24d)$$

where G_e and G_i are defined in (31).

If (20) and (22) are to be consistent, their corresponding terms must be equal and T must be zero. Inserting (8a) to (8c) in (24a) to (24d) it can be shown that the necessary conditions that E_k as well as S in (20) and (22) are consistent for arbitrary h_1, h_2, $\vec{M}_1$, and $\vec{M}_2$ are that

$$a_e^2/\Gamma_e + \epsilon a_i^2/\Gamma_i = 1/H_1(\rho_2/\rho_1), \quad (25a)$$

$$\beta_e^2/\Gamma_e + \epsilon \beta_i^2/\Gamma_i = 1/H_2, \quad (25b)$$

$$a_e \beta_e/\Gamma_e + \epsilon a_i \beta_i/\Gamma_i = 0. \quad (25c)$$

It is also necessary, for consistency in E_p and $\vec{J}$, that

$$a_e^2 + \epsilon a_i^2 = \rho_1/\rho_2, \quad (26a)$$

$$\beta_e^2 + \epsilon \beta_i^2 = 1, \quad (26b)$$

$$a_e \beta_e + \epsilon a_i \beta_i = 1. \quad (26c)$$

12

The requirement that T must be zero can be examined by substituting (13) in (23) and rearranging to yield,

$$T = \rho_1 h_1 \vec{M}_1 \cdot \nabla(a_e^2 + \epsilon a_i^2) + (\rho_1 h_1 \vec{M}_2 + \rho_2 h_2 \vec{M}_1) \cdot \nabla(a_e \beta_e + \epsilon a_i \beta_i) + \rho_2 h_2 \vec{M}_2 \cdot \nabla(\beta_e^2 + \epsilon \beta_i^2).$$ (27)

Using conditions (26a) to (26c), it can be shown that T vanishes provided that the ratio ρ_2/ρ_1 is constant. Therefore, (25) and (26) assure that (20) and (22) are entirely consistent with T equal to zero and all other terms are identical. These two sets of equations will also be used to determine a and β.

From (25a),(25b) and (26a),(26b) we find

$$a_e^2 = \rho_2 \Gamma_e / \rho_1 H_1 [(H_1 - \Gamma_i)/(\Gamma_e - \Gamma_i)],$$ (28)

$$\beta_e^2 = \Gamma_e / H_2 [(H_2 - \Gamma_i)/(\Gamma_e - \Gamma_i)],$$

and

$$a_i^2 = \rho_2 \Gamma_i / \epsilon \rho_1 H_1 [(\Gamma_e - H_1)/(\Gamma_e - \Gamma_i)],$$ (29)

$$\beta_i^2 = \Gamma_i / \epsilon H_2 [(\Gamma_e - H_2)/(\Gamma_e - \Gamma_i)].$$

It is not difficult to show that the ratios $(\beta/a)_e$ and $(\beta/a)_i$ obtained from (28) and (29) are the same as those in (19). If we substitute (16) in (28) and (29), we obtain the relation for a and β, accurate to order ϵ, in terms of H_1, H_2 and D as follows:

$$a_e = 1 + \tfrac{1}{2}\epsilon - \tfrac{1}{2}\epsilon(H_2/D)^2 + O(\epsilon^2),$$ (30a)

$$\beta_e = 1 - \tfrac{1}{2}\epsilon(H_1/D)^2 + O(\epsilon^2),$$ (30b)

13

$$a_i = H_2/D\{1+\tfrac{1}{2}\epsilon + \epsilon[(H_1H_2/D^2)-\tfrac{1}{2}(H_1/D)] + O(\epsilon^2)\} \quad (30c)$$

$$\beta_i = -H_1/D\{1+\epsilon[(H_1H_2/D^2)-\tfrac{1}{2}(H_2/D)] + O(\epsilon^2)\} \quad (30d)$$

Note that positive roots are chosen except for β_i. Using a and β from (30) it can be verified that (25c) and (26c) are correct to the order ϵ.

b) Normal Mode Equations

To express Eqs.(11) and (12) with all dependent variables in terms of modes, (8) is rewritten for each mode as:

$$\vec{M}_e = a_e\vec{M}_1 + \beta_e\vec{M}_2$$

$$\vec{M}_i = a_i\vec{M}_1 + \beta_i\vec{M}_2$$

$$\phi_e = a_e\rho_1h_1 + \beta_e\rho_2h_2$$

$$\phi_i = a_i\rho_1h_1 + \beta_i\rho_2h_2 \quad (31)$$

$$G_e = a_e\vec{F}_1 + \beta_e\vec{F}_2$$

$$G_i = a_i\vec{F}_1 + \beta_i\vec{F}_2.$$

It readily can be shown from (31) that

$$\rho_1h_1 = r(\beta_e\phi_i - \beta_i\phi_e)$$

$$\rho_2h_2 = r(-a_e\phi_i + a_i\phi_e)$$

$$\vec{M}_1 = r(\beta_e\vec{M}_i - \beta_i\vec{M}_e) \quad (32)$$

14

$$\vec{M}_2 = r(-a_e \vec{M}_i + a_i \vec{M}_e),$$

where $r = (a_i \beta_e - a_e \beta_i)^{-1}$. Using (30a) to (30d), the factor r is $(\rho_1/\rho_2)^{1/2}$ to order ϵ and

$$h_1 = [\phi + (H_1/D)\phi_e](\rho_1 \rho_2)^{-\frac{1}{2}},$$

$$h_2 = [(\epsilon H_2/D - 1)\phi + (H_2/D)\phi_e](\rho_1 \rho_2)^{-\frac{1}{2}},$$

(33)

$$\vec{M}_1 = (H_1/D)\vec{M}_e + \vec{M}_i,$$

$$\vec{M}_2 = (H_2/D)\vec{M}_e - \vec{M}_i.$$

Using (31) and (32) the coupling terms defined by (13) can be approximated by,

$$\vec{B}_e \simeq rg\Gamma_e \epsilon \phi_i \nabla(H_1/D),$$

$$\vec{B}_i \simeq -g\Gamma_i \phi_e \nabla(H_1/D),$$

(34)

$$C_e \simeq r\epsilon \vec{M}_i \cdot \nabla(H_1/D),$$

$$C_i \simeq -\vec{M}_e \cdot \nabla(H_1/D).$$

These forms show clearly that the external mode is influenced by the internal mode and vice versa when H_1/D is variable.

It can be shown by substituting (34) in (23) that the energy transfer between modes, T, is zero as required.

Finally, the forcing terms $\vec{G}$ can be approximated by using (5), (8), and (31) as:

$$G_e = \vec{\tau}_s - \vec{\tau}_b - D\nabla P_a + O(\epsilon),$$

$$(35)$$

$$G_i = (H_2/D)\vec{\tau}_s + (H_1/D)\vec{\tau}_b - \vec{\tau}_i + O(\epsilon).$$

The kinematic counterparts of $\vec{M}$, ϕ, $\vec{\tau}$ and P_a are defined as

$$\vec{Q}_e \equiv \vec{M}_e/\rho, \qquad \vec{Q}_i \equiv \vec{M}_i/\rho,$$

$$\psi_e \equiv \phi_e/\rho, \qquad \psi_i \equiv \phi_i/\rho,$$

$$(36)$$

$$\vec{T}_s \equiv \vec{\tau}_s/\rho, \qquad \vec{T}_i \equiv \vec{\tau}_i/\rho,$$

$$\vec{T}_b \equiv \vec{\tau}_i/\rho, \qquad -\nabla P_a/\rho \equiv g\nabla b,$$

The variable b in (36) is the barometric pressure deficit expressed in terms of an equivalent head of water (sometimes referred to as the inverted barometric effect).

The normal mode equations (11) and (12), therefore, take the form

$$\partial\vec{Q}_e/\partial t + f\vec{k}x\vec{Q}_e + gD\nabla\psi_e - \epsilon gD\psi_i\nabla(H_1/D) = (\vec{T}_s - \vec{T}_b + gD\nabla b),$$

$$(37)$$

$$\partial\psi_e/\partial t + \nabla\cdot\vec{Q}_e - \epsilon\vec{Q}_i\cdot\nabla(H_1/D) = 0 ,$$

and

$$\partial\vec{Q}_i/\partial t + f\vec{k}x\vec{Q}_i + g\Gamma_i\nabla\psi_i + g\Gamma_i\psi_e\nabla(H_1/D) = (H_2/D)\vec{T}_s + (H_1/D)\vec{T}_b - \vec{T}_i,$$

$$(38)$$

$$\partial\psi_i/\partial t + \nabla\cdot\vec{Q}_i + \vec{Q}_e\cdot\nabla(H_1/D) = 0 ,$$

where Γ_i is given in (17).

16

2. Numerical model

a) Grid system

A space-staggered computational mesh is employed in the numerical analogs of the normal mode equations (37) and (38). The grid spacing is taken as 15' x 15' in latitude ($\Delta\Phi$) and longitude ($\Delta\lambda$). The modal transport per unit width, represented by U, V for east and north components, respectively, is located at the mid points of the appropriate sides of each grid block. The modal water level anomaly, ψ, is defined at the middle of each grid block. Figure 1 illustrates locations of these variables whose positions are identified by I,J and time is indexed by n. The grid spacing is taken as the distance between the same variables, thus consecutive U, ψ values are at half increments of I and consecutive V, ψ values are at half increments of J. The depth is stored at every variable location.

The grid system used in this study is the same as that used in the Gulf of Mexico Tidal Model (Reid and Whitaker, 1981). It nominally covers 70 x 50 grid blocks for the Gulf of Mexico and the northwest portion of the Caribbean Sea (Cayman Sea) as shown in Fig. 2.

The depths of the Gulf of Mexico were digitized from bathymetry charts prepared by Buffler et al. (1984). The Cayman Sea depths were taken from available hydrographic charts. Depth over most of the Cayman, especially near the open boundaries to the east and south, was taken as 4000 m. Figure 3 shows the computer plotted contours of

17
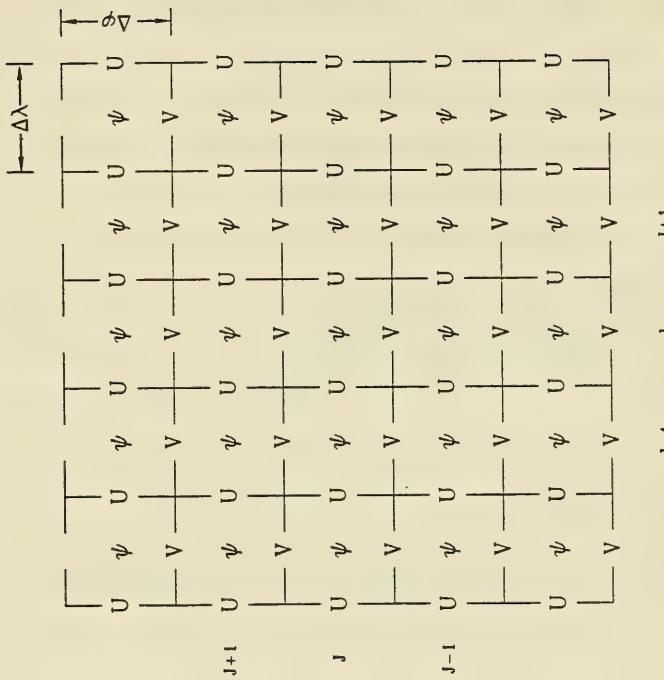
Fig. 1. Computing lattice showing locations where U, V, ψ are evaluated. Positive U is toward the east (increasing index I). Positive V is to the north (increasing index J).
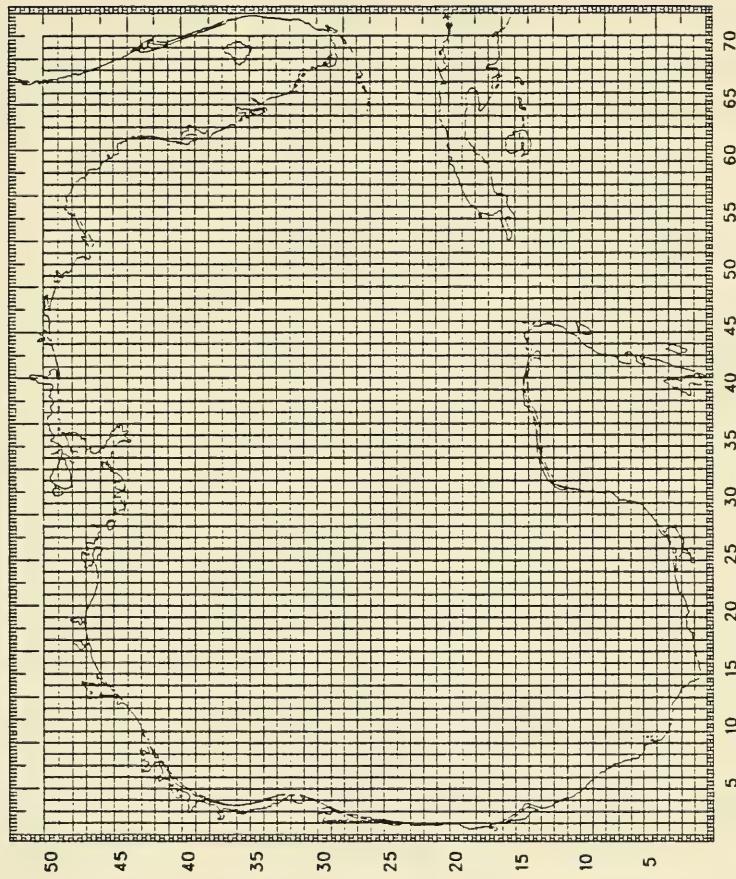
Fig. 2. Grid system for the Gulf of Mexico and the Cayman Sea. The grid increments are 15 in latitude and longitude.

19
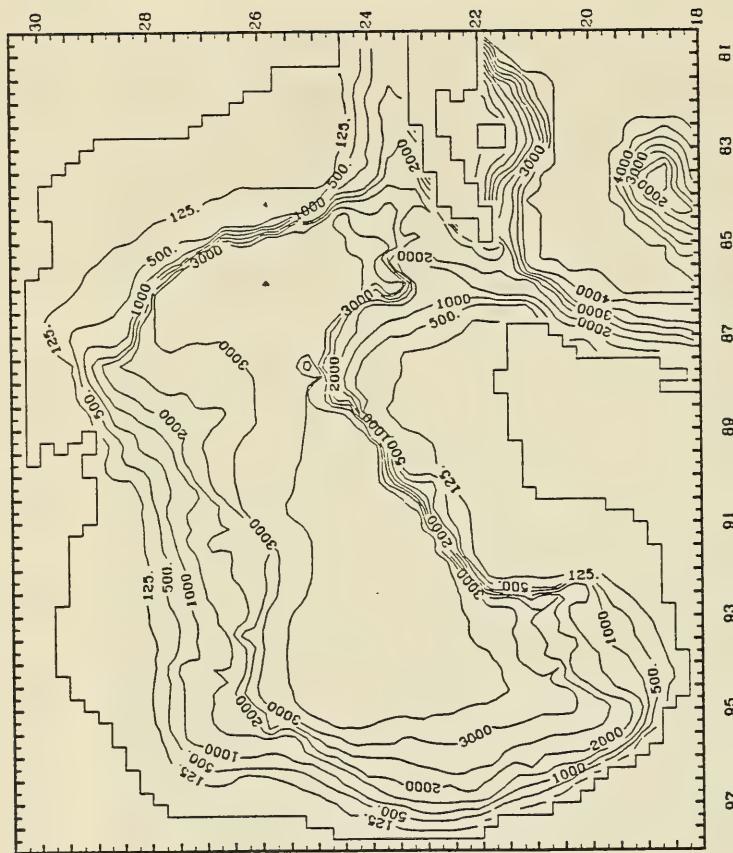
Fig. 3. Model coastline and sample contours of the digitized bathymetry. Depths in meters.

20

the digitized depth field. Special care was observed when comparing
the digitized depth fields to the bathymetry chart, especially in the
shelf break regions and modifications were made where necessary.

b) Numerical integration scheme

The multioperational alternating direction implicit algorithm
developed by Leendertse (1967) was adopted for time integration of
the finite difference equations. The following notation is used in
the discussion. The spatial average of a field variable X is
written as

$$\bar{\bar{X}}^n(I,J) = \tfrac{1}{4}[X(I-\tfrac{1}{2},J-\tfrac{1}{2})+X(I+\tfrac{1}{2},J-\tfrac{1}{2})+X(I-\tfrac{1}{2},J+\tfrac{1}{2})+X(J+\tfrac{1}{2},J+\tfrac{1}{2})], \quad (39)$$

where $X^n(I,J) \equiv X(\lambda_0+I\Delta\lambda,\Phi_0+J\Delta\Phi,t_0+n\Delta t)$. Time and space derivatives
are depicted by the standard centered differences,

$$\partial X/\partial t = (1/\Delta t)[X^{n+1}(I,J)-X^{n-1}(I,J)],$$

$$(40)$$

$$\partial X/\partial\lambda = (\cos\Phi/\Delta\lambda)[X^n(I+\tfrac{1}{2},J)-X^n(I-\tfrac{1}{2},J)].$$

A spherical coordinate system is employed in representing the
gradient terms on a level surface, i.e.,

$$\nabla X = (1/a\theta(J))\{\partial X/\partial\Phi \; \vec{a} + \theta(J)\partial X/\partial\lambda \; \vec{b}\} \quad (41)$$

where X is any scalar field variable, $\vec{a}$ is a unit vector along lines
of constant Φ, $\vec{b}$ is a unit vector along lines of constant λ, and
$\theta(J) = \cos(\Phi_0+J\Delta\Phi)$, where Φ_0 is the reference latitude ($18°N$).

21

The cycle of calculation is separated into two operations. During the first-half cycle, at odd time steps, ψ and U are computed implicitly along lines of constant latitude, followed by an explicit computation of the V field. For the second half-cycle, the computations proceed along lines of constant longitude with ψ, V updated implicitly and U computed explicitly. In each half-cycle, the external mode computations are executed first and, after completing the entire computing domain, are repeated for the internal mode.

The implicit formulation of the finite difference analogs of the external mode momentum and mass conservation equations, respectively, are, for odd time steps,

$$-\gamma_x(I-\tfrac{1}{2},J)\psi_e^{n+1}(I-\tfrac{1}{2},J) + U_e^{n+1}(I,J) + \gamma_x(I+\tfrac{1}{2},J)\psi_e^{n+1}(I+\tfrac{1}{2},J)$$

$$= U_e^n(I,J) + 2\Delta t f(J)\bar{\bar{V}}_e^n(I,J) + \Delta t F_e + \chi_i, \text{ and} \qquad (42)$$

$$-v_x(J)U_e^{n+1}(I-\tfrac{1}{2},J) + \psi_e^{n+1}(I,J) + v_x(J)U_e^{n+1}(I+\tfrac{1}{2},J)$$

$$= \psi_e^n(I,J) - v_y\delta_y V_e^n(I,J) + \xi_i, \qquad (43)$$

and for even time steps

$$-\gamma_y(I,J-\tfrac{1}{2})\psi_e^{n+1}(I,J-\tfrac{1}{2})\theta(J-\tfrac{1}{2}) + V_e^{n+1}(I,J) + \gamma_y(I,J+\tfrac{1}{2})\psi_e^{n+1}(I,J+\tfrac{1}{2})\theta(J+\tfrac{1}{2})$$

$$= V_e^n(I,J) - \Delta t f(J)\bar{\bar{U}}_e^n(I,J) + \chi_i + \Delta t F_e, \qquad (44)$$

$$-v_y(J-\tfrac{1}{2})V_e^{n+1}(I,J-\tfrac{1}{2}) + \psi_e^{n+1}(I,J) + v_y(J+\tfrac{1}{2})V_e^{n+1}(I,j+\tfrac{1}{2})$$

$$= \psi_e^n - v_x\delta_x U_e^n(I,J) + \xi_i, \qquad (45)$$

where

$$\gamma_x(I,J) \;=\; (\Delta t/\Delta\lambda)\{gD(I,J)/a\theta(J)\},$$

$$\gamma_y(I,J) \;=\; (\Delta t/\Delta\Phi)\{gD(I,J)/a\theta(J)\},$$

$$v_x(J) \;=\; (\Delta t/\Delta\lambda)\{1/a\theta(J)\},$$

$$v_y(J) \;=\; (\Delta t/\Delta\Phi)\{1/a\theta(J)\},\cdot$$

$$\delta_x U_e^n(I,J) \;=\; U_e^n(I+\tfrac{1}{2},J) - U_e^n(I-\tfrac{1}{2},J),$$

$$\delta_y V_e^n(I,J) \;=\; V_e^n(I,J+\tfrac{1}{2})\theta(J+\tfrac{1}{2}) - V_e^n(I,J-\tfrac{1}{2})\theta(J-\tfrac{1}{2}),$$

$$a = \text{radius of the Earth,}$$

$$f(J) = 2\Omega\sin(\Phi_o+J\Delta\Phi),$$

$$F = \text{forcing and friction terms,}$$

$$\chi,\xi = \text{coupling terms.}$$

The forcing and coupling terms will be discussed in the next section. The coupling terms in (42) and (43) or (44) and (45) are of opposite mode relative to the other terms.

Upon replacing the total depth, D, by the equivalent depth, $\epsilon H_1 H_2/D$, interchanging modes of all field variables and coupling terms, and using the proper forcing terms, (42) through (45) are also representations of the implicit formulation for the internal mode computation.

The explicit coding of the external mode momentum equation at odd time steps is

23

$$V_e^{n+1}(I,J) = V_e^n(I,J) - \tfrac{1}{2}\Delta t\ f(J)\{\overline{\overline{U}}_e^{n+1}(I,J) + \overline{U}_e^n(I,J)\}$$

$$-\gamma_y(I,J)\delta_y\psi_e^n(I,J) + \chi_i + \Delta t F_e. \tag{46}$$

The even time step counterpart of (46) is

$$U_e^{n+1}(I,J) = U_e^n(I,J) - \tfrac{1}{2}\Delta t\ f(J)\{\overline{\overline{V}}_e^{n+1}(I,J) + \overline{V}_e^n(I,J)\}$$

$$-\gamma_x(I,J)\delta_x\psi_e^n(I,J) + \chi_i + \Delta t\ F_e. \tag{47}$$

Likewise, the explicit coding, at odd and even time steps, respectively, for the internal mode computation is obtained by replacing the total depth by the equivalent depth, interchanging modes of all field variables and coupling terms, and employing the proper forcing terms in (46) and (47).

Eqs. (42) and (43) or (44) and (45) form a system of linear algebraic equations in the collective I or J, depending upon time step, of ψ and either U or V at time level n+1. The coefficient matrix is tridiagonal for which there exists a double sweep solution algorithm for inversion, provided that boundary conditions on U or V or some combination of conditions on U or V and ψ are supplied at each end of the array of variables.

c) Surface, interface, and bottom stress

The forcing term F in (42) and (44) consists of the surface stress, the bottom stress and either the atmospheric pressure force due to a surface pressure deficit for the external mode forcing or the interface stress for the internal mode forcing, respectively. That is

$$F_e = \vec{T}_s - \vec{T}_b + gD\nabla b, \text{ or}$$

$$F_i = (\frac{H_2}{D})\vec{T}_s + (\frac{H_1}{D})\vec{T}_b - \vec{T}_i. \tag{48}$$

The stress terms are presented in the form

$$\vec{T} = \kappa|\vec{W}|\vec{W}. \tag{49}$$

For the surface stress, $\vec{W}$ is the wind speed at an elevation of 10 m above the water surface. Reid and Bodine (1968) considered κ as a function of wind speed in the form

$$\kappa = \kappa_1 \qquad\qquad \text{for } |\vec{W}| \leq W_c$$

$$\kappa = \kappa_1 + \kappa_2(1-W_c/|\vec{W}|)^2 \quad \text{for } |\vec{W}| \geq W_c \tag{50}$$

where κ_1 and κ_2 are taken as 1.1×10^{-6} and 2.5×10^{-6}, respectively, and W_c is a critical wind speed which is taken as 7.0 m/s. The coefficient κ is related to the drag coefficient, C_D by the relation

$$\kappa = (\rho_a/\rho_w)C_D \tag{51}$$

where ρ_a is air density and ρ_w is water density.

For large wind speed, κ approaches the limiting value of 3.6×10^{-6} which corresponds to a drag coefficient of about 3.0×10^{-3} if the density ratio between air and water is assumed to be 1.2×10^{-3}. Equation (50) was used by Wanstrath (1975) in his simulation of storm surge in transformed coordinates while Miyasaki (1963) used a constant 3.2×10^{-6} for κ in his computation of storm surge for hurricane Carla. The choice of κ for intense winds ($|\vec{W}| \geq 50$ m/s) is

controversial. However, taking into account that wind speeds associated with hurricanes are not steady or uniform, κ is taken as a function of wind speed.

The surface wind stresses are computed at every time step using linear interpolated positions of the hurricane center which are given at 6 h intervals, except for the case of hurricane Carla simulation which will be discussed later. A constant inflow angle of 20° is used to rotate the surface stress vector before the components are computed.

For the bottom stress, $\vec{W}$ is the depth averaged lower layer current velocity, i.e.

$$\vec{T}_b = \kappa |\vec{V}_2| \vec{V}_2, \tag{52}$$

where $|\vec{V}_2|$ is the magnitude of the depth averaged lower layer current. A constant value of 2.5×10^{-3} is assumed for the coefficient κ. The lower layer current, $|\vec{V}_2|$ is given in terms of the modal velocities by the relation

$$\vec{V}_2 = (1/D)\vec{V}_e - (1/H_2)\vec{V}_i, \tag{53}$$

where $\vec{V}_e$ and $\vec{V}_i$ are the external and internal velocity vectors, respectively.

The bottom stress for the external mode computation at odd time steps is coded as

$$T_b = 2.5 \times 10^{-3} \Delta t \{ [(1/D)U_e^{n-1}(I,J) - (1/H_2)U_i^{n-1}(I,J)]^2 + [(1/D)\overline{V}_e^{n-1}(I,J) - (1/H_2)\overline{V}_i^{n-1}(I,J)]^2 \}^{\frac{1}{2}} \{ -(1/H_2)U_i^{n-1}(I,j) \}. \tag{54}$$

Upon substituting (53) in (52) both U_e and U_i from the previous time

step are used in $|\vec{V}_2|$ while only the previous value of U_i is used in $\vec{V}_2$. This implies that the coefficient of U_e on the left hand side of (42) has to be changed from a constant value of 1 to $1 - 2.5 \times 10^{-3}(\Delta t/D)$. However, the tridiagonal form of the coefficient matrix is retained.

At even time steps, coding for the bottom stress is obtained by directly interchanging U and V to obtain

$$T_b = 2.5 \times 10^{-3} \Delta t \{ [(1/D)V_e^{n-1}(\bar{I},J) - (1/H_2)V_i^{n-1}(\bar{I},J)]^2$$
$$+ [(1/D)\bar{U}_e^{n-1}(\bar{I},J) - (1/H_2)\bar{U}_i^{n-1}(\bar{I},J)]^2 \}^{\frac{1}{2}} \{ -(1/H_2)V_i^{n-1}(\bar{I},J) \}. \quad (55)$$

The bottom stress for the internal mode computation is depicted as

$$T_b = 2.5 \times 10^{-3} \Delta t \{ [(1/D)U_e^{n-1}(\bar{I},J) - (1/H_2)U_i^{n-1}(\bar{I},J)]^2$$
$$+ [(1/D)\bar{V}_e^{n-1}(\bar{I},J) - (1/H_2)\bar{V}_i^{n-1}(\bar{I},J)]^2 \}^{\frac{1}{2}} \{ (1/D)U_e^{n-1}(\bar{I},J) \} \quad (56)$$

$$T_b = 2.5 \times 10^{-3} \Delta t \{ [(1/D)V_e^{n-1}(\bar{I},J) - (1/H_2)V_i^{n-1}(\bar{I},J)]^2$$
$$+ [(1/D)\bar{U}_e^{n-1}(\bar{I},J) - (1/H_2)\bar{U}_i^{n-1}(\bar{I},J)]^2 \}^{\frac{1}{2}} \{ (1/D)V_e^{n-1}(\bar{I},j) \} \quad (57)$$

for odd and even time steps, respectively.

The velocity vector $\vec{W}$ in the interface stress is the internal mode volume transport per unit width multiplied by the appropriate depth

$$\vec{W} = (D/H_1 H_2)\vec{Q}_i \quad (58)$$

A constant value of 2.0×10^{-5} is assumed for the friction coefficient, κ. The finite difference form of this stress is, for odd time steps,

$$T_i = 2.0 \times 10^{-5}\{[U_i^{n-1}(I,J)]^2 + [\bar{V}_i^{n-1}(I,J)]^2\}^{\frac{1}{2}}\{U_i^{n-1}(I,J) + \bar{V}_i^{n-1}(I,J)\},$$

and   (59)

$$T_i = 2.0 \times 10^{-5}\{[V_i^n(I,J)]^2 + [\bar{U}_i^n(I,J)]^2\}^{\frac{1}{2}}\{V_i^n(I,J) + \bar{U}_i^n(I,J)\},$$

for even time steps.

d) The coupling terms

     The coupling terms are coded based on the premise that the
energy transferred between modes due to coupling must be balanced.
The energy equations are formed by multiplying (37a,b) and (38a,b) by
$\vec{Q}_e/D$, $g\psi_e$, $\vec{Q}_i/\Gamma_i$, and $\epsilon g\psi_i$, respectively, and thus the coupling terms
appear as

$$-\epsilon g\psi_i\vec{Q}_e\nabla(H_1/D) \tag{60a}$$

$$-\epsilon g\psi_e\vec{Q}_i\nabla(H_1/D) \tag{60b}$$

$$\epsilon g\psi_i\vec{Q}_i\nabla(H_1/D) \tag{60c}$$

$$\epsilon g\psi_e\vec{Q}_e\nabla(H_1/D) \tag{60d}$$

     For simplicity, consider a one dimensional channel in cartesian
coordinates as sketched in figure 4. The solid boundary is at point
1 while there are three possible conditions at point 7; i) a solid
boundary, ii) an open port, and iii) an interior point where the
interface intersects the bottom. Since the depth, and hence the
ratio H_1/D, are defined at every field variable location the
gradients $[\frac{\partial}{\partial x}(H_1/D)]$ are defined at midpoints between U and ψ
locations (refer to points A, B, C, ... in Fig. 4). As an example,
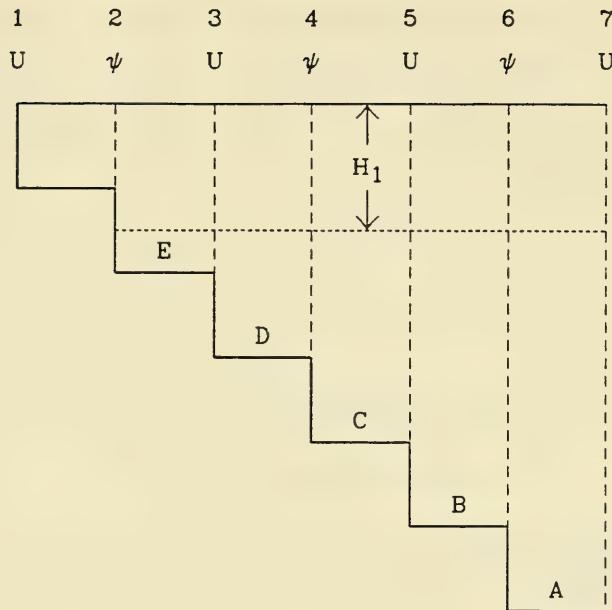
Fig. 4. Schematic of one dimensional channel with stair-step depth profile. Capital letters A through E indicate locations where the gradients $[\frac{\partial}{\partial x}(H_1/D)]$ are defined.

$$[\tfrac{\partial}{\partial x}(H_1/D)]_A = (H_1/D)_7 - (H_1/D)_6, \qquad (61)$$

where numeral subscripts indicate the points where the ratios are computed.

For the external mode computations, the continuity and momentum equations are alternately applied at points 2 through 6, while the internal mode computations start at point 4 in the same sequence. The summation of the coupling terms for one complete operation, after eliminating like terms, is

$$-\epsilon g[U_e]_3 \; \tfrac{1}{2}\{[\psi_i]_2[\tfrac{\partial}{\partial x}(H_1/D)]_E\}$$

$$+\epsilon g[\psi_i]_6 \; \tfrac{1}{2}\{[U_e]_7[\tfrac{\partial}{\partial x}(H_1/D)]_A\}$$

$$\qquad\qquad\qquad\qquad\qquad\qquad\qquad (62)$$

$$-\epsilon g[\psi_e]_2 \; \tfrac{1}{2}\{[U_i]_3[\tfrac{\partial}{\partial x}(H_1/D)]_E + [U_i]_1[\tfrac{\partial}{\partial x}(H_1/D)]_F\}$$

$$-\epsilon g[\psi_e]_6 \; \tfrac{1}{2}\{[U_i]_7[\tfrac{\partial}{\partial x}(H_1/D)]_A\}.$$

The internal mode computations start at point 4 as discussed earlier. Hence the first and third terms in (62) vanish. The residual terms depend upon the condition at point 7. If point 7 is a solid boundary, then $[U_e]_7 = [U_i]_7 = 0$ and the net energy transferred between modes is zero. The second possibility that point 7 is an open boundary requires that either the depths at point 6 and 7 are set equal or the gradient, $[\tfrac{\partial}{\partial x}(H_1/D)]_A$ is set to zero. In fact the two choices imply one another. It is more rational to set the gradient H_1/D to zero since all these gradients are computed only for the purpose of evaluating the coupling terms. If the interface intersects the bottom at point 7, then the external mode computations

30

are continued until a solid boundary or an open port is encountered, while the internal mode computations stop at point 6. It immediately follows that the last term in (62) vanishes. The coupling term obtained by applying the external momentum equation at point 7 is

$$-\epsilon g[U_e]_7 \frac{1}{2}\{[\psi_i]_6[\frac{\partial}{\partial x}(H_1/D)]_A\};$$
(63)

which exactly balances the only remaining term in (62). Note that the second part of the coupling term in (63) is omitted since it involves ψ_i, which is zero. It can be shown from (59a,b) that all the coupling terms are zero beyond point 7. As a result, the net transfer of energy between modes is zero.

In summary, with this form of coding, employing the average of the products $U[\frac{\partial}{\partial x}(H_1/D)]$ or $\psi[\frac{\partial}{\partial x}(H_1/D)]$, the only constraint needed to fulfill the energy requirement is that the gradient of (H_1/D) along the points just inside the open boundary be zero.

Therefore, the coupling terms, χ_i, and ξ_i, in the implicit computations of the external mode momentum and mass conservation equations, (41) and (43), are coded as follows:

$$\chi_i = \epsilon\gamma_x \frac{1}{2}\{\psi_i^n(I-\frac{1}{2},J)[(H_1/D(I,J))-(H_1/D(I-\frac{1}{2},J))]$$
$$+\psi_i^n(I,J+\frac{1}{2})[(H_1/D(I+\frac{1}{2},J))-(H_1/D(I,J))]\}.$$
(64a)

$$\xi_i = \frac{1}{2}\epsilon\{v_x\{U_i^n(I-\frac{1}{2},J)[(H_1/D(I,J))-(H_1/D(I-\frac{1}{2},J))]$$
$$+U_i^n(I+\frac{1}{2},J)[(H_1/D(I+\frac{1}{2},J))-(H_1/D(I,J))]\}$$
$$+v_y\{V_i^n(I,J+\frac{1}{2})\theta(J+\frac{1}{2})[(H_1/D(I,J+\frac{1}{2}))-(H_1/D(I,J))]$$
$$+V_i^n(I,J-\frac{1}{2})\theta(J-\frac{1}{2})[(H_1/D(I,J))-(H_1/D(I,J-\frac{1}{2}))]\}\}.$$
(64b)

For the explicit calculations at odd time steps, χ_i, in (46) becomes

31

$$X_i = \epsilon\gamma_y\tfrac{1}{2}\{\psi_i^n(I,J+\tfrac{1}{2})\theta(J+\tfrac{1}{2})[(H_1/D(I,J+\tfrac{1}{2}))-(H_1/D(I,J))]$$

$$+\psi_i^n(I-\tfrac{1}{2},J)\theta(J-\tfrac{1}{2})[(H_1/D(I,J))-(H_1/D(I,J-\tfrac{1}{2}))]\}. \qquad (65)$$

Note that the values of all the field variables at previous time steps are used in the expressions of the coupling terms. This implies that the codes for these terms at even time steps are the same as those at odd time steps except for the sequence in which they are applied. Eqs. (65), (64b), and (64a) are the codes employed for implicit computations of V and ψ and for explicit computations of U, respectively.

Sequential coding of coupling terms for the implicit and explicit internal mode computations at odd time steps, are

$$X_e = -g[\epsilon H_1 H_2/D(I,J)]v_x\tfrac{1}{2}\{\psi_e^n(I-\tfrac{1}{2},J)[(H_1/D(I,J))-(H_1/D(I-\tfrac{1}{2},J))]$$

$$+\psi_e^n(I,J+\tfrac{1}{2})[(H_1/D(I+\tfrac{1}{2},J))-(H_1/D(I,J))]\}, \qquad (66a)$$

$$\xi_e = -\tfrac{1}{2}\{U_x\{U_e^n(I-\tfrac{1}{2},J)[(H_1/D(I,J))-(H_1/D(I-\tfrac{1}{2},J))]$$

$$+U_e^n(I+\tfrac{1}{2},J)[(H_1/D(I+\tfrac{1}{2},J))-(H_1/D(I,J))]\}$$

$$+v_y\{V_e^n(I,J+\tfrac{1}{2})\theta(J+\tfrac{1}{2})[(H_1/D(I,J+\tfrac{1}{2}))-(H_1/D(I,J))]$$

$$+V_e^n(I,J-\tfrac{1}{2})\theta(J-\tfrac{1}{2})[(H_1/D(I,J))-(H_1/D(I,J-\tfrac{1}{2}))]\}\}, \text{ and} \qquad (66b)$$

$$X_e = -g[\epsilon H_1 H_2/D(I,J)]v_y\tfrac{1}{2}\{\psi_e^n(I,J+\tfrac{1}{2})\theta(J+\tfrac{1}{2})[(H_1/D(I,J+\tfrac{1}{2})))$$

$$-(H_1/D(I,J))]+\psi_e^n(I-\tfrac{1}{2},J)\theta(J-\tfrac{1}{2})[(H_1/D(I,J))-(H_1/D(I,J-\tfrac{1}{2}))]\}. (67)$$

The same considerations for the coding at even time steps as discussed above also apply.

It is noteworthy that the numerical coding of the coupling terms employed is the only possible form, on the basis of energy transfer,

for the spatial-staggered grid system used in this study. Furthermore, the energy transfer is balanced globally, but not locally. In other words, a balance is obtained when considering the entire domain but not at any individual grid block.

e) Initial and boundary conditions

The model was taken initially at rest. The initial positions of the storms were in the Cayman Sea for the hurricanes of record and for all except one synthetic storm employed in the parametric study which will be discussed in Chapter IV.

Specified volume transport or height anomalies are employed as boundary conditions. Along the solid coastal boundaries the normal component of volume transport is specified as zero. At the open grid elements water levels are placed in equilibrium with the inverted barometric pressure for the external mode and zero for the internal mode.

3. Wind and pressure forcing

a) Analytical wind model

Practically, there are two methods of portraying hurricane wind fields on the computing grid. One method is to digitize the surface charts that are available. The data are sampled at stipulated time intervals and grid points and then interpolated in space and time to provide the necessary information to the model. This method requires detailed surface charts of wind throughout the simulation period. In addition, this is a laborious technique to apply, especially for this

study which requires these data over long time periods. The alternative, which is used in this study, is to derive the required forcing fields from a parametric analytical model.

Schwerdt et al. (1979) developed a model for surface wind fields associated with hurricanes for the Gulf and East Coasts of the United States which is commonly known as National Weather Service Model, NWS-23. This model was employed to reconstruct radial wind profiles for hurricane Carla. Comparisons between the model results and the observed profiles revealed that this model does not satisfactorily depict the observed Carla winds in the far field. It is remarked that effect of the storm forward speed is ignored

In NWS-23 there are two variables, the maximum wind, V_m, and the radius to maximum wind, R, that determine the wind speed for a stationary storm. Therefore, in order to obtain good comparison of the winds in the far field, either V_m or R, or both have to be changed and this inevitably deteriorates the winds near the center of the storm.

Holland (1980) proposed a new model that has two parameters, C and k that independently define the location of the maximum winds and the shape of the wind profile, respectively. The model thus allows the adjustment of wind speed in the far field through the parameter k, without changing R. The gradient wind profile is given as

$$W_g = [Ck(P_n - P_c)\exp(-C/r^k)/\rho_a r^k + (\tfrac{1}{2}rf)^2]^{\frac{1}{2}} - \tfrac{1}{2}rf, \qquad (68)$$

where W_g is the gradient wind at a distant r from the center, f is the Coriolis parameter, ρ_a is the the air density (assumed constant),

34

P_c is the central pressure, and P_n is the ambient pressure.

Holland determined C and k by fitting the pressure profile

$$P = P_c + (P_n - P_c)\exp(-C/r^k). \qquad (69)$$

However, he pointed out that this approach would underestimate the peak winds and that wind observations, if available, should be used directly.

For hurricane Carla, there were detailed surface charts available. Equation (68) was modified for the direct approach as follows: First, C was eliminated by considering that the cyclostrophic wind

$$W_c = [Ck(P_n - P_c)\exp(-C/r^k)/\rho_a r^k]^{\frac{1}{2}}, \qquad (70)$$

was a more appropriate representation of the maximum wind. Upon taking dW_c/dr and setting it equal to zero at r=R, we obtain the relation

$$R = C^{1/k} \text{ or } C = R^k . \qquad (71)$$

Since detailed surface charts allow a good estimate of the maximum wind and radius of maximum wind, the pressure drop (P_n-P_c) was represented in terms of the maximum wind by substituting (71) in (70) to obtain

$$W_m = [(k/\rho_a e)(P_n - P_c)]^{\frac{1}{2}}. \qquad (72)$$

Using (71) and (72), (68) reduces to

$$W_g = [(R/r)^k W_m^2 \exp(1-(R/r)^k) + (\tfrac{1}{2}rf)^2]^{\frac{1}{2}} - \tfrac{1}{2}rf. \qquad (73)$$

It should be remarked that for k=1, this wind model is equivalent to the NWS-23 model. Another important point to note is that the azimuthal variation of k automatically results in an asymmetry of the wind field due to the translation of the storm. From the NWS-23 model, this asymmetry has to be taken into account by augmenting the maximum wind speed with the forward speed of the storm and the cosine of the angle that depends upon the location of the maximum wind relative to the storm path.

b) Analytical pressure model

The pressure profiles obtained from (69) using k obtained from fitting the velocity profiles were not in good agreement with the observed pressure profiles. This confirms Holland's remark as mentioned earlier. Therefore, the pressure profile

$$P = P_c + (P_n - P_c)e^{(-R/r)}, \tag{74}$$

which is equivalent to (69) with k=1, was employed in this study.

CHAPTER III

SIMULATIONS OF HURRICANES OF RECORD

1. Selected hurricanes of record

Eligible hurricanes of record for the purposes of this study
were considered as those storms for which the historical information
required by the numerical model was available. This includes the
time series of the central pressure, radius of maximum wind and
surface charts of wind and pressure. These charts should cover the
entire Gulf of Mexico and Cayman Sea from the time at which the storm
center was outside the Gulf to sometime after landfall. Additional
important data required includes the water level associated with
these storms at stations around the Gulf, in both the United States
and Mexico.

Of the 26 hurricanes spanning the period 1950-1980 which were
examined as potential hurricanes of record, only hurricanes Carla in
1961 and Allen in 1980 had sufficient observations of the forcing
fields and the response histories. These are the hurricanes of
record used for verification purposes in this study.

Hurricane Carla was an exceptionally slow moving storm with an
average forward speed of 13 km/h. Figure 5 shows the path indicated
by serial positions of the storm's center at six hour intervals.
Carla reached hurricane stage at 1200 GMT 6 September 1961 and the
center entered the Gulf through Yucatan Strait at approximately 1500
GMT 7 September with a central pressure of 970 mb. As it moved to
the northwest, it continuously deepened and reached a minimum central
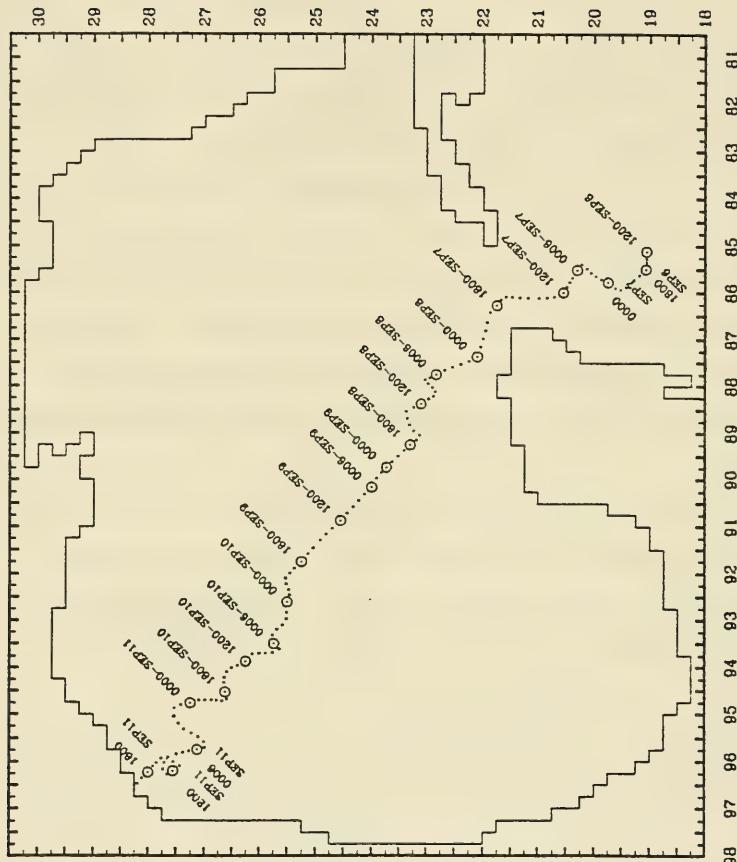
Fig. 5. Track of hurricane Carla from 1200 GMT 6 September to 1800 GMT 11 September 1961.

38

pressure of 935 mb at 1200 GMT 11 September. The time sequence of
the central pressure from September 4 to September 13, Fig. 6, was
presented by Dunn et al. (1962). During the period 1200 GMT 9
September through 1800 GMT 12 September, the average radius of
maximum wind was approximately 40 km with a slight increase observed.
Upon entering the Gulf, Carla had winds of 60 km/h. As it drifted
northwest, then west northwest it increased in size with cyclonic
winds observed over the entire Gulf. Maximum wind speeds of 82 km/h
were observed inland as Carla approached the coast. Carla made
landfall near Pass Cavallo at 2100 GMT 11 September and by 12
September it was positioned north of Waco. Hurricane Carla has the
distinction of being the best documented storm in history.

Hurricane Allen was a fast moving storm compared to Carla. Its
average forward speed in the Cayman Sea was 35 km/h. Its forward
speed decelerated to about 30 km/h as it moved west-northwest across
the Gulf. The center of the storm entered Yucatan Strait at
approximately 1800 GMT 7 August, 1980. The hurricane center crossed
the coastline near Brownsville at 0700 GMT 10 August. Figure 7 shows
the path of Allen from the Cayman Sea until landfall.

The time sequence of Allen's central pressure, as shown in Fig.
8, was obtained from Lawrence and Pelissier (1981). There were three
cycles of a 50 mb fluctuation in the six-day period from 4-10 August.
The first minimum central pressure of 911 mb occurred early on 5
August when the storm was approximately 370 km south of Puerto Rico.
The next minimum of 899 mb was measured at 1742 GMT 7 August when the
eye just passed through the strait. Allen deepened for the third
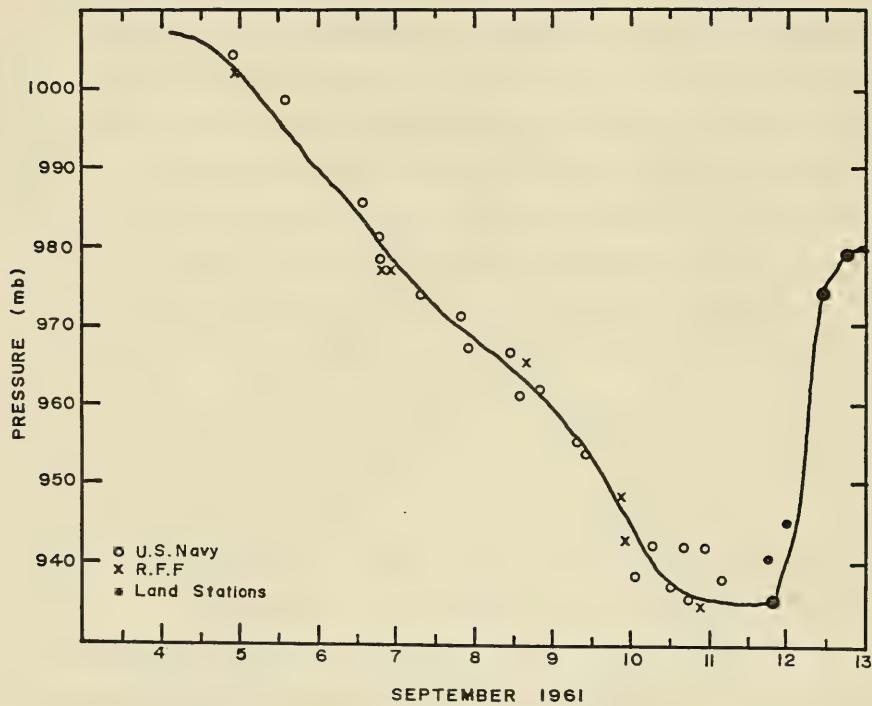
Fig. 6. Time sequence of Carla central pressure 4 - 13 September, 1961 (after Dunn et al., 1962).

Fig. 7. Track of hurricane Allen from 0000 GMT 7 August to 1200 GMT 12 August 1980.

41
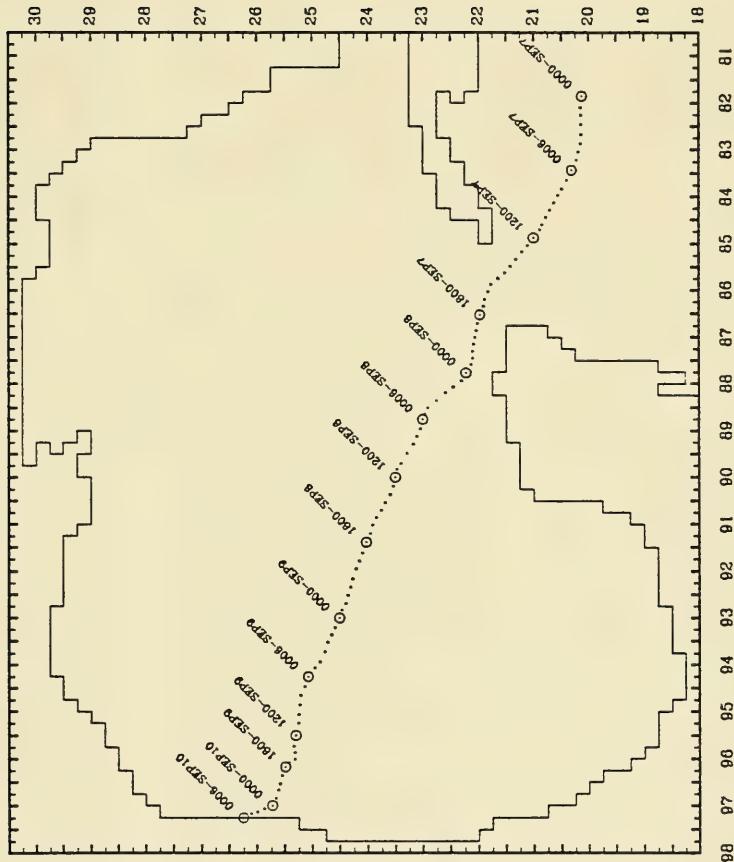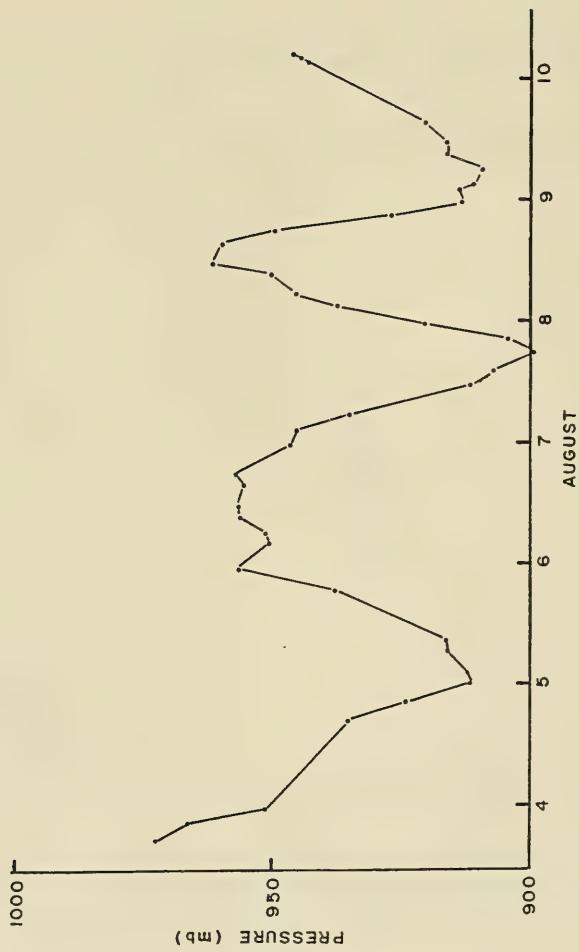
Fig. 8. Time sequence of Allen central pressure 4 – 10 August, 1980 (after Lawrence and Pelissier, 1981).

42

time when it moved toward Texas coast and reached a 909 mb low early on 9 August local time.

2. Meteorological data

The Hydrometeorological Section of the U.S. Weather Bureau provided surface charts of hurricane Carla winds and pressure for the entire Gulf of Mexico. These charts were available at 6 h intervals from 1200 GMT 9 September to 1200 GMT 10 September and at 3 h intervals thereafter. Prior to this period, the surface pressure charts that covered North America, obtained from the National Climatic Center, provided observed surface winds from land stations, a bouy and ships of opportunity.

Ho and Miller (1980) presented several surface wind charts for the period when Allen was in the western Gulf. The coverage of these charts is limited to the western Gulf only. Despite the lack of surface wind charts however, the time sequence of the central pressure and the available surface pressure charts provided enough information to construct surface wind fields. However, this information was not sufficient to provide the same degree of detail as obtained with hurricane Carla.

a) Surface wind for hurricane Carla

The hurricane Carla surface wind charts were analyzed to determine the location of the eye and R, W_m and k which were required for the computation of wind fields.

43

The position of the eye and the radius of maximum wind were first determined. To account for the asymmetry of the wind fields, k was determined by fitting the observed radial wind profiles along different sectants around the eye. A total of 8 profiles was fitted for each chart. Figure 9 shows sections where these profiles were fitted. In each case, the profile was plotted by digitizing the radial distance from the center to the isovels on the observed chart. The maximum wind speed, W_m, was determined from the plot at the distance R from the center. The radial wind profile was computed from (73) by substituting R, W_m and assuming k=1. The resulting profile was compared to the observed and k was adjusted to obtain the best possible agreement.

Prior to 1200 GMT 9 September, during which there were no regional Carla surface wind charts, the analysis to obtain R, W_m and k depended upon the surface pressure charts from the National Climatic Center. Eq. 68 was rewritten, by using (71), as

$$W = [(R/r)^k (k/\rho_a)(P_n - P_c) e^{-(R/r)^k} + (\tfrac{1}{2}rf)^2]^{\tfrac{1}{2}} - \tfrac{1}{2}rf. \qquad (75)$$

The time sequence of the radius of maximum wind was extrapolated back in time using its relation to the central pressure which is summarized in NWS-23. The radial distances to those points where observed winds were reported, were digitized from the surface chart. The far field pressure was determined from the first cyclonically curved isobar. Assuming ρ_a = 1.15 Kg/m^3 and k=1, the wind speed computed from (75) was compared to the observed value and again k was adjusted to obtain minimum error. Once k was determined, W_m was
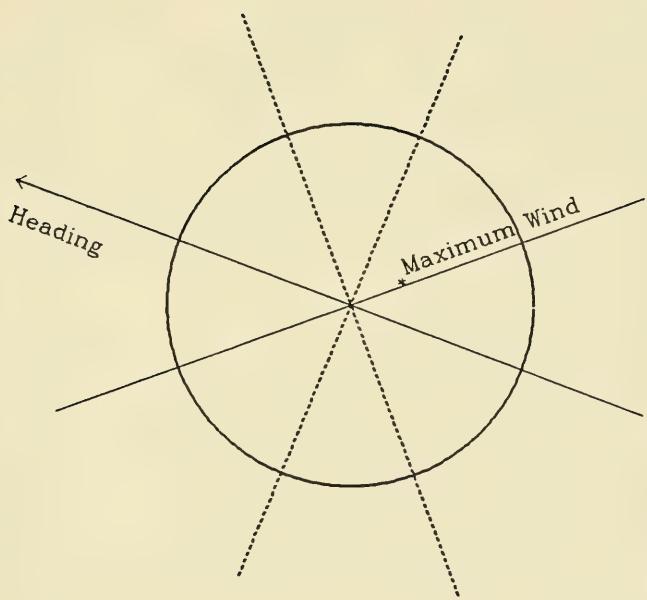
Fig. 9. Schematic showing azimuthal distribution of radial sections where wind profiles were fitted.

computed from (72).

Attempts were made to obtain a simple expression for both k and W_m as a function of the azimuthal angle (measured from the north) such that these two parameters could be internally computed. However, no simple relationship could be established due to the complexities of the patterns of azimuthal variation of k and W_m which, in addition, varied irregularly for each map time. Therefore, these parameters have to be specified serially. Furthermore, linear interpolation in time to obtain these parameters for intermediate time step computations constrained the values to the same set of azimuths (relative to heading) throughout the simulation period. As a result, an a priori linear interpolation in space was employed to get k and W_m as continuous functions of azimuth. A standard set of azimuths was then selected.

Finally, the surface wind fields for each map time were constructed using the interpolational routine employed in the model. Comparison between the computed and observed wind fields was made and final adjustments of k, if necessary, were decided. Figures 10 and 11 are examples of the computed wind fields at 0000 GMT 7 September and 1200 GMT 9 September, respectively. The solid circles indicate the observed wind speed from the surface charts.

b) Surface wind for hurricane Allen

The inadequate coverage in both space and time of surface wind charts for hurricane Allen aborted attempts to fully analyze these charts as practiced in hurricane Carla. Therefore, NWS-23 was used
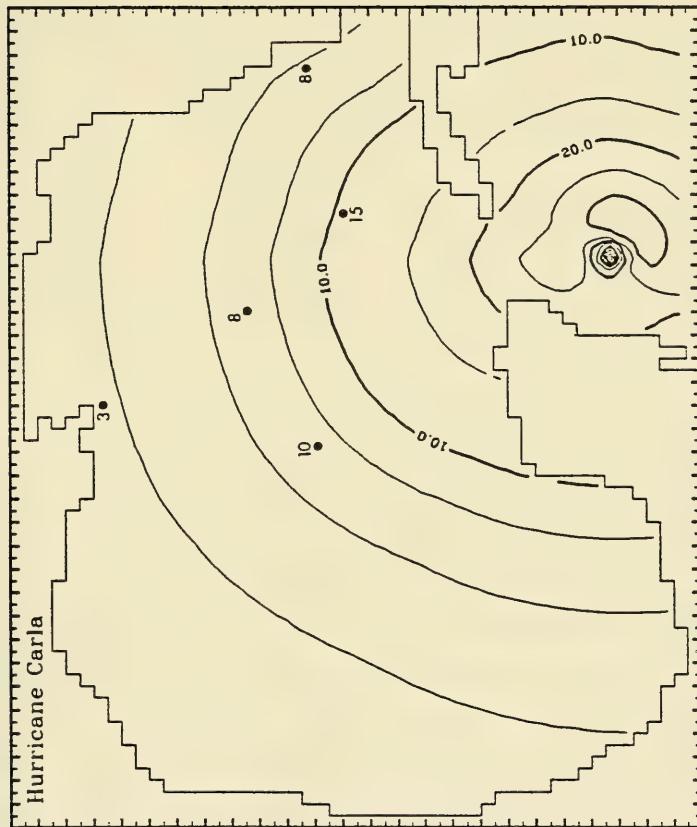
Fig. 10. Hurricane Carla surface wind (m/s) at 0000 GMT 7 September 1961, as obtained from Holland's model. The solid circles indicate the observed wind speed from the surface chart.
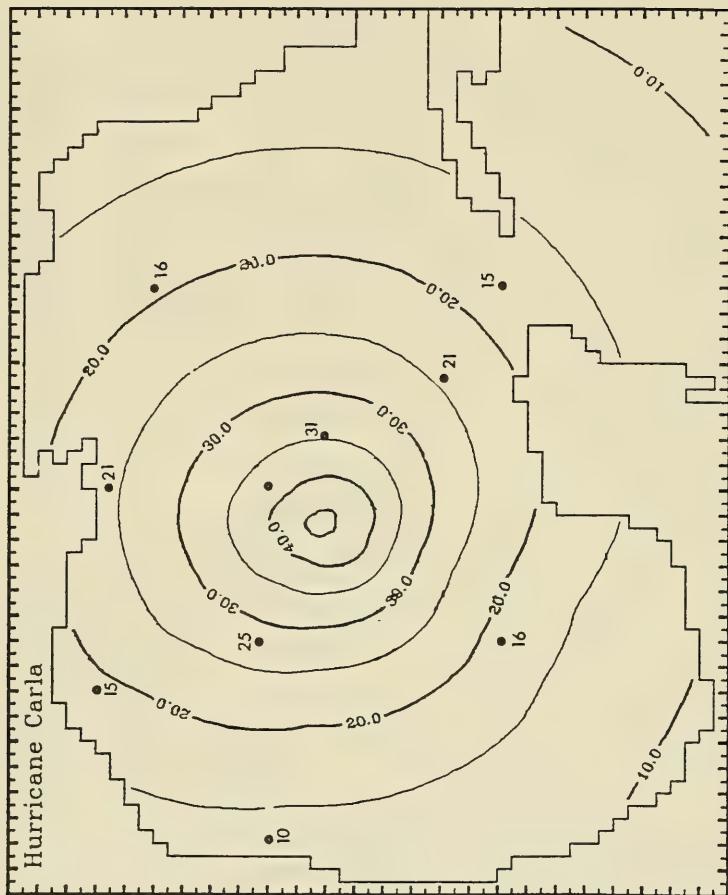
Fig. 11. Hurricane Carla surface wind (m/s) at 1200 GMT 9 September 1961, as obtained from Holland's model. The solid circles indicate the observed wind speed from the the surface chart.

48

to determine R and W_m from P_c which were required to construct the wind fields. The graphical relationship between the radius of maximum wind and the central pressure was analyzed using simple linear regression to establish a functional relationship. The radius of maximum wind was then determined. The maximum wind speed for a stationary storm W_{ms}, is given as

$$W_{ms} = 0.9(1/\rho e)^{\frac{1}{2}}(P_n - P_c)^{\frac{1}{2}} - (Rf/2) \qquad (76)$$

Since there were no surface charts to analyze for the parameter k, a constant value of 1 was assumed. As discussed earlier, the asymmetry of the wind field was achieved by augmenting the maximum wind speed by

$$W_m = W_{ms} + 1.5(V_f^{0.63})(T_o^{0.37})\cos\sigma, \qquad (77)$$

where σ was the angle between track direction and the surface wind vector and $T_o = 0.514791$ for wind speed in m/s. The track of hurricane Allen was approximately 285° (cf. Fig. 7, p. 41) relative to true north. Assuming that the maximum wind occurred at right angles to the right of the track, then σ was zero at 25° relative to true north. Eq. (78) was used to compute the maximum wind speed for each grid point (I,J) and thus the surface wind speed at all computational points can then be evaluated.

3. Tide gauge data

A total of 9 and 13 tide gauge stations for hurricane Carla and Allen, respectively, were chosen to provide the observed response in the Gulf of Mexico. Figure 12 shows locations of these tide gauge stations. The Tides Prediction Branch of the National Oceanic and Atmospheric Administration (NOAA) and the National Autonomous University of Mexico (UNAM) provided hourly water level for a period of several weeks before and after the hurricanes. Filtered versions (using a 40 h lowpass filter) are shown in Figs. 13-15 for some selected series obtained during hurricane Carla. These filtered plots essentially remove the tides. The arrows in the figures indicate the time at which the center of Carla entered the Gulf through Yucatan Strait. There were indications of a gradual rise of water level well before the peak surge, a possibility of forerunner surges at all 9 stations. Note also the degree of background variation unrelated to the hurricane several weeks prior to the hurricane.

The same analysis as applied to recorded water level for hurricane Carla were used for the records obtained obtained during hurricane Allen. Figures 16-18 show the filtered data at some selected stations. The presence of an initial rise in water level is again observed at all stations.

The lowpass filtering illustrated above is known to smooth out and broaden the peak surge. To properly remove tidal signals from recorded data by the harmonic method requires a suitable number of constituents to insure proper phasing. Unfortunately, only the Key

50
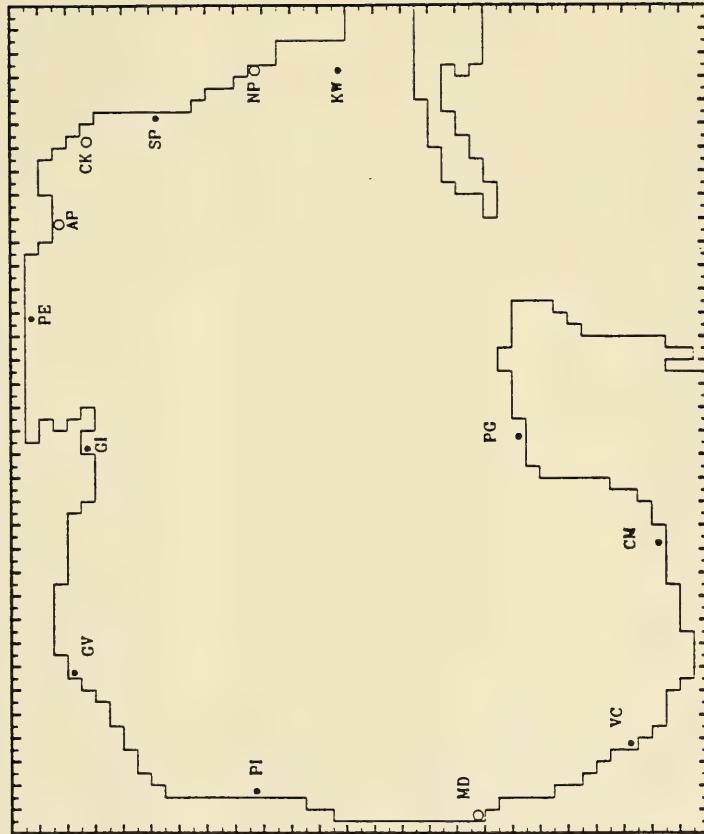
Fig. 12. Locations of tide gauge stations used in this study. KW is Key West, NP is Naples, SP is St. Petersburg, CK is Cedar Key, AP is Apalachicola, PE is Pensacola, GI is Grand Isle, GV is Galveston, PI is Port Isabel, MD is Madero, VC is Veracruz, CM is Carmen, PG is Progreso. The solid circles indicate those stations used in the simulation of hurricane Carla. Both the solid and open circles are those used in the simulations of hurricane Allen and also as the model tide gauge stations in the parametric study.
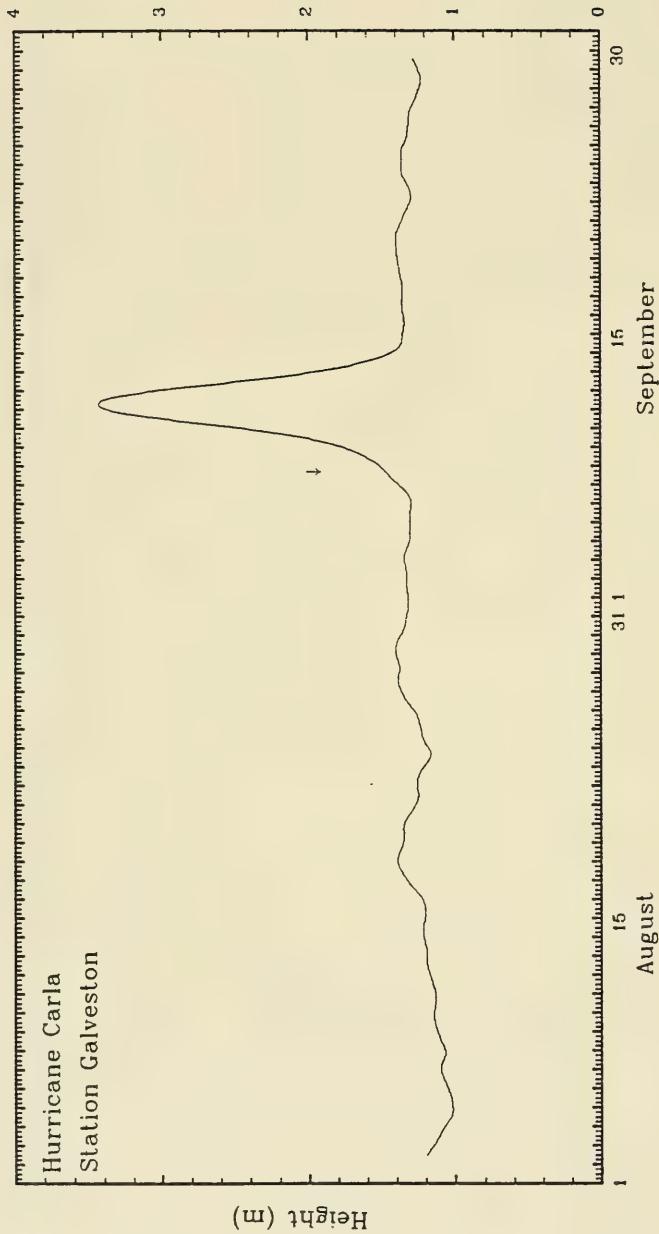
Fig. 13. Observed water levels at Galveston during hurricane Carla, 1961. The arrow indicates the time at which Carla entered the Gulf through Yucatan Strait. The datum is gauge mean low water.

52
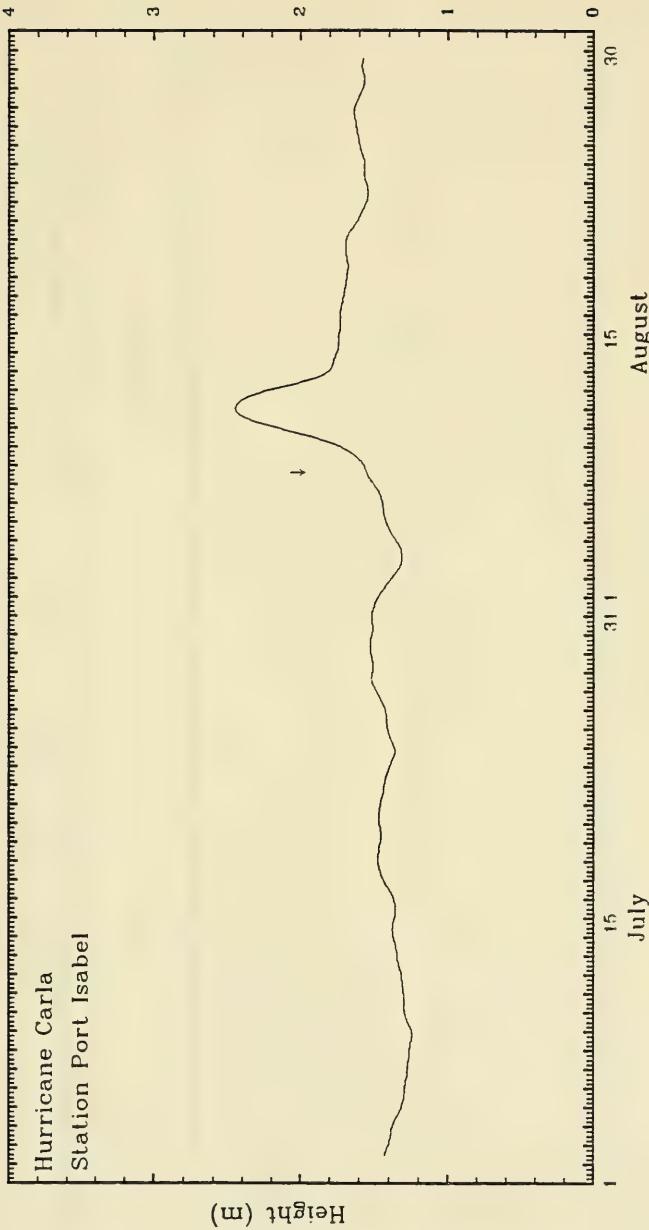
Fig. 14. Observed water levels at Port Isabel during hurricane Carla, 1961. The arrow indicates the time at which Carla entered the Gulf through Yucatan Strait. The datum is gauge mean low water.
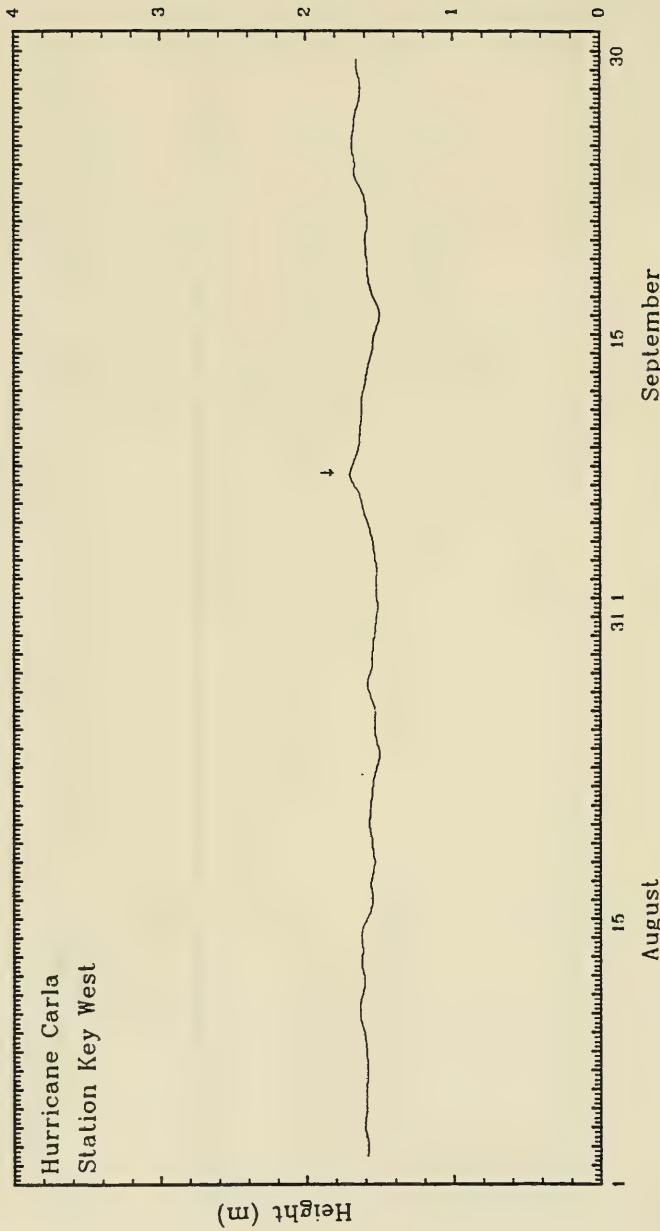
Fig. 15. Observed water levels at Key West during hurricane Carla, 1961. The arrow indicates the time at which Carla entered the Gulf through Yucatan Strait. The datum is gauge mean low water.

Fig. 16. Observed water levels at Galveston during hurricane Allen, 1980. The arrow indicates the time at which Allen entered the Gulf through Yucatan Strait. The datum is gauge mean low water.
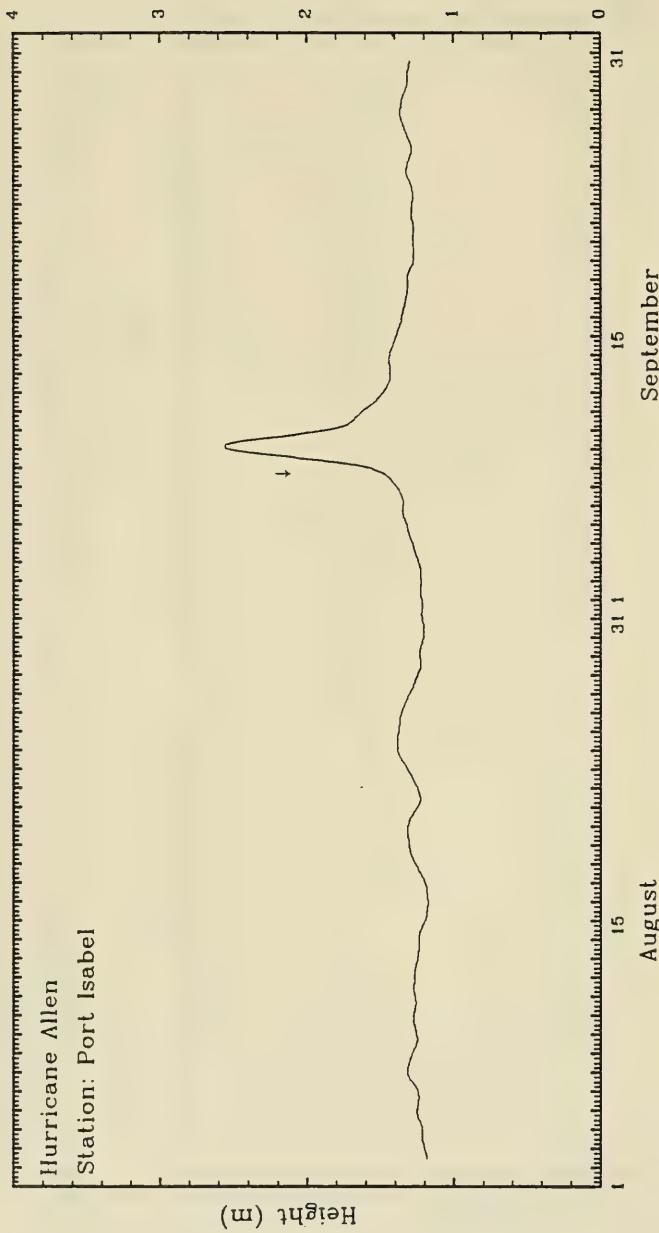
Fig. 17. Observed water levels at Port Isabel during hurricane Allen, 1980. The arrow indicates the time at which Allen entered the Gulf through Yucatan Strait. The datum is gauge mean low water.

56
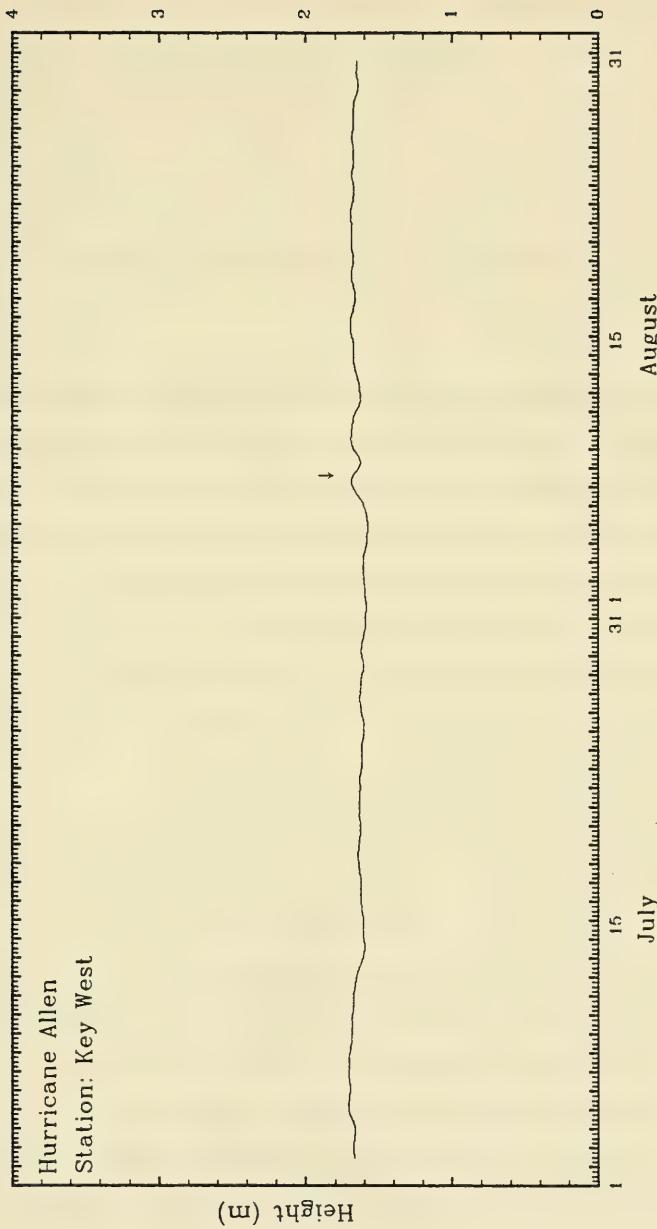
Fig. 18. Observed water levels at Key West during hurricane Allen, 1980. The arrow indicates the time at which Allen entered the Gulf through Yucatan Strait. The datum is gauge mean low water.

West and Galveston stations have enough information for the actual computation of the tide. Therefore, at each station, only the mean water level during the period considered, excluding the peak surge, was removed from the raw data. Thus the recorded hydrographs which are compared to those computed contain the tidal signal, but its amplitude is small and does not unduly complicate the comparison.

4. Simulation procedure

The initial model wind and pressure fields were increased in amplitude linearly from zero to their actual initial values over a 48 hour prototype time period. During this period Carla was kept stationary at $19.04°N$ and $85.15°W$ which was its position at 1200 GMT 6 September. The simulation was carried out to 0000 GMT 13 September, approximately 28 h after landfall.

The simulation for hurricane Allen starts at 0000 GMT 7 August and ends at 0000 GMT 12 August. The initial position of the eye of hurricane Allen during start up was at $20.10°N$ and $81.90°W$.

At each time step the east and north component of wind stress and the atmospheric pressure (the inverted barometric height) were computed at each grid point. The sequence of wind and pressure computations consisted of two linear interpolations. First, the position of the eye and the other parameters at each time step were linearly interpolated from two appropriate sets of values (6 h apart). The radial distance from the eye to each individual grid point (I,J) was computed. The inverted barometric height was then computed from (74). The angle between the line joining the eye to

58

the grid point (I,J) and true north, $\tilde{\theta}$, was determined. The pair of azimuthal angles that embraced $\tilde{\theta}$ was sorted. The values of k and W_m associated with the two angles so determined were used in the linear interpolation to obtain their values at grid point (I,J).

A constant inflow angle of $20°$ was assumed in all simulations except Carla for the decomposition of the wind speed before computing the wind stress components. The computed water level at Galveston during the early stage of Carla simulation using constant inflow angle was lower than the observed. Careful examination of the surface wind charts at 1200 GMT 9 September revealed that there was a region along the Texas shelf where the cross shelf wind reversed direction indicating a negative inflow angle. An example of an analyzed wind map given by Miyasaki (1963), also shows negative inflow angles along the Texas shelf. Therefore, the inflow angle was allowed to vary as a function of the radial distance using the empirically determined formula

$$\Theta = \begin{cases} \Theta_1 & \text{for } r < R_1, \\ \\ \Theta_2 - (r-R_1)*0.5*A/r & \text{for } r > R_1, \end{cases} \tag{78}$$

where A is a maximum inflow angle, $20°$, R_1 is the radial distance at which the inflow angle was zero, and

$$\Theta_1 = [(R_1/r)A^2 \exp(1-(R_1/r))+(\tfrac{1}{2}rf)^2] - \tfrac{1}{2}rf,$$

$$\Theta_2 = [(R_1/r)^K A^2 \exp(1-(R_1/r)^K)+(\tfrac{1}{2}rf)^2] - \tfrac{1}{2}rf,$$

$$K = r/50 \ .$$

Figure 19 shows the adopted inflow angle profile. This radially varying inflow angle was applied only from the begining of the simulation to 0000 GMT 10 September. A constant inflow angle was resumed after this period since there was no other evidence of negative inflow angles on the remaining available surface charts.

Results of the simulation were sampled every 24 hour prototype time. These included digital fields and map plots of the height anomalies and currents for both modes, and surface currents whose values were retrieved from the modal currents. At the end of the simulation, the computed and observed hydrographs at the tide stations were plotted. Contours of the peak surge on the continental shelf for the entire Gulf of Mexico and for the Texas-Louisiana shelf were also plotted.

5. Results of Carla simulation

Figures 20 through 28 show the computed (solid) and recorded (dashed) hydrographs at the stations used in this study. The overall comparisons are fair, especially during the first half of the simulation period. There is not much activity in the southwestern portion of the Gulf (Campeche Bay) as revealed from the hydrographs from the three Mexican stations (Figs. 26 through 28). The simulated hydrograph at Key West has a slow oscillation with a period of approximately 7 days. The mean of this long period oscillation lies close to the mean of the recorded water level. This signal is also observable in the St. Petersburg computed hydrograph. However, the

60
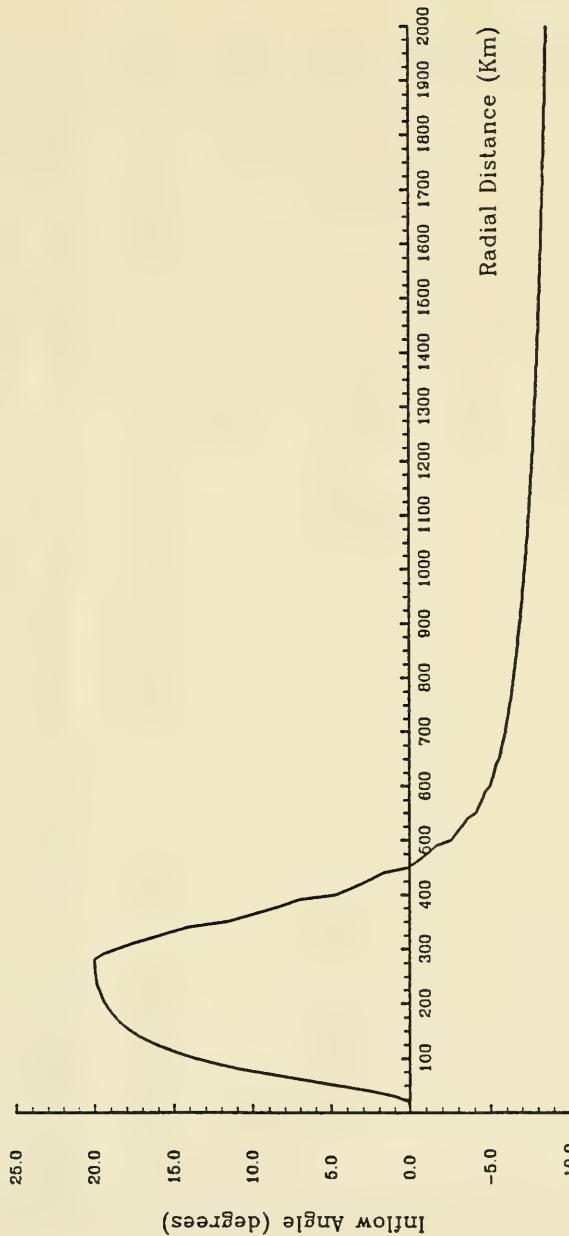
Fig. 19. Radial profile of the inflow angles computed from (78).

61
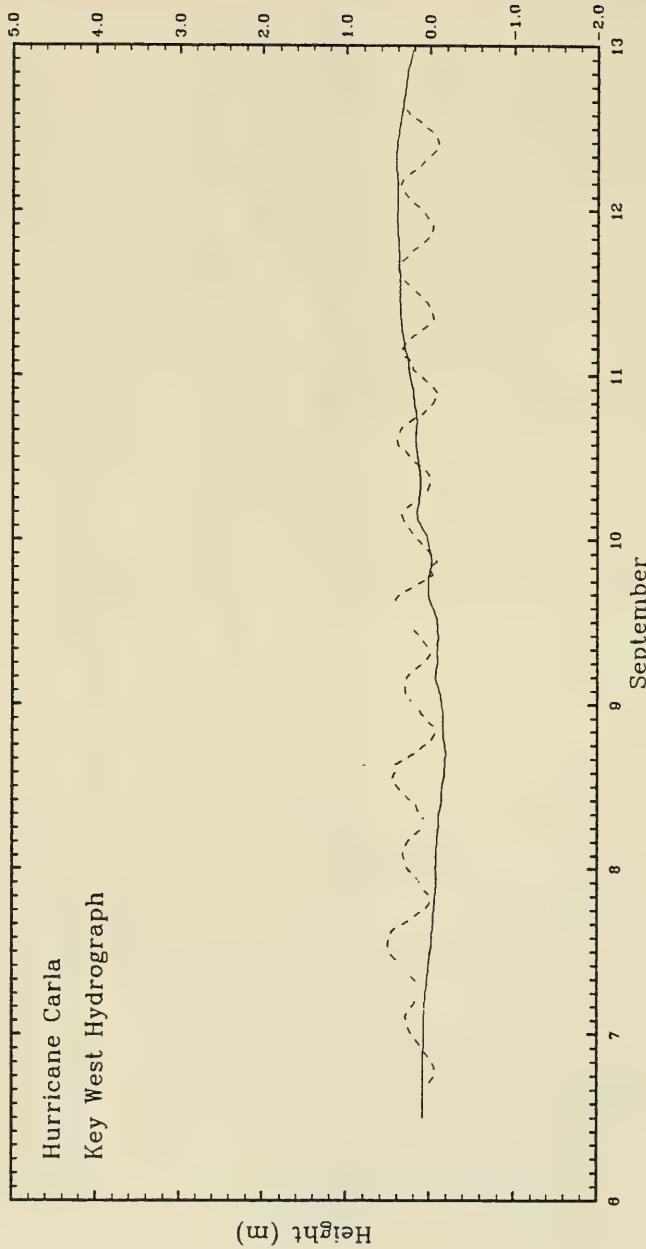
Fig. 20. Computed (solid) and observed (dashed) hydrographs at Key West during hurricane Carla 6 - 13 September 1961. The datum is mean sea level.
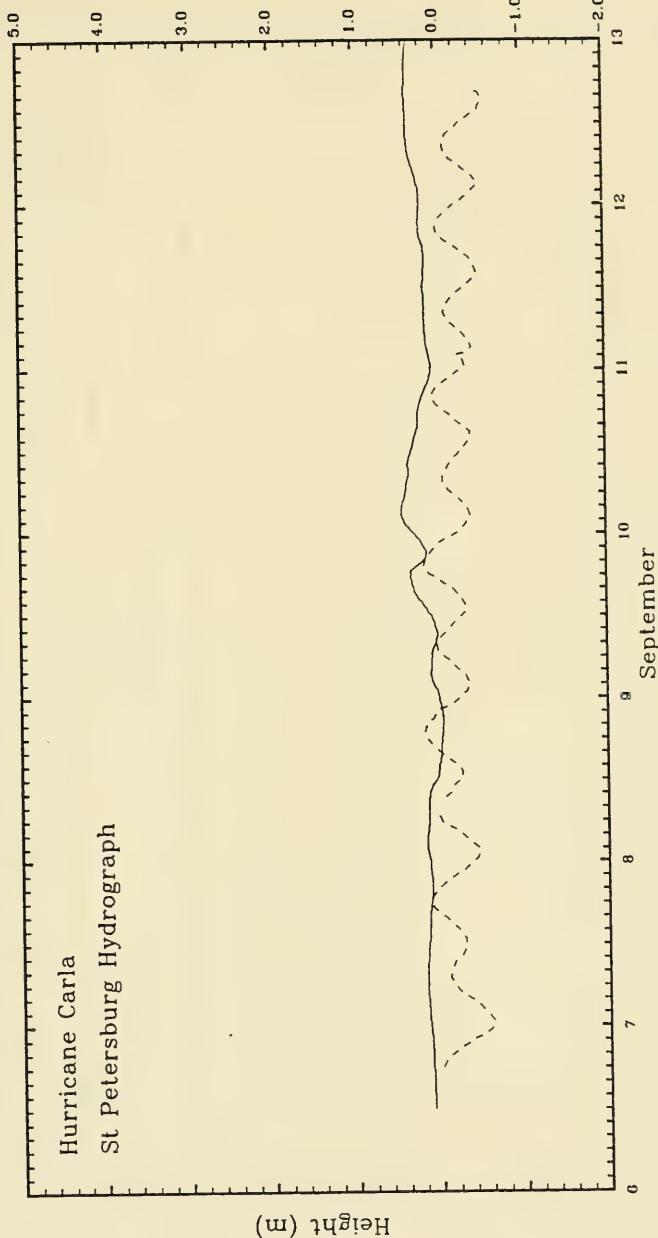
Fig. 21. Computed (solid) and observed (dashed) hydrographs at St. Petersburg during hurricane Carla
6 - 13 September 1961. The datum is mean sea level.

63
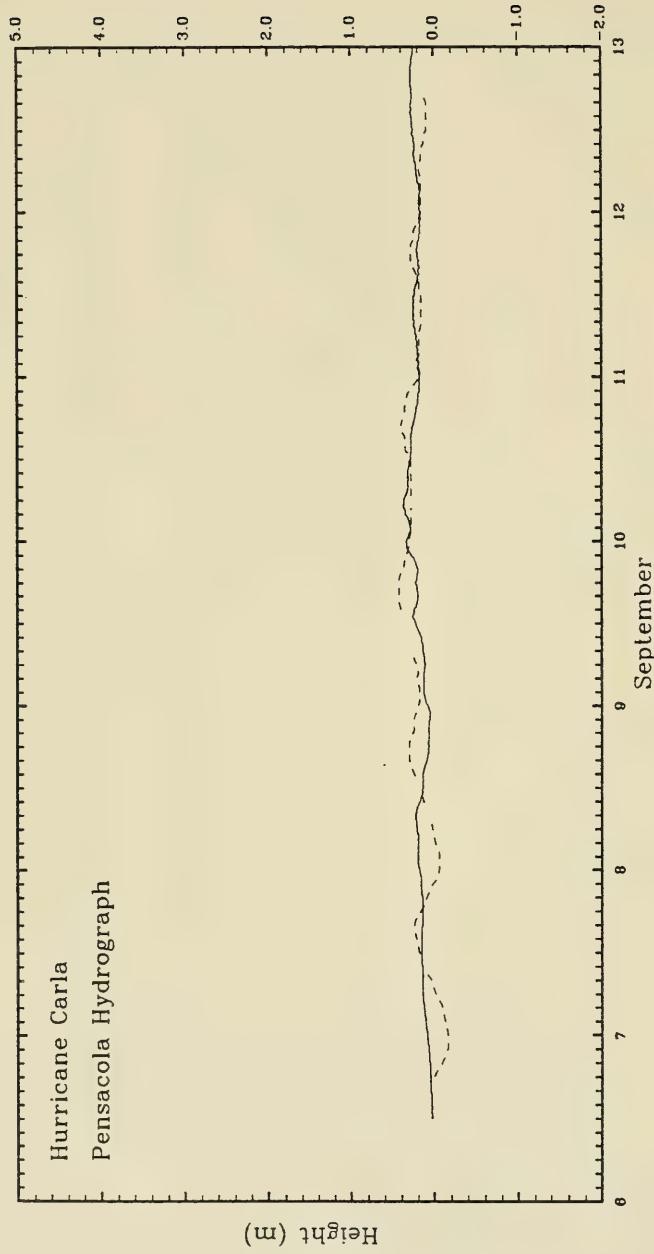
Fig. 22. Computed (solid) and observed (dashed) hydrographs at Pensacola during hurricane Carla 6 - 13 September 1961. The datum is mean sea level.

64
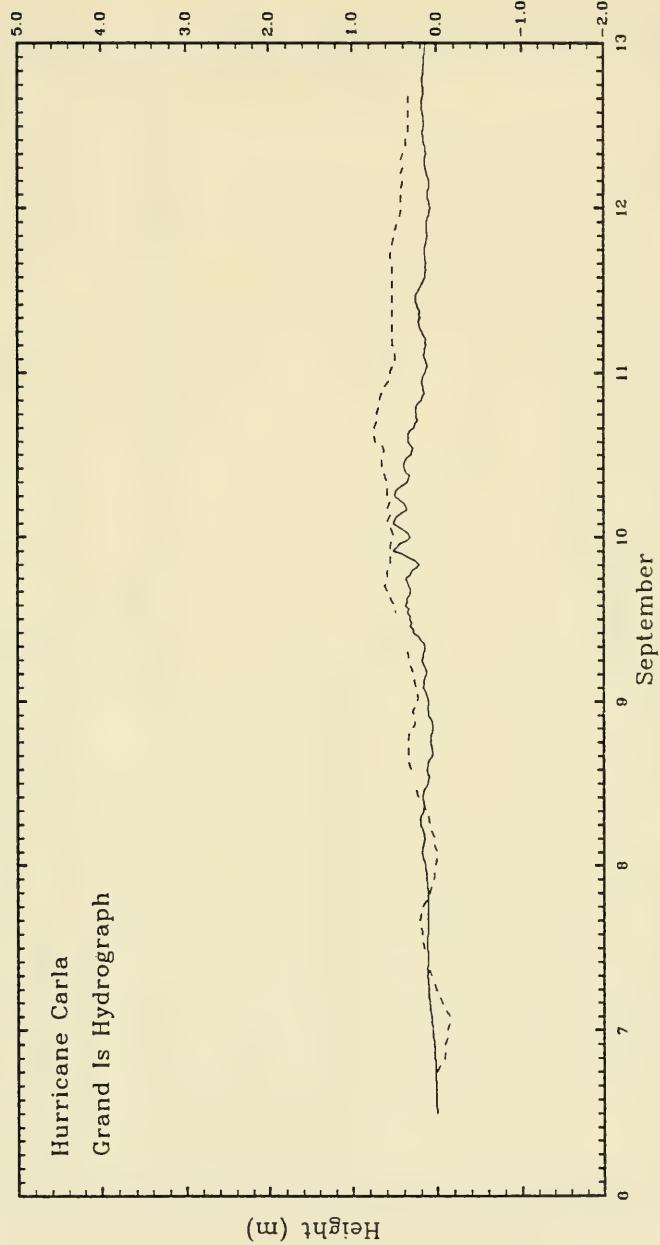
Fig. 23. Computed (solid) and observed (dashed) hydrographs at Grand Isle during hurricane Carla
6 - 13 September 1961. The datum is mean sea level.

65
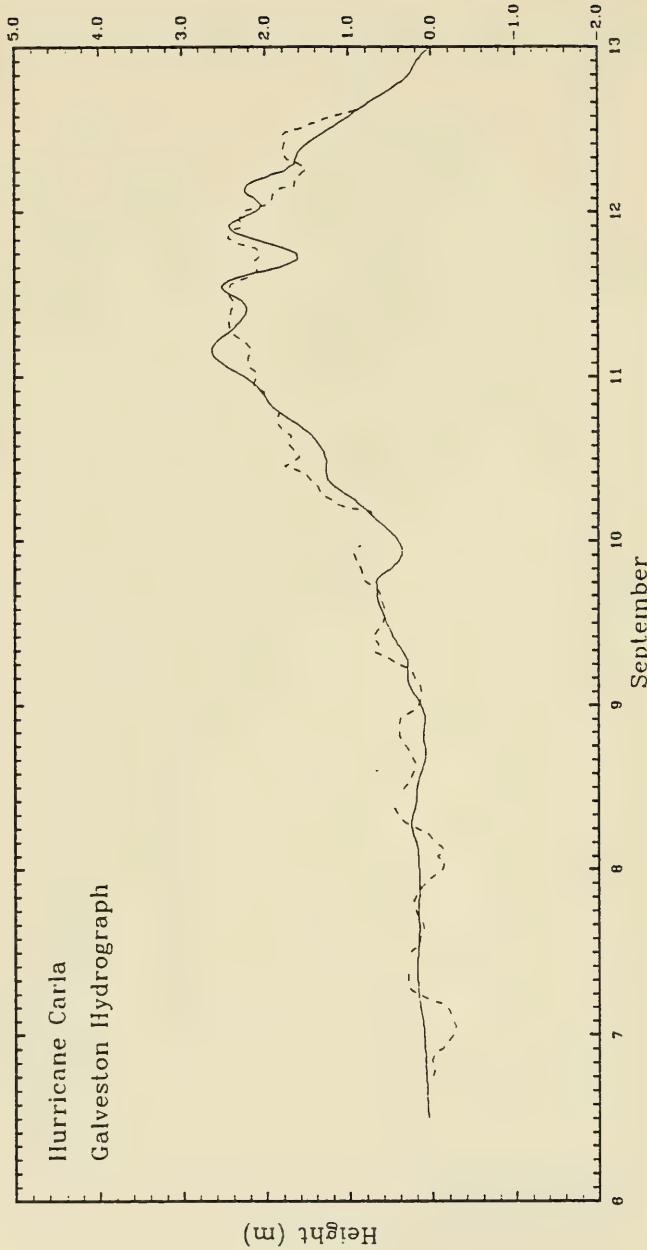
Fig. 24. Computed (solid) and observed (dashed) hydrographs at Galveston during hurricane Carla 6 - 13 September 1961. The datum is mean sea level.

66
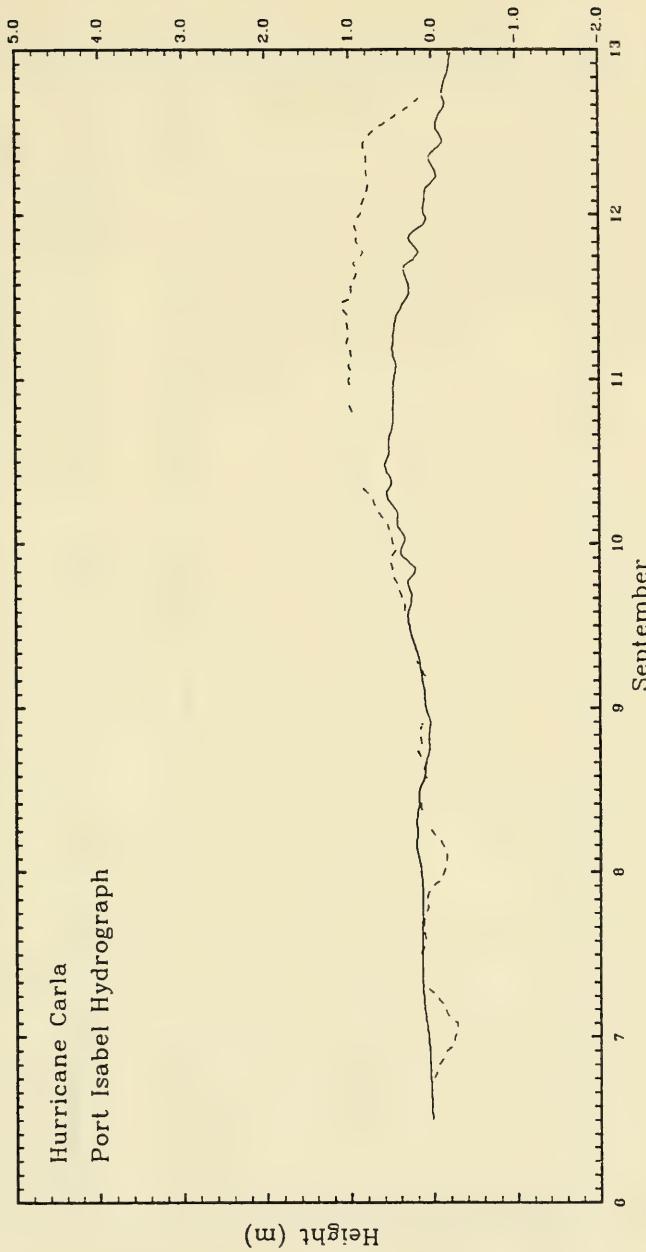
Fig. 25. Computed (solid) and observed (dashed) hydrographs at Port Isabel during hurricane Carla 6 – 13 September 1961. The datum is mean sea level.

67
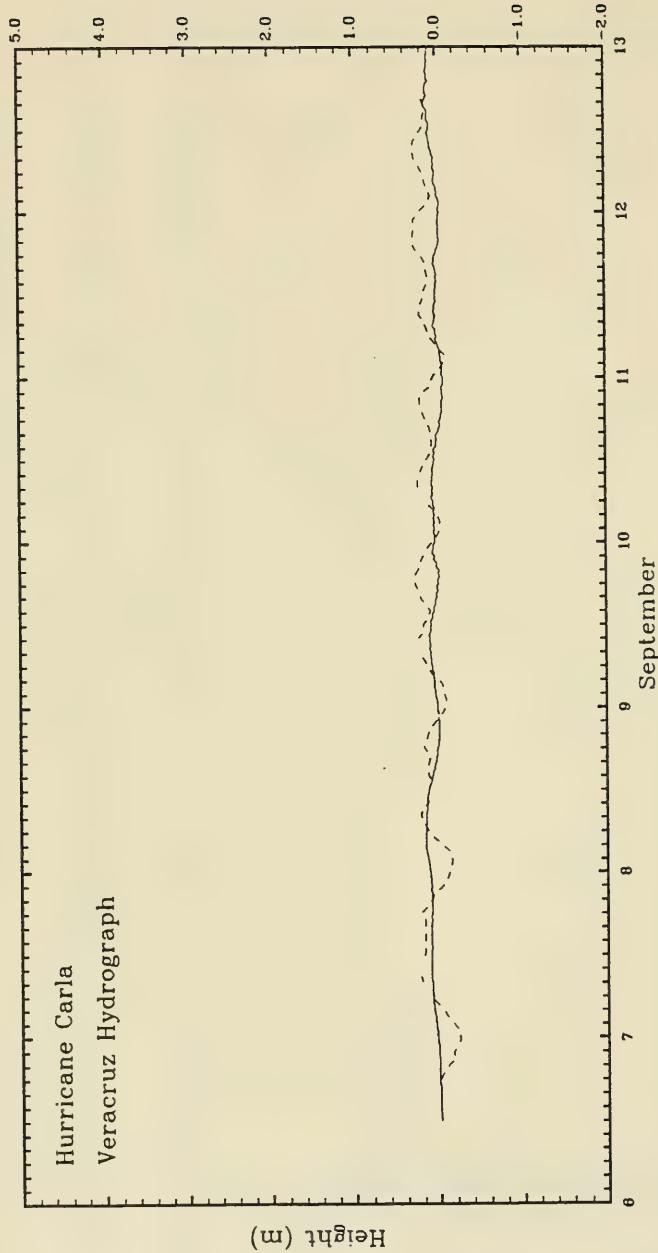
Fig. 26. Computed (solid) and observed (dashed) hydrographs at Veracruz during hurricane Carla
6 - 13 September 1961. The datum is mean sea level.

68
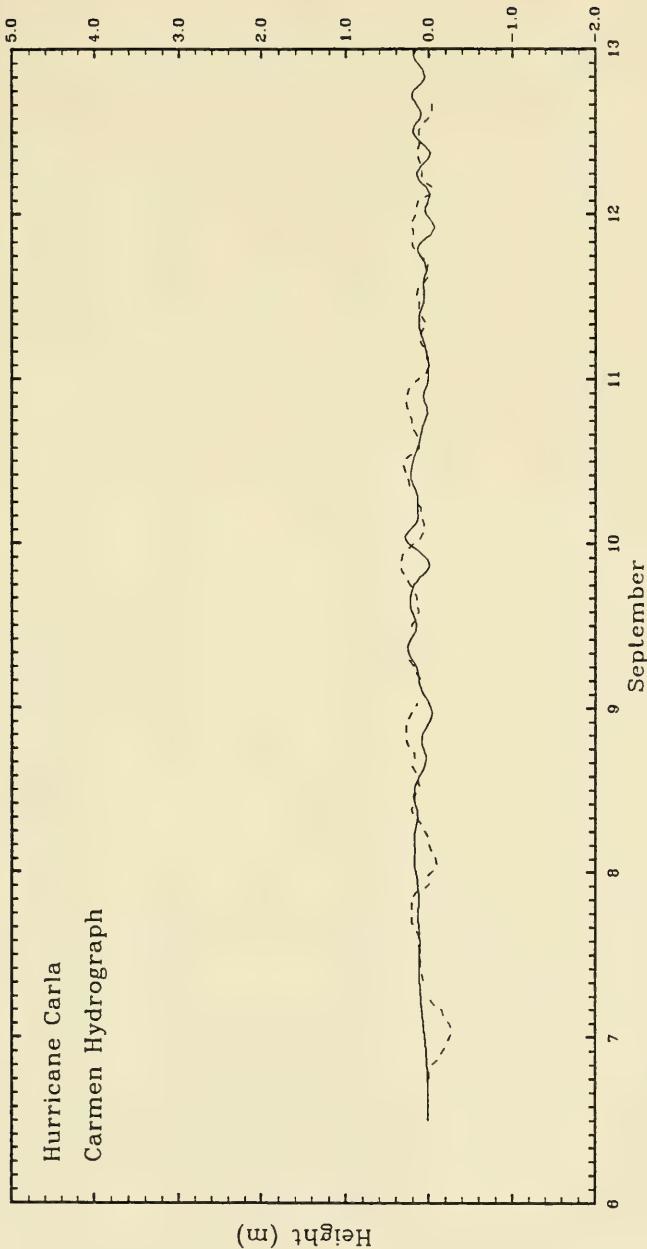
Fig. 27. Computed (solid) and observed (dashed) hydrographs at Carmen during hurricane Carla 6 - 13 September 1961. The datum is mean sea level.

69
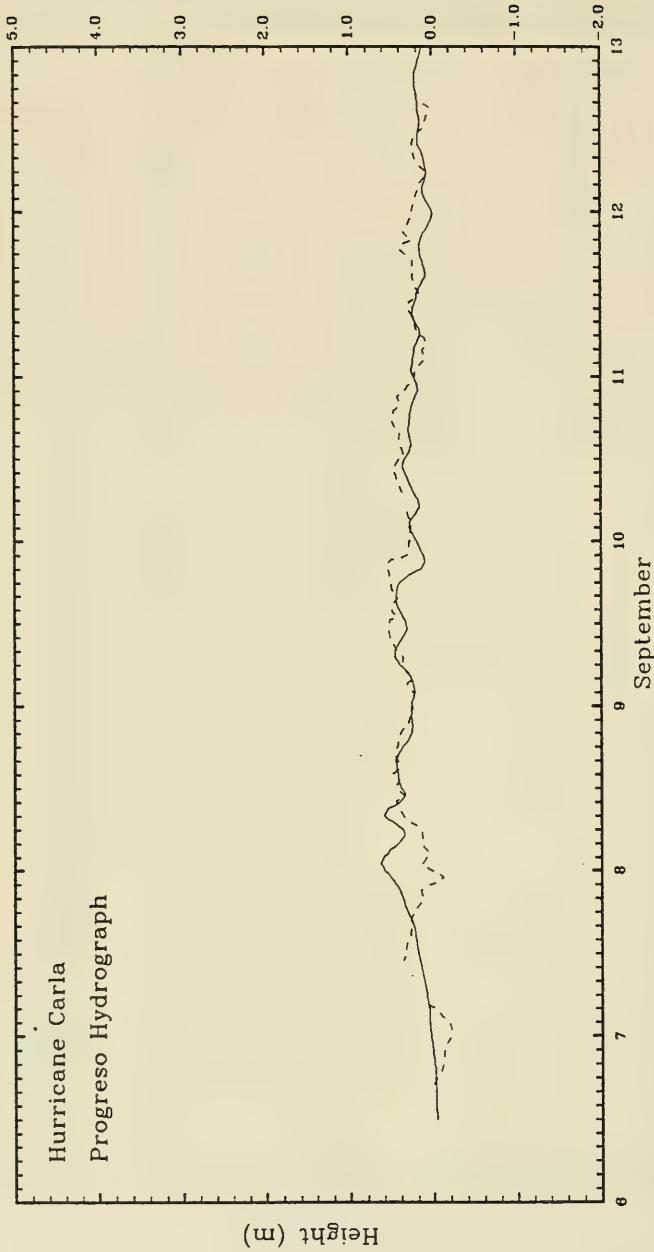
Fig. 28. Computed (solid) and observed (dashed) hydrographs at Progreso during hurricane Carla 6 - 13 September 1961. The datum is mean sea level.

70

computed water level at St. Petersburg is higher than the recorded throughout the period. This might be due to the fact that this tide gauge station is located inland and not on the open coast. The departure of the two hydrographs at Grand Isle is probably the result of resuming the 20° inflow angle which shifted the wind direction from the alongshore or slightly onshore to slightly offshore. The comparison for Galveston is better than that obtained by Miyasaki (1963), presumably because of the special care to match the observed wind fields for the northwest Gulf Coast. At Port Isabel, the discrepancy, which resembles that at Grand Isle but with a larger deviation, is possibly due to the difference in locations of the tide gauge station and the point where the computed water level was sampled. The actual site of the tide gauge station is inside a semi-enclosed embayment, as shown in Fig. 29. As a result, the effect of the offshore component of the wind, which prevailed at this station from approximately 0000 GMT 10 September onward, is limited while the southerly component produces a set up within the constricted lagoon at the gauge site. On the contrary, the computed hydrograph, sampled at half the grid size away from the digitized coastline, is subjected fully to the wind draw-down. Miyasaki (1963) obtained a similar result at this station.

Despite these discrepancies, the primary interest is the comparison at Galveston where the largest surge, among all sampled stations, occurs. It should be pointed out that the maximum computed water level is not at Galveston but at the grid point (8,42), located one grid block northeast of the path of Carla at the coast close to

71
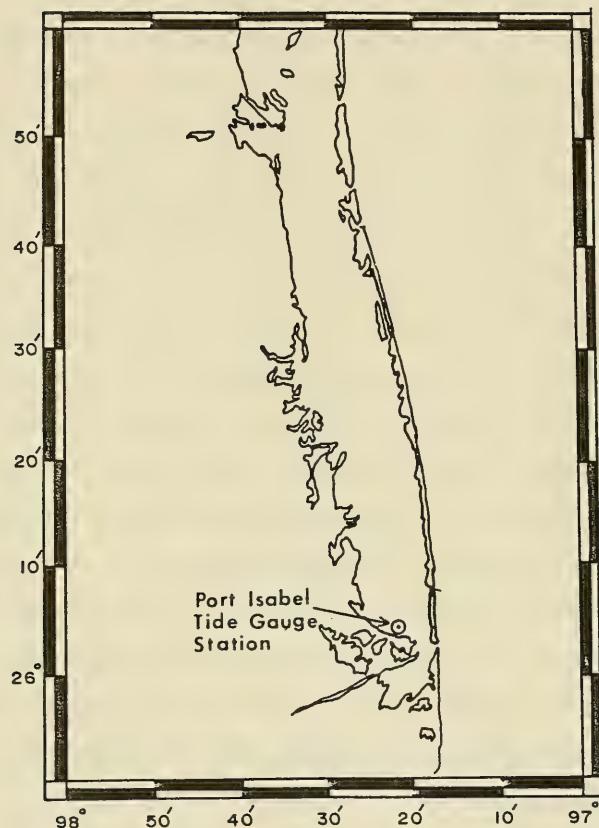
Fig. 29. Location of Port Isabel tide gauge station which is
sheltered by south Padre Island.

the location of Matagorda Bay where the highest high water marks were
observed for this hurricane. The agreement is good over the entire
simulation period at Galveston. The effect of the reversing inflow
angle in the simulation is clearly pronounced as the computed water
level suddenly drops at approimately 2200 GMT 9 September. This
result is somewhat out of phase with that indicated by the
observations.

Figures 30-32 show instantaneous fields of the barotropic and
baroclinic height anomalies and surface currents at 1200 GMT 10
September. Contours of the barotropic height (Fig. 30) clearly
demonstrate the inverted barometric effect around the storm center.
Upwelling along the hurricane path, a feature first investigated by
Leipper (1967) in the wake of hurricane Hilda in the Gulf of Mexico
in 1964, is noticeable in the baroclinic height field shown in Fig.
31. It should be remembered that the negative contours of the
baroclinic height anomalies correspond to upwelling of the interface.
Geisler (1970), in his linear analytic model, found that the
baroclinic response to a moving hurricane consisted of both upwelling
and inertio-gravity waves in the lee of the storm. Figures 31,32
strikingly portray this wake oscillation. Chang and Anthes (1978)
carried out numerical experiments to investigate the character of
this wake produced by various types of atmospheric forcing. They
found that the wavelength is longer for a faster moving storm and,
for the same forward speed of the storm, is shorter at higher
lattitude. In addition, within the limit of 50 h and 1200 km time
and space scales employed, the β-effect (variation of f) did not
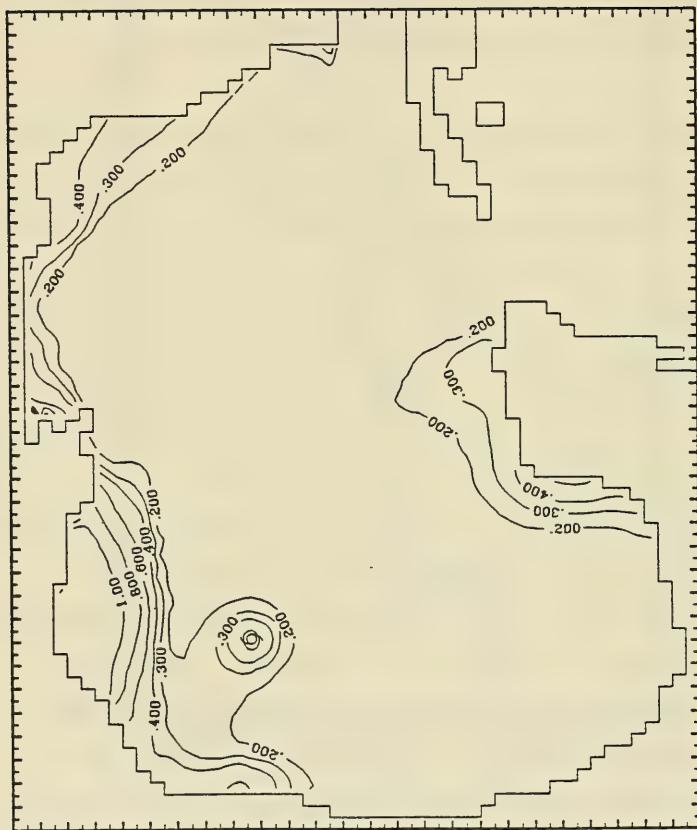
Fig. 30. Computed barotropic height anomaly field (meters) for hurricane Carla at 1200 GMT 10 September 1961.

74
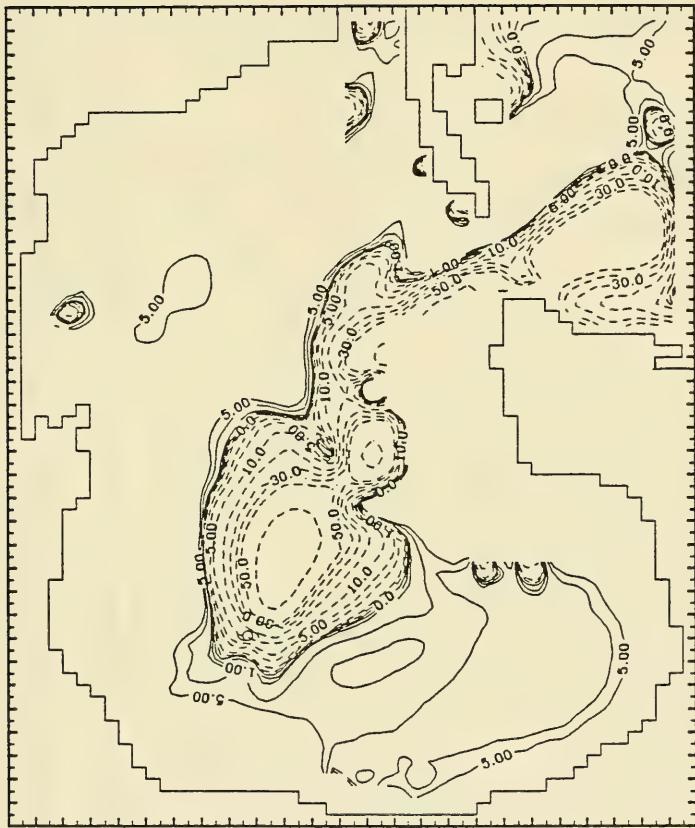
Fig. 31. Computed baroclinic height anomaly field (meters) for hurricane Carla at 1200 GMT 10 September 1961.

200.
MAXIMUM VECTOR
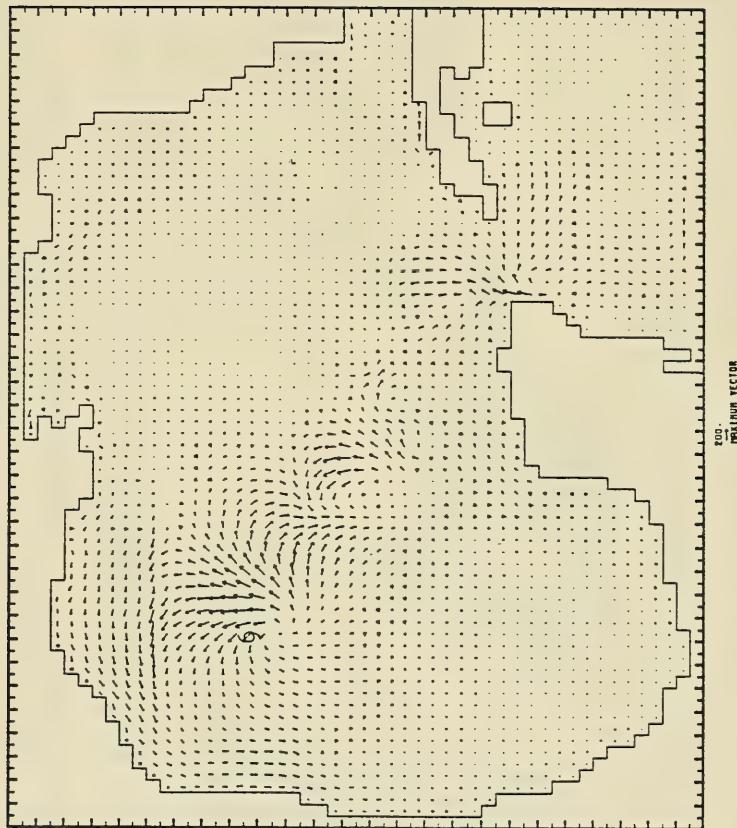
Fig. 32. Computed surface current field (cm/s) for hurricane Carla at 1200 GMT 10 September 1961.

76

alter the results. For an asymmetric storm moving at 18 km/h, which is comparable to the translation speed of Carla, in an idealized f-plane basin, the wake oscillation has a wave length of approximately 420 km. The average wave length obtained from this Carla simulation is approimately 360 km.

6. Results of Allen simulation

The results of the Allen simulation show a synchronous oscillatory signal with a period of approximately 28 h in all of the simulated hydrographs. The amplitude of this oscillation is approximately 20 cm. The existence of this in phase signal in all stations around the Gulf is indicative of a Gulf-wide, Helmholtz mode superimposed on other forced modes. Consequently, an *ad-hoc* code to compute the average water level in the Gulf proper (designated as η_G) at each time step was added. Figure 33 shows the time series of η_G. The solid line represents η_G computed by averaging water levels at each grid point in the Gulf, and the dashed line is η_G computed from the continuity equation using the difference of volume transports at the Florida and Yucatan ports. The two curves are practically coincident and very well matched with the signal present in the individually computed hydrographs mentioned above. As it can be seen in Fig. 33, this mode persisted throughout the entire simulation period.

The agreement between the simulated and observed hydrographs (Figs. 34-46) is comparable to that obtained in the Carla simulation. This is surprising since less information regarding the atmospheric

77
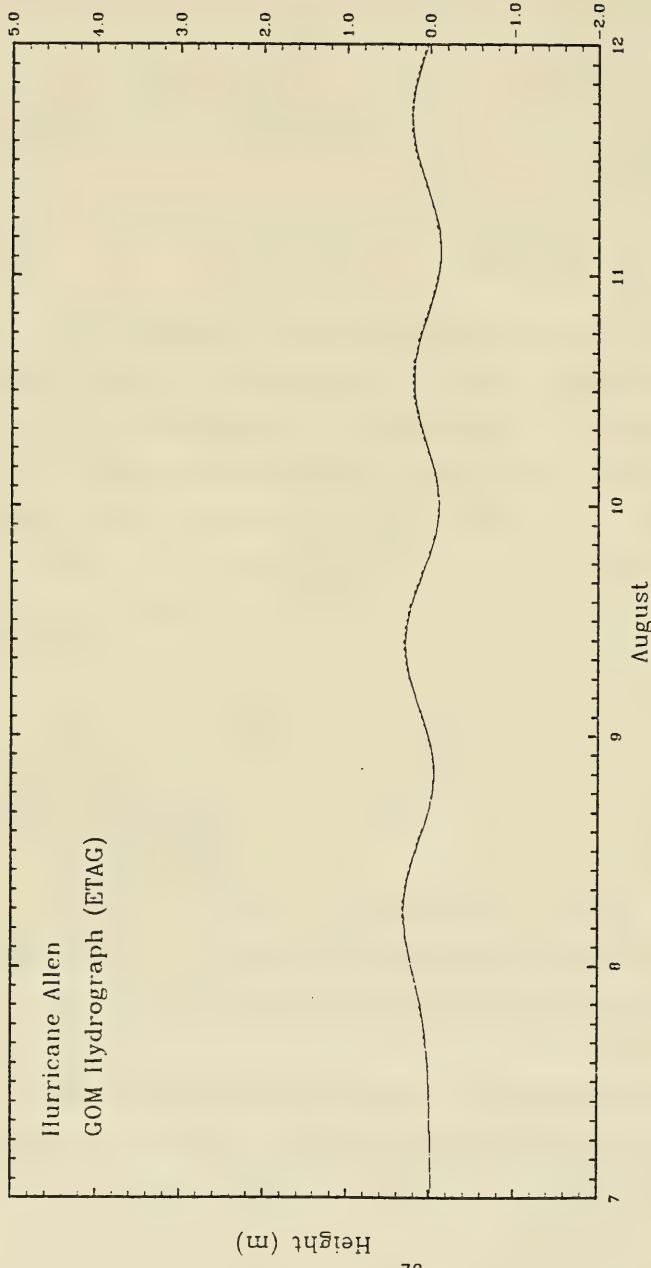
Fig. 33. Time sequences of the average water levels in the Gulf of Mexico, η_G for hurricane Allen. The solid line is computed by averaging water levels from every grid point in the Gulf at each time step. The dashed line is computed from the continuity equation. The datum is mean sea level.

78

Fig. 34. Computed (solid) and observed (dashed) hydrographs at Key West during hurricane Allen 7 – 12 August 1980. The datum is mean sea level.

79
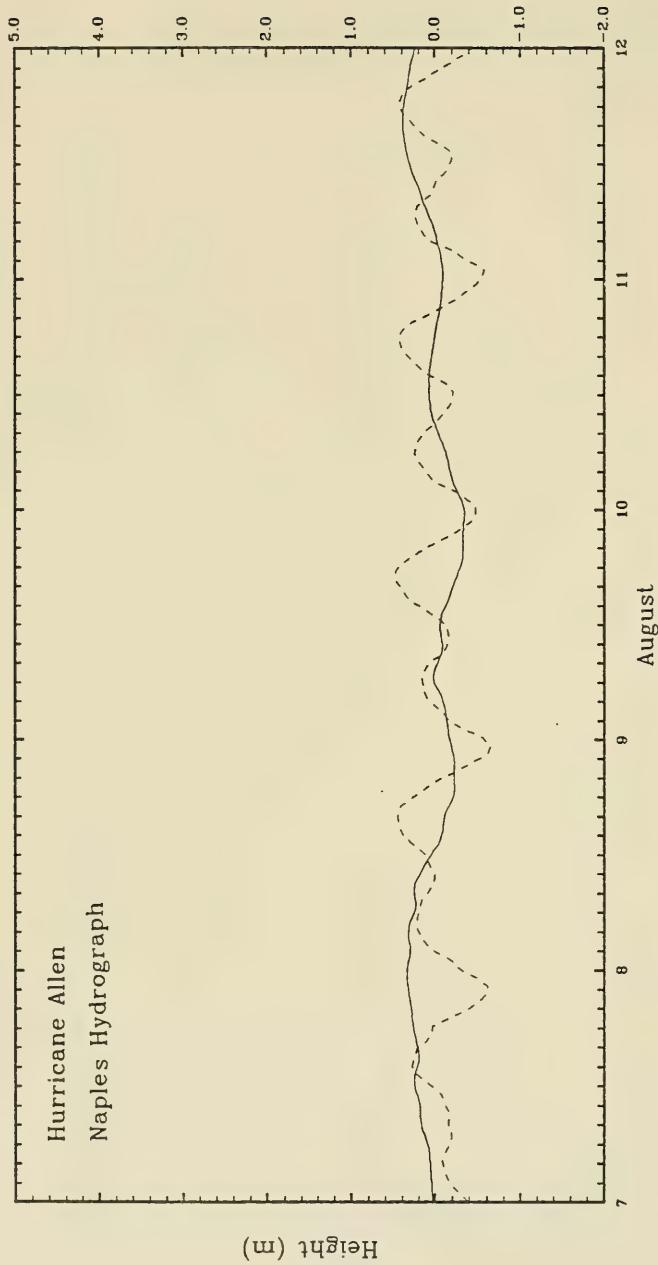
Fig. 35. Computed (solid) and observed (dashed) hydrographs at Naples during hurricane Allen 7 – 12 August 1980. The datum is mean sea level.
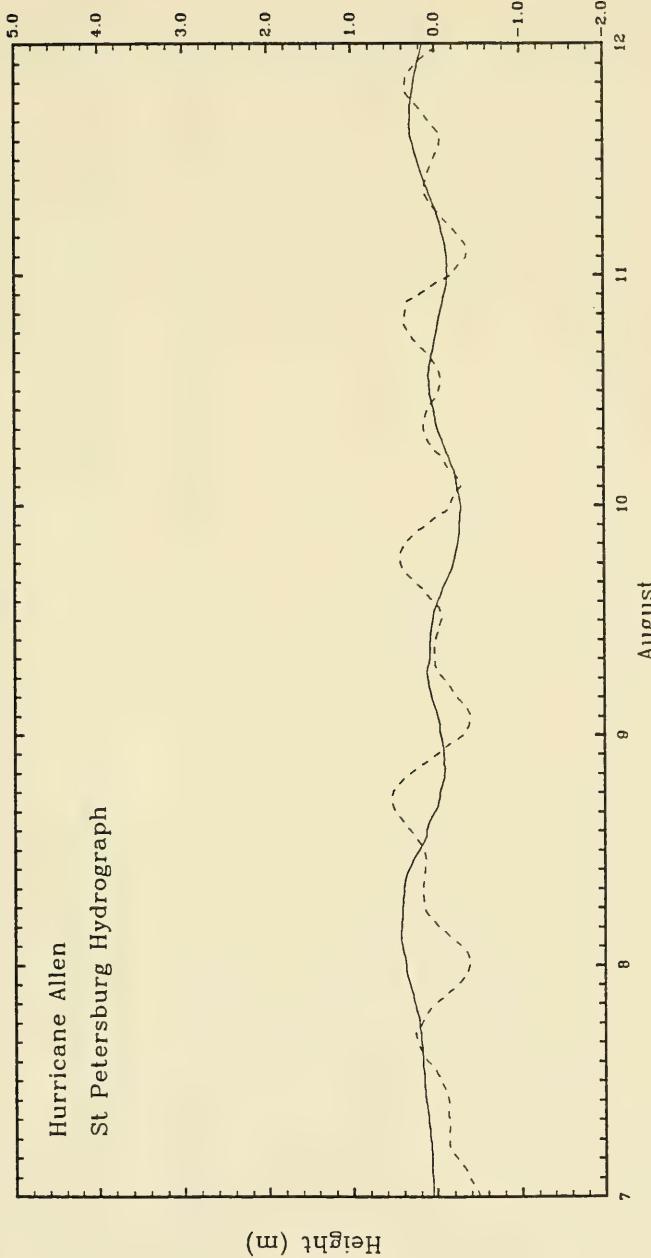
Fig. 36. Computed (solid) and observed (dashed) hydrographs at St. Petersburg during hurricane Allen 7 - 12 August 1980. The datum is mean sea level.

81
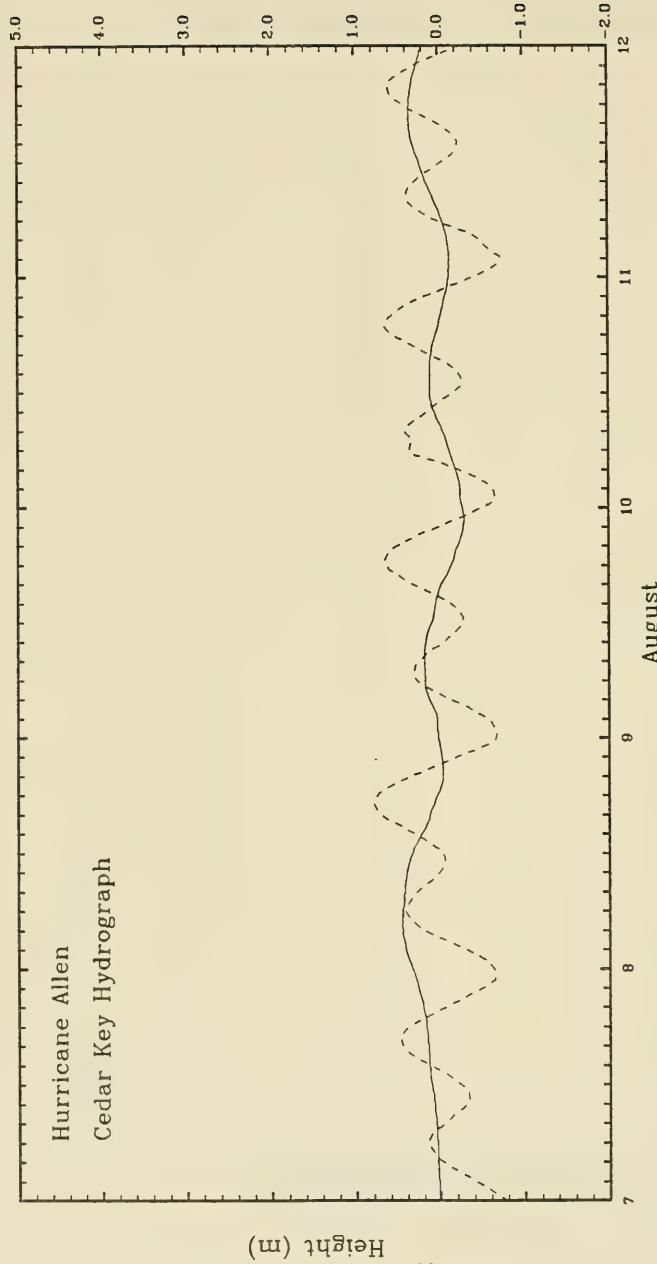
Fig. 37. Computed (solid) and observed (dashed) hydrographs at Cedar Key during hurricane Allen 7 – 12 August 1980. The datum is mean sea level.

82
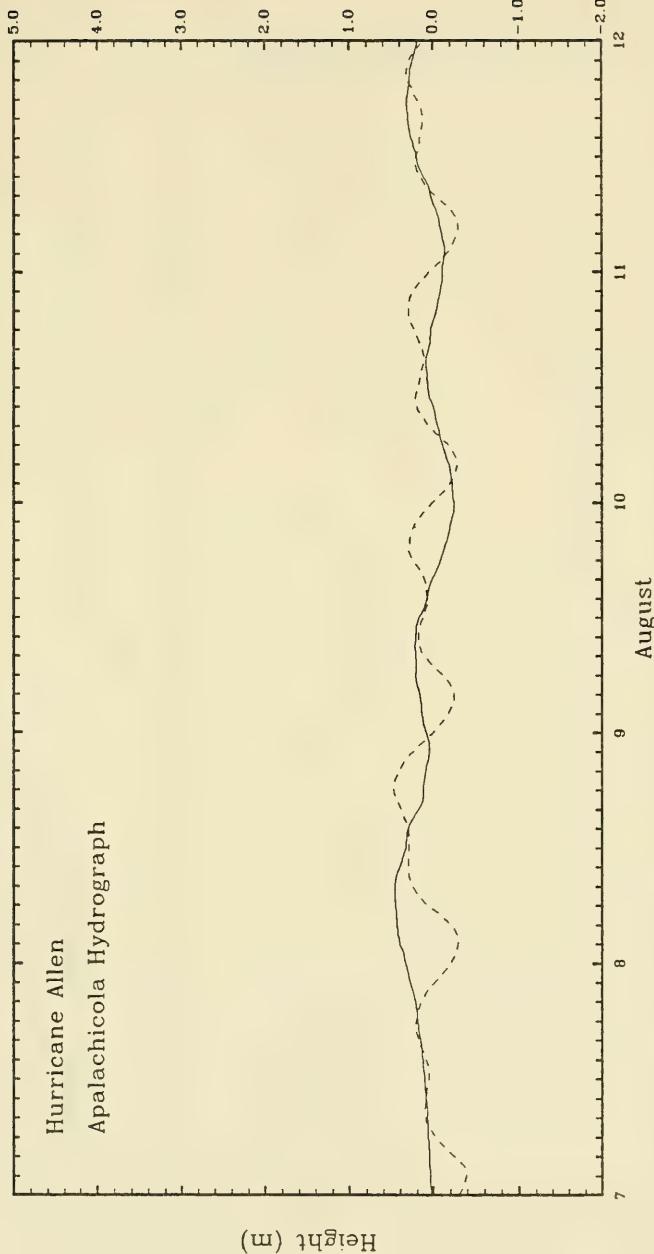
Fig. 38. Computed (solid) and observed (dashed) hydrographs at Apalachicola during hurricane Allen
7 - 12 August 1980. The datum is mean sea level.
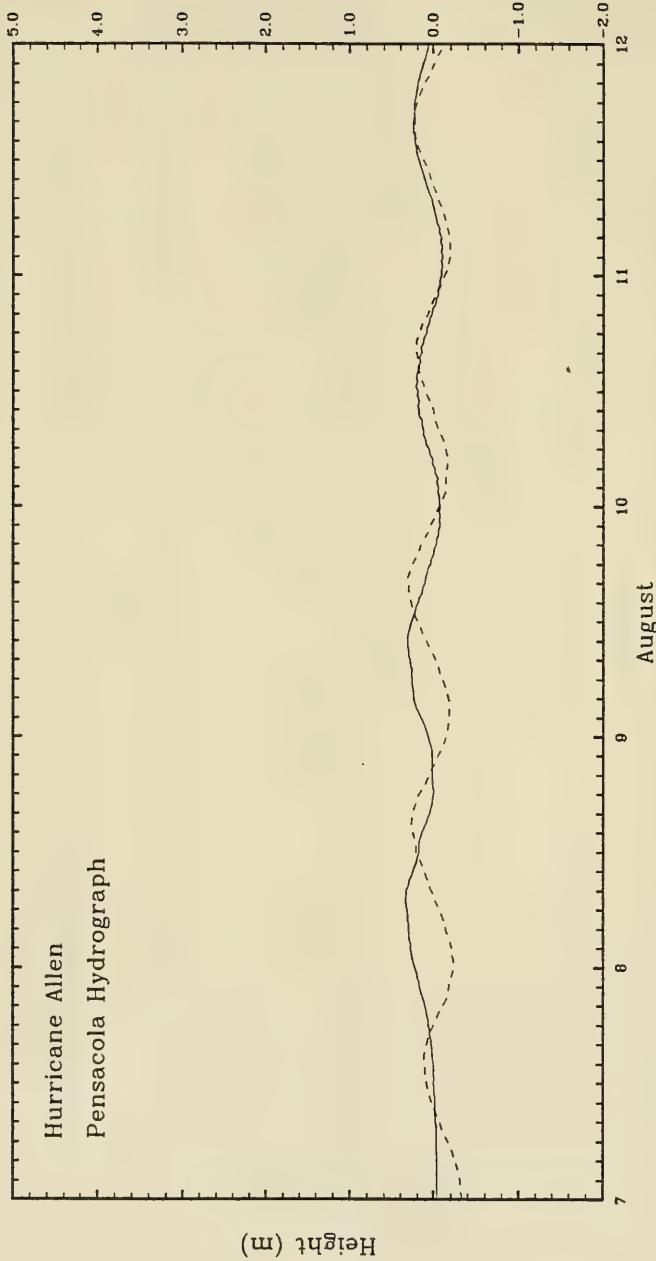
Fig. 39. Computed (solid) and observed (dashed) hydrographs at Pensacola during hurricane Allen 7 – 12 August 1980. The datum is mean sea level.

84
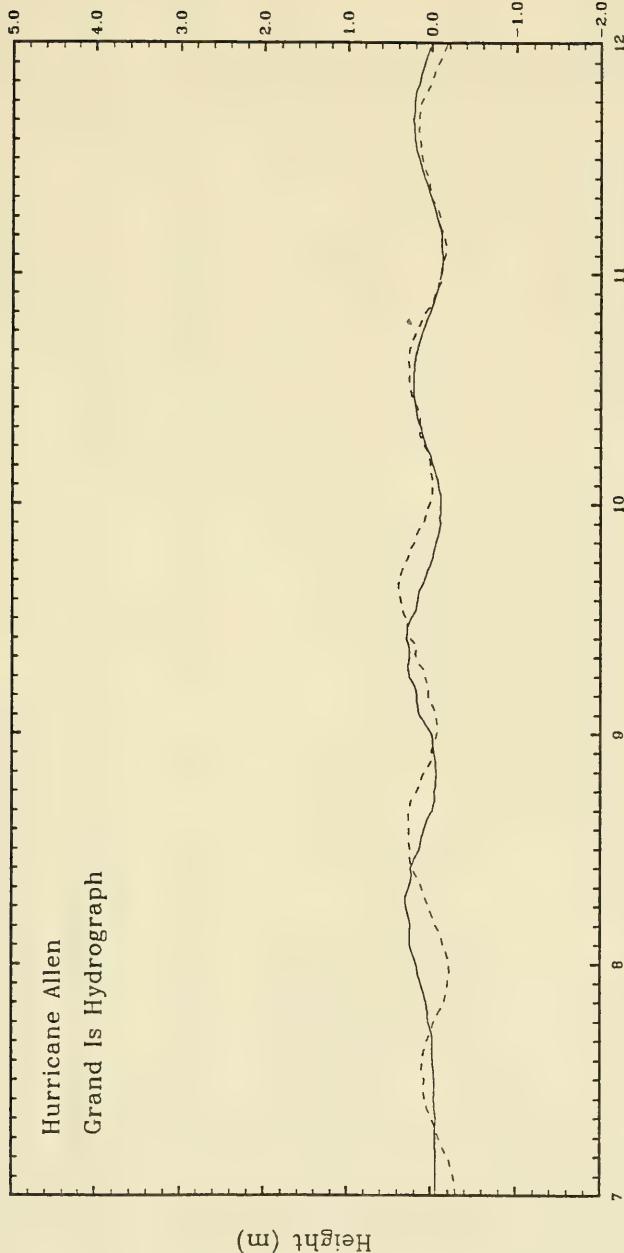
Fig. 40. Computed (solid) and observed (dashed) hydrographs at Grand Isle during hurricane Allen 7 - 12 August 1980. The datum is mean sea level.
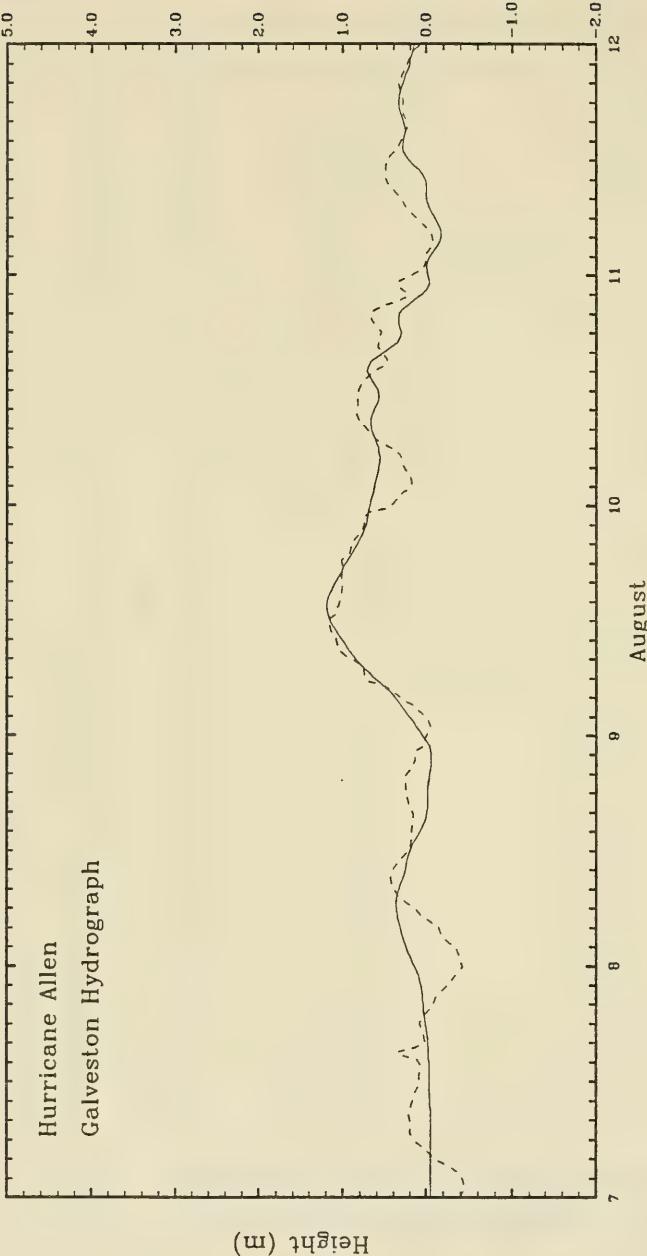
Fig. 41. Computed (solid) and observed (dashed) hydrographs at Galveston during hurricane Allen
7 - 12 August 1980. The datum is mean sea level.

86
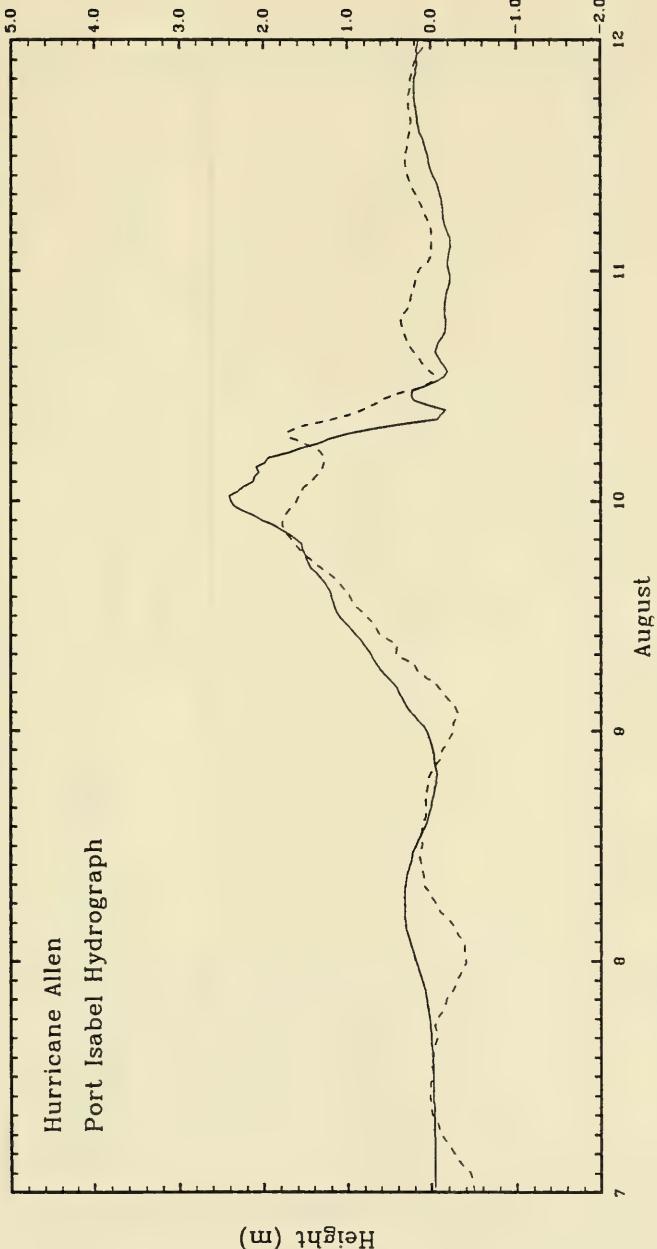
Fig. 42. Computed (solid) and observed (dashed) hydrographs at Port Isabel during hurricane Allen 7 – 12 August 1980. The datum is mean sea level.

87
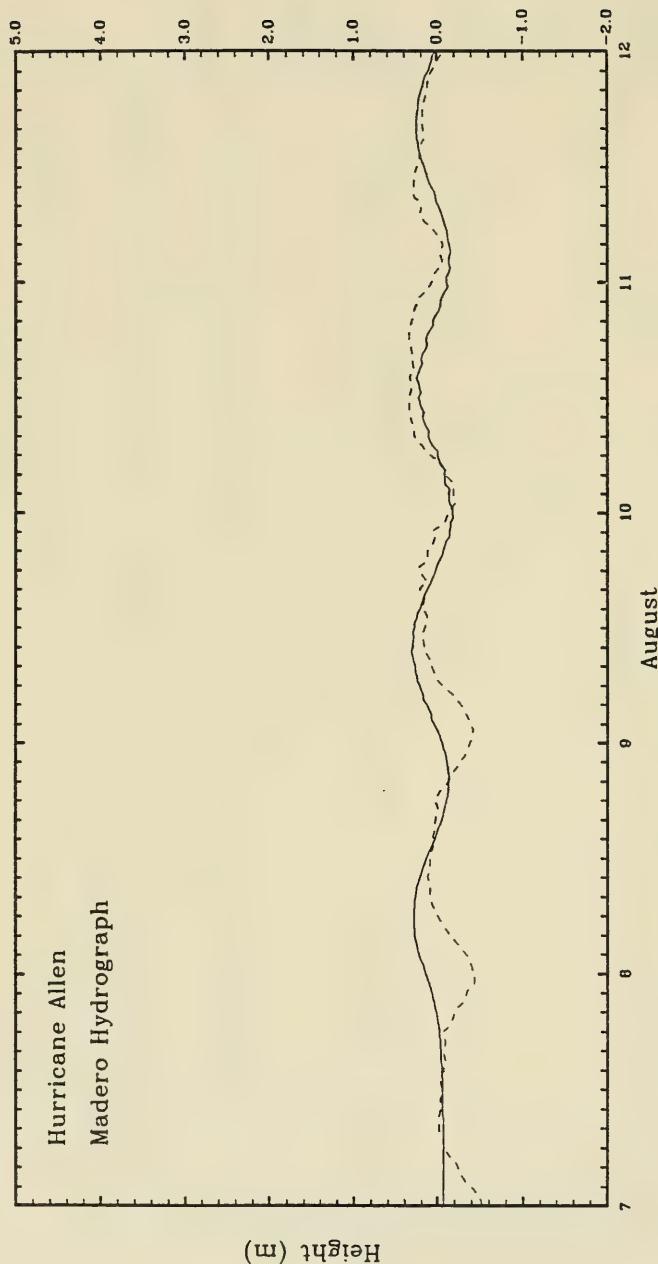
Fig. 43. Computed (solid) and observed (dashed) hydrographs at Madero during hurricane Allen 7 - 12 August 1980. The datum is mean sea level.
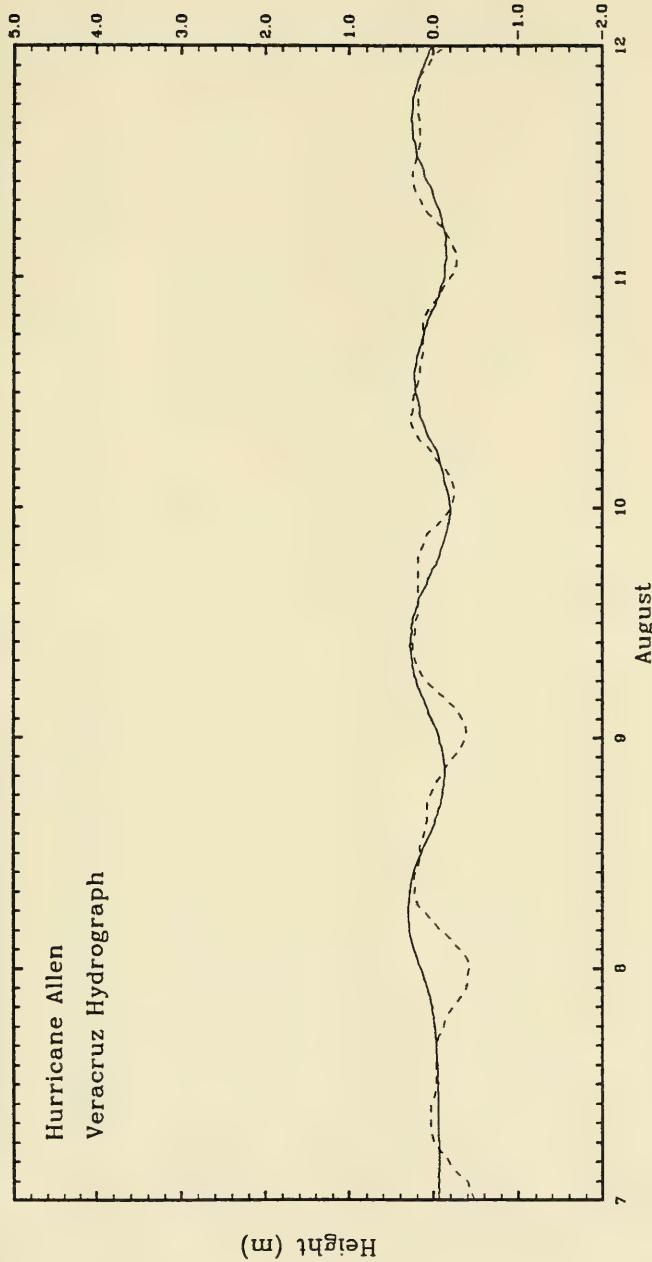
Fig. 44. Computed (solid) and observed (dashed) hydrographs at Veracruz during hurricane Allen 7 - 12 August 1980. The datum is mean sea level.

89
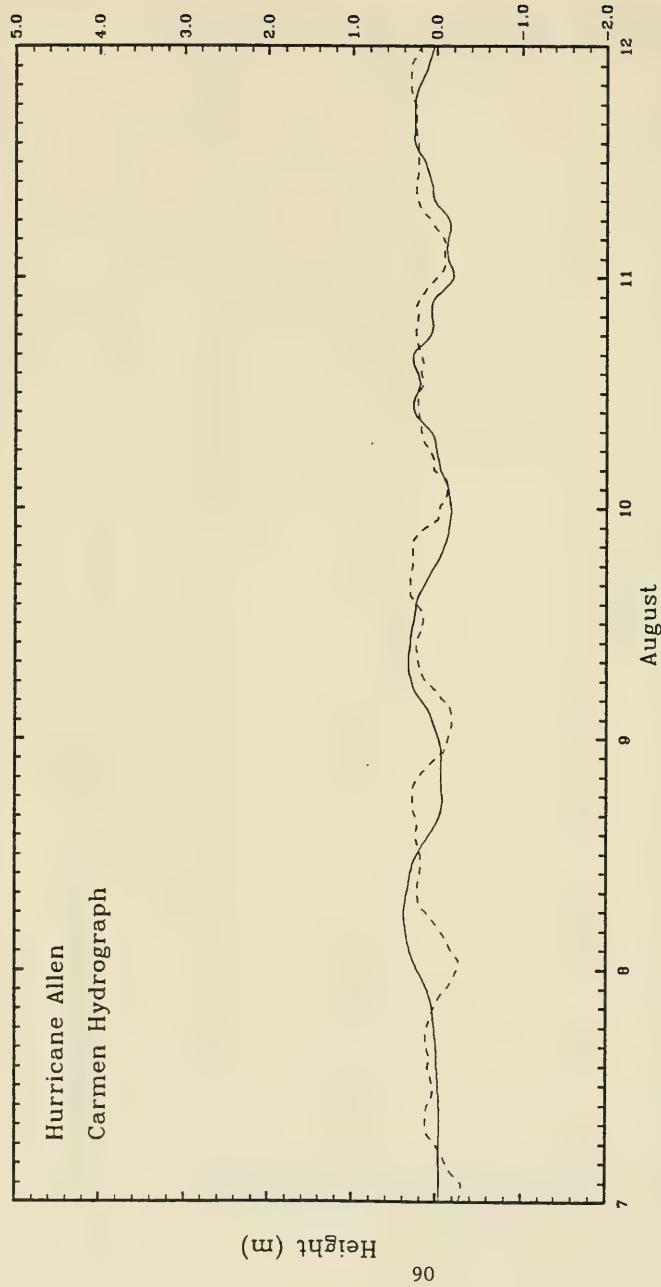
Fig. 45. Computed (solid) and observed (dashed) hydrographs at Carmen during hurricane Allen 7 – 12 August 1980. The datum is mean sea level.
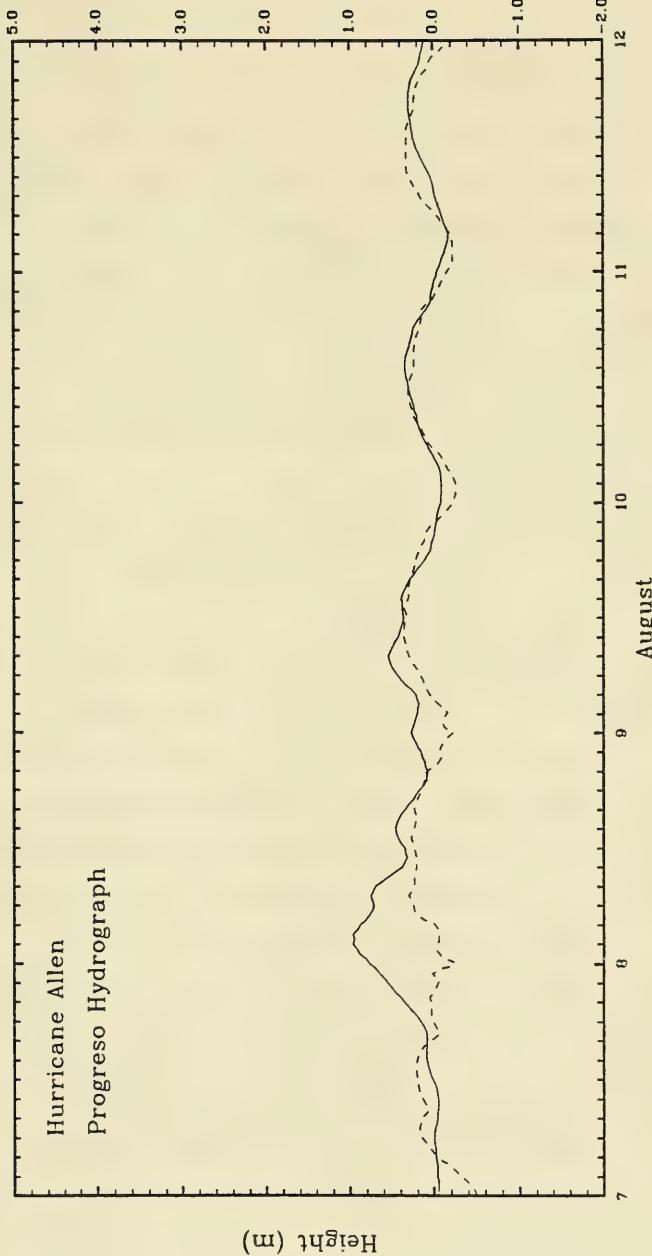
Fig. 46. Computed (solid) and observed (dashed) hydrographs at Progreso during hurricane Allen 7 - 12 August 1980. The datum is mean sea level.

forcing is available for hurricane Allen than for hurricane Carla.

Hydrographs from the Mexican stations (Figs. 44-46, p. 89 - 91) reveal almost no response except for η_G for the entire period considered. The computed water level at Progreso shows a response to the barometric pressure drop during the passage of the center of Allen between 1800 GMT 7 August to 0006 GMT 8 August. However, the observed hydrographs have no indication of this perturbation. This circumstance also occurs in the simulation of hurricane Carla (cf. Fig. 28, p. 70). It is not yet appreciated why the Mexican coast is passive to these two hurricanes.

The slow oscillation found at Key West and St. Petersburg in the Carla simulation is also present. It is noticeable again at all stations from Key West to Appalachicola.

The maximum computed water level occurs at grid point (4,33) which is the location of the sample point for the Port Isabel hydrograph. This simulated peak surge is of the order of one meter higher than the recorded peak. This is to be expected considering the difference in locations of the simulated and actual hydrographs (cf. Fig. 29, p. 72). In addition to reduction of the magnitude of wind speed at the actual tide station by South Padre Island, the volume responses inside the Laguna Madre will be small because of the constricted opening. These factors contribute to a higher computed water level at this station. A slower retreat in the observed hydrograph is due possibly to the trapping of water inside the embayment.

The contours of modal height anomalies and surface currents at 1200 GMT 9 August are shown in Figs. 47-49. The inertio-gravity waves in the baroclinic height anomaly (Fig. 48) seem to be undetectable. Examination of this field at later times indicates that only one-half wavelength of the wake oscillation is seen in Fig. 48. This agrees with the experimental results of Chang and Anthes (1978) showing that the faster the storm moves the longer the wavelength of the oscillation. The approximate half wavelength of 350 km is measured in this hurricane Allen simulation.

The existence of η_G in the simulated hydrographs for Allen prompted a repeat simulation of hurricane Carla with the added code to determine η_G. Figure 50 shows the resulting time sequence of η_G for Carla. The amplitude is smaller than the one associated with hurricane Allen and the averaged period is about 24 h. The η_G signal obtained from the Carla simulation once again shows up simultaneouly in the individual hydrographs at stations around the Gulf.

It is important to note that there is a correlation between the η_G signal and the transport through both Florida and Yucatan Straits. Figures 51 and 52 show the time series of the volume transport through Florida Strait (FS), Yucatan Strait (YS), and the total differential volume transport (unlabelled) as obtained from the hurricane Carla and Allen simulations. The striking feature of the differential transport is the periodicity. The average periods of 24 h and 28 h estimated from Figs. 51 and 52 are exactly the same as the period of their corresponding η_G signals. In both cases, the η_G signal lags the net transport by 90° in phase. The first maximum of

93
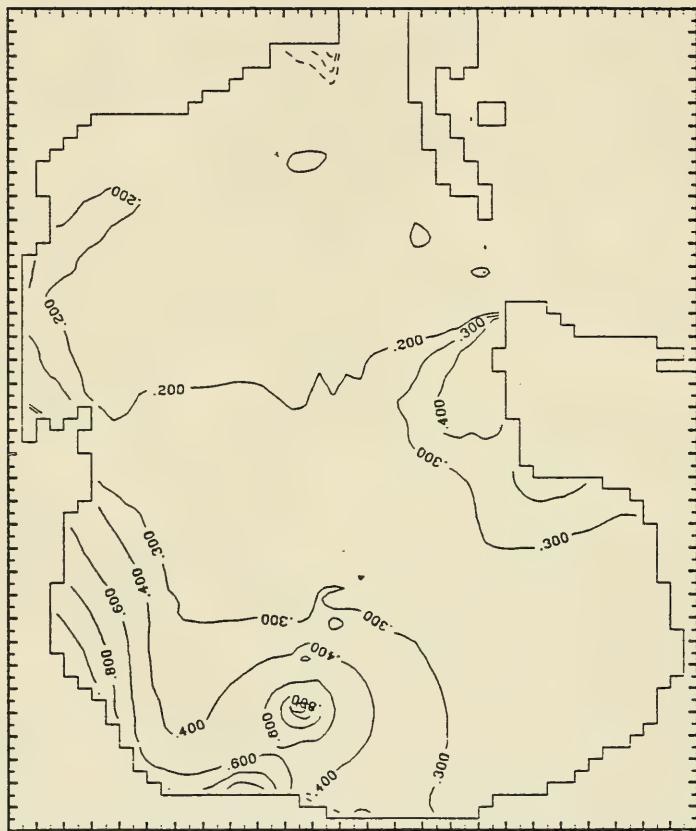
Fig. 47. Computed barotropic height anomaly field (meters) for hurricane Allen at 1200 GMT 9 August 1980.

94
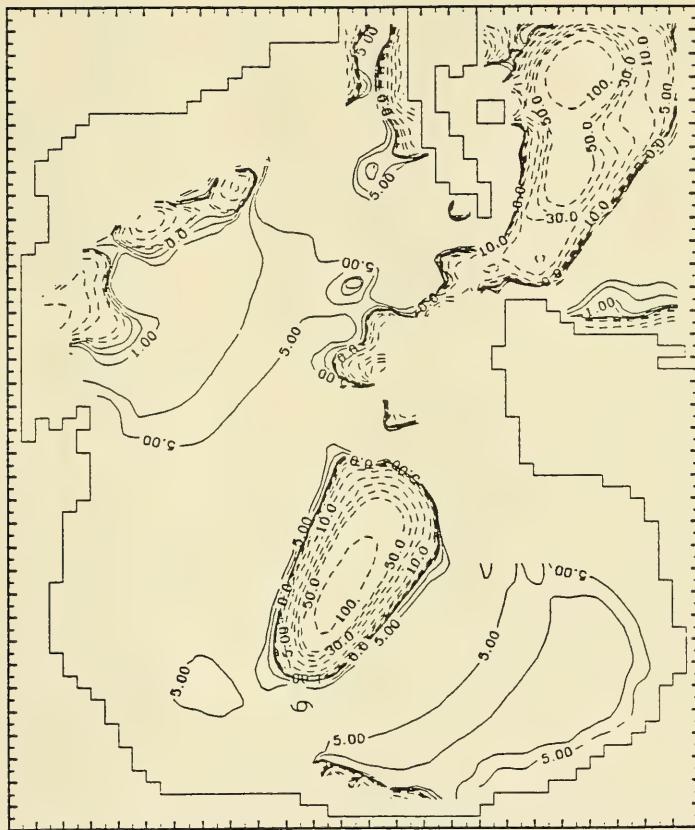
Fig. 48. Computed baroclinic height anomaly field (meters) for hurricane Allen at 1200 GMT 9 August 1980.

95

200.
Maximum Vector
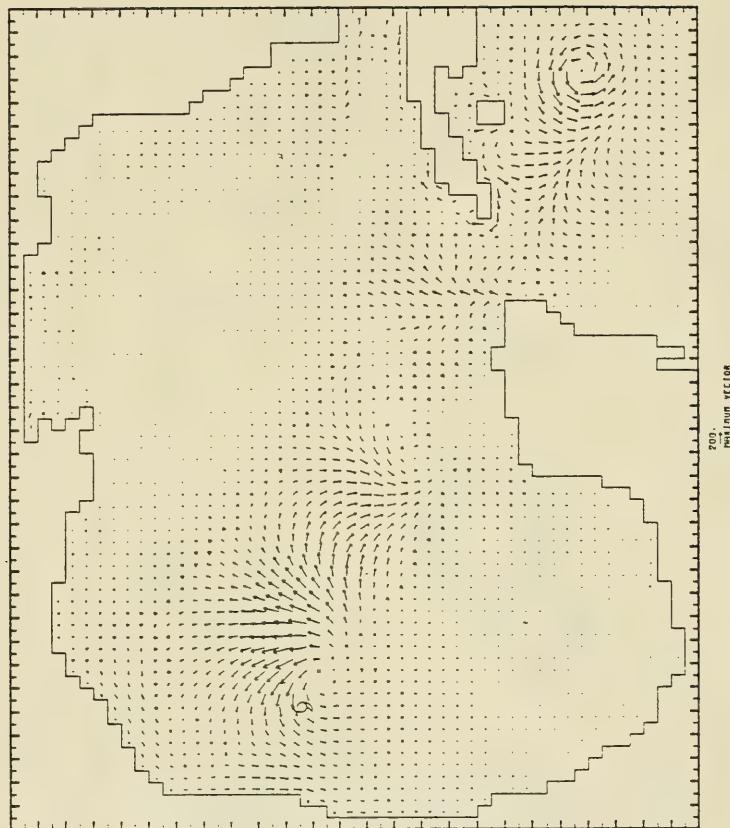
Fig. 49.   Computed surface current field (cm/s) for hurricane Allen at 1200 GMT 9 August 1980.

96
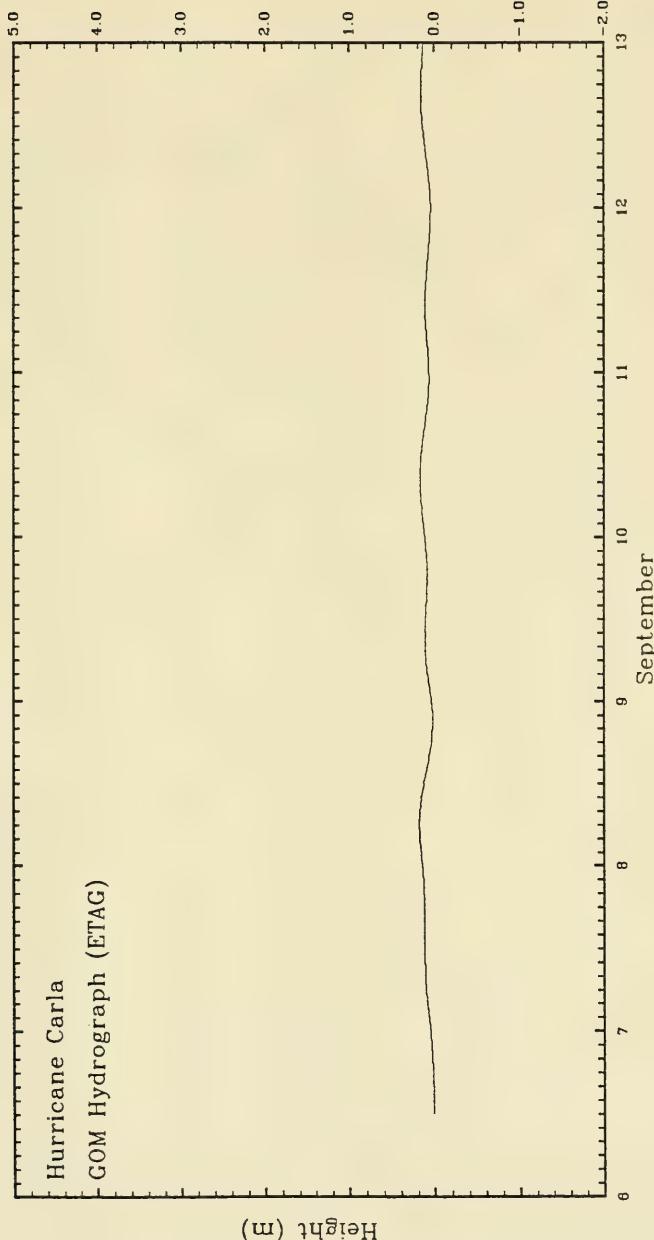
Fig. 50. Time sequence of the averaged water level in the Gulf of Mexcio, η_G, obtained from the simulation of hurricane Carla. The datum is mean sea level.
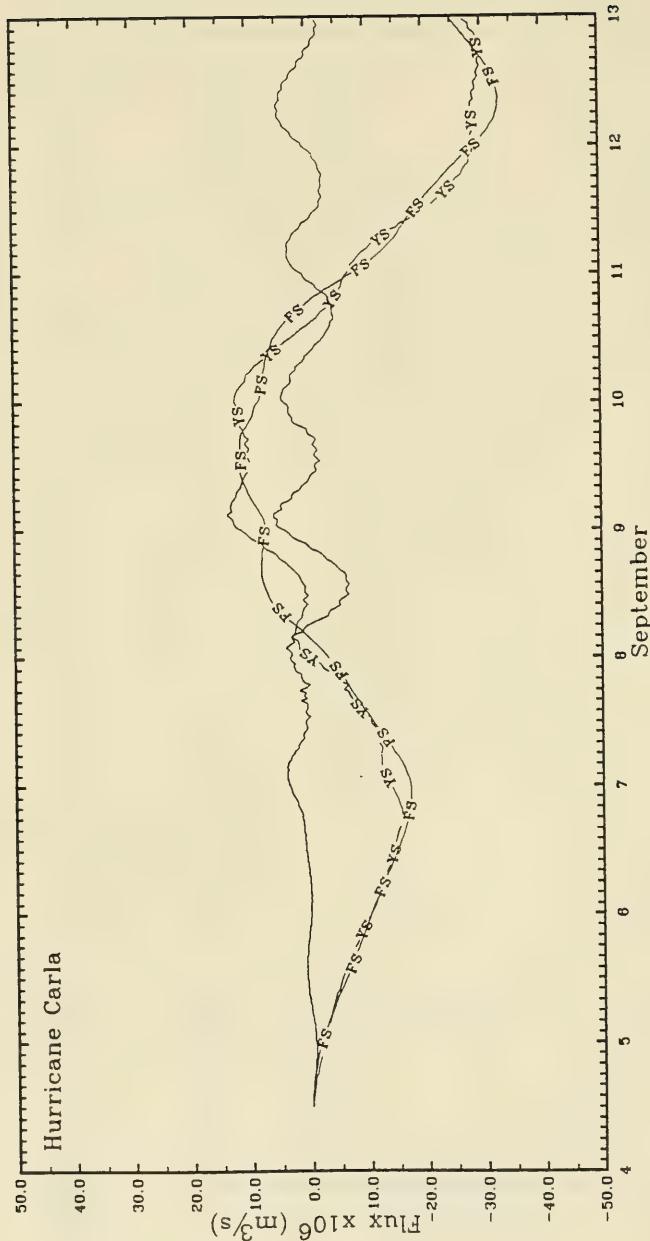
Fig. 51. Time sequences of volume transport through Florida (FS) and Yucatan (YS) Straits obtained from the simulation of hurricane Carla. The unlabelled curve is the net differential volume transport. Note that the same sign for FS and YS correspond to out-of-phase port flux (one into and the other out of the Gulf).
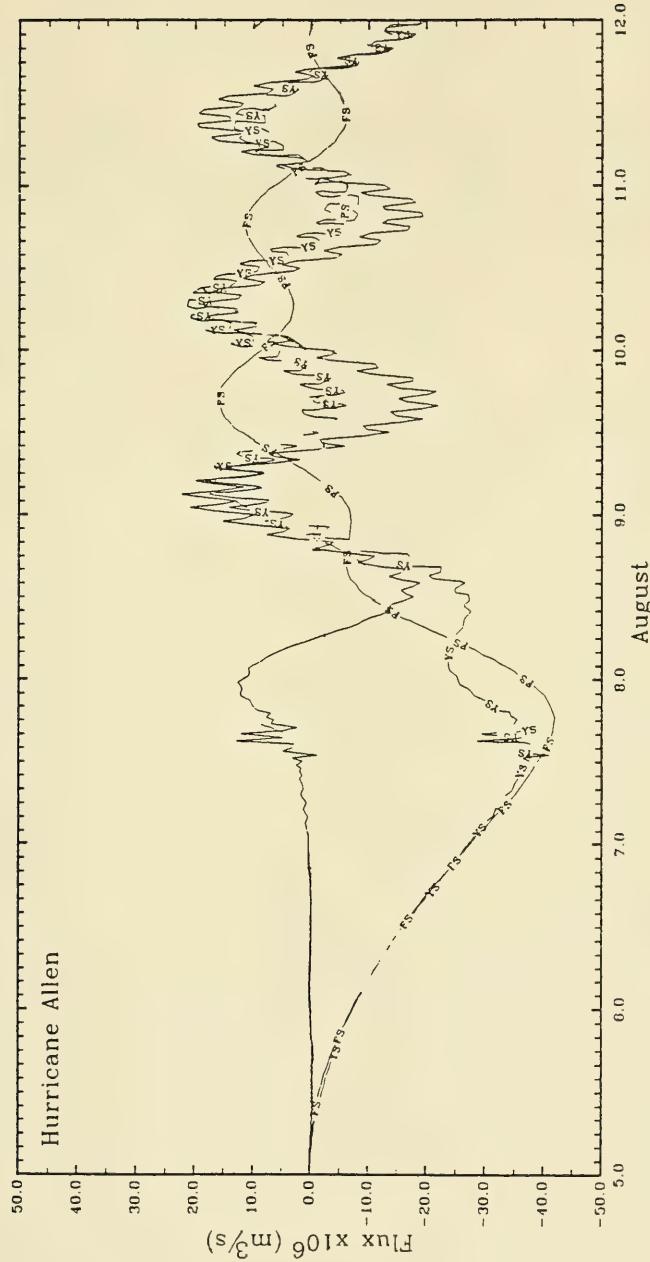
Fig. 52. Time sequences of volume transport through Florida (FS) and Yucatan (YS) Straits obtained from the simulation of hurricane Allen. The unlabelled curve is the net differential volume transport.

the net periodic transport produced by hurricane Carla is approximately 5×10^6 m^3/s as compared to 12.5×10^6 m^3/s generated by hurricane Allen. The η_G signal reaches the first maximum of about 0.1 m for hurricane Carla and 0.35 m for hurricane Allen which are in conformity with their respective net periodic transports. These results are indicative of the generation of η_G by the net differential port forcing (volume transport).

CHAPTER IV

PARAMETRIC STUDY

The purposes of the parametric study were to obtain responses in
the Gulf of Mexico to different forcing from hypothetical storms and
to investigate those cases where the forerunner surges might be
generated.

1. Selection of paths

A total of 5 paths, designated as PATH1 to PATH5, for which the
model storms would traverse the Gulf was selected. The first four
paths originated in the Cayman Sea and entered the Gulf through
Yucatan Strait. Sequentially, the locations where these four paths
crossed land were in the vicinity of Corpus Christi (PATH1), Sabine
Pass (PATH2), Burrwood (PATH3) and Apalachicola (PATH4). The last
path (PATH5) started at 25°N and 81.5°W (overland in Florida) and
made landfall at Corpus Christi. All of these paths were great
circles as shown in Fig. 53. The first and second track (PATH1 and
PATH2) were similar to those of hurricanes Carla and Allen. The
third path (PATH3) was similar to hurricane Camille's (1969) track
while the fourth path resembled the track of hurricane Agnes (1972).
The last track (PATH5) which is rarely observed in nature, was
selected as a special case.
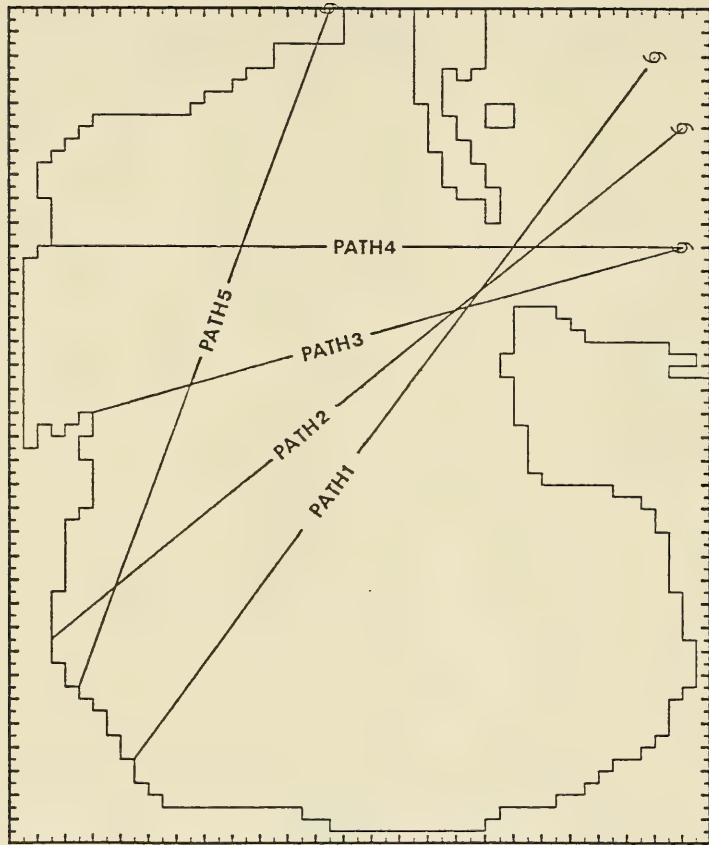
Fig. 53. Selected paths for synthetic storms employed in the parametric study.

2. Hypothetical storms

The hypothetical storms were assumed to be characterized by the NWS23 parametric model with time invariant radius of maximum wind, translational speed and central pressure deficit. Three constant forward speeds of 15, 25 and 35 km/h were adopted. The slowest one was comparable to the average forward speed of hurricane Carla while the fastest speed was approximately the translation speed of hurricane Allen when it was in the Cayman Sea.

Two radii of maximum wind, 30 and 60 km, were selected to account for the scale variation of the atmospheric forcing. The radii were kept constant for the entire simulation period. The range of radius of maximum wind for Gulf Coast hurricanes of record as summarized in Schwerdt et al. (1979) was approximately 10 to 60 km. This range of radii applies to those storms making landfall between Port Isabel and Apalachicola, which covered the landfall locations of the five selected paths. The large radius is at the upper limit and the other is about the average of the observed range. The approximate dimensions of a grid block are 25 km x 27 km and, therefore, sets a lower limit on the radius of maximum wind which can be used. Storms with a radius of maximum wind smaller than the grid size would not be resolved and the associated wind field would be highly distorted.

The last characteristic considered was the pressure drop (ΔP = $P_n - P_c$). It is known, however, that there is a nearly linear relationship between the peak surge and the pressure deficit, other parameters being held fixed (Jelesnianski, 1972). Therefore, a

103

constant value of 80 mb pressure drop was assumed in most of these parametric simulations. Nevertheless, one of the sensitivity tests, which will be discussed later, was designed to verify this relationship.

Table 1 summarizes the possible combinations of these parameters for the five selected paths including their designated hurricane names for further discussions. Runs were made for a representative subset of these model hurricanes (those identified by an * in the last column). This subset allows one to examine responses for different paths for average hurricane parameters, as well as to determine effects of forward speed and effects of scale.

3. Simulation procedure

The start up process for all parametric simulations is the same as in the simulations of hurricanes of record. The model calculations start at 0000 h on day 1 but end at different times depending on the path and forward speed. However, in all cases the computations proceeded to at least 24 h after landfall.

Wind and pressure forcings are again computed at each time step. Parameterizing the pressure drop instead of maximum wind speed (including assuming k=1) simplifies the wind stress computations by eliminating linear interpolations in space (azimuth) and time to obtain k and W_m. Equation (75) is used to compute the wind speed which is then augmented by the forward speed to account for the asymmetry in the wind fields. The only information required to compute the forcing is the position of the storm center which is

Table 1. Characteristics and designated hurricane names for the adopted hypothetical storms for parametric study

Path	Radius of maximum wind (km)	Forward speed (km/h)	Name
1	30	35	HUR2 *
		25	HUR1 *
		15	HUR3 *
	60	35	HUR5 *
		25	HUR4 *
		15	HUR6 *
2	30	35	HUR8
		25	HUR7 *
		15	HUR9
	60	35	HUR11
		25	HUR10
		15	HUR12
3	30	35	HUR14
		25	HUR13*
		15	HUR15
	60	35	HUR17
		25	HUR16
		15	HUR18
4	30	35	HUR20
		25	HUR19*
		15	HUR21
	60	35	HUR23*
		25	HUR22*
		15	HUR24*
5	30	35	HUR26
		25	HUR25*
		15	HUR27
	60	35	HUR29
		25	HUR28
		15	HUR30

given at 6 h intervals. The code added to compute η_G is retained.

4. Results of parametric simulations

The simulated responses of the Gulf to the synthetic storms
listed in Table 1 are presented in this section. Discussions of the
results are separated into three parts. First, general results
common to all simulations are briefly discussed. The simulated
hydrographs obtained from each simulation and other results
pertaining to the development of forerunners are highlighted in the
second part of the discussion. The last part contains results from
related simulations.

a) General results

The inertio – gravity waves in the baroclinic height anomaly
fields are found in all parametric runs. Figures 54 through 57 show
contours of baroclinic height anomalies and the surface current
fields obtained from the HUR2 and HUR3 simulations. Increasing the
forward speed of the storm resulted in increasing the wavelength and
decreasing the width of the wake as seen in Figs. 54 and 56. This is
in agreement with the results of Chang and Anthes (1978) and Geisler
(1970) regarding the wavelength and the width, respectively, of the
storm generated wake.

A dominant long period oscillation is found in the hydrographs
from all stations on the Florida shelf. Estimated periods of this
oscillation are on the order of 4 – 6 days. Marmorino (1982)
analyzed sea level records from Key West to Pensacola recorded during
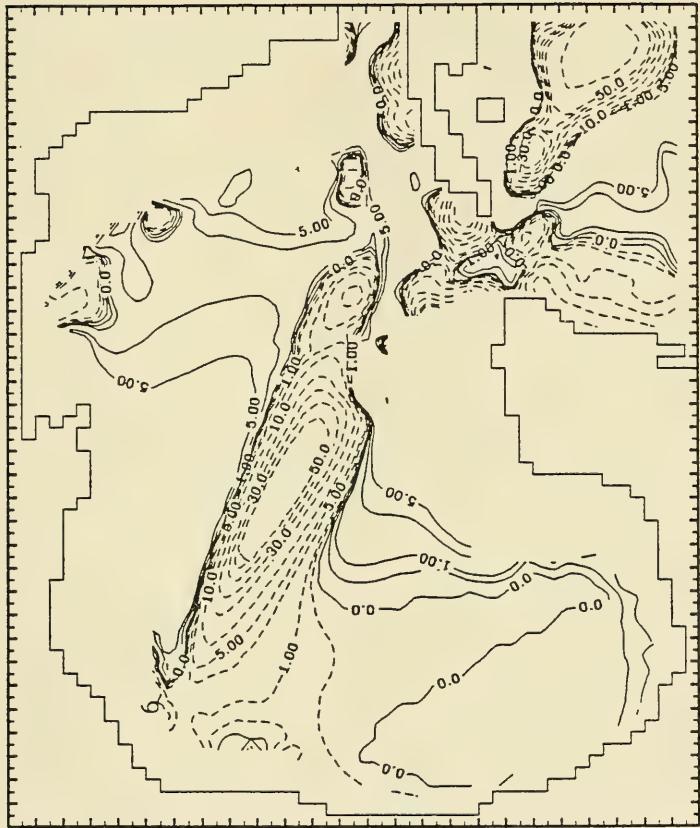
Fig. 54. Computed baroclinic height anomaly (meters) field at 0000 h on day 5 generated by model storm HUR2.

107
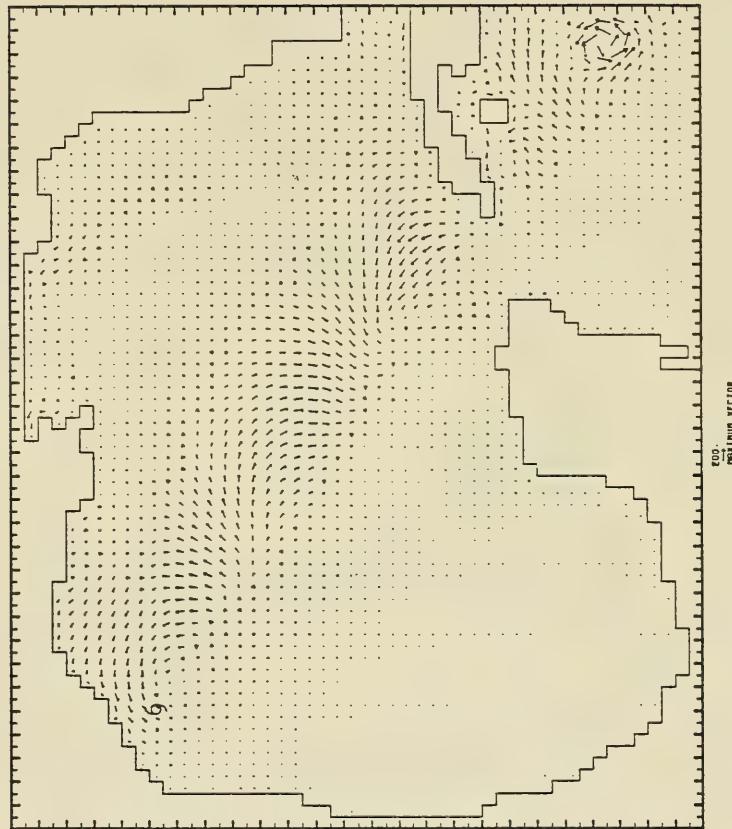
Fig. 55. Computed surface current field (cm/s) at 0000 h on day 5 generated by model storm HUR2.
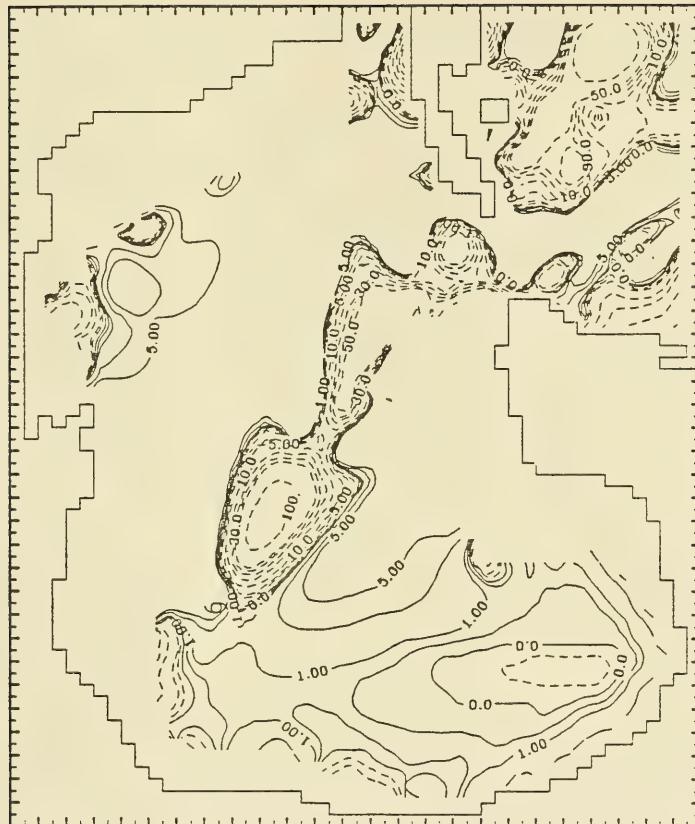
Fig. 56. Computed baroclinic height anomaly field (meters) at 0000 h on day 7 generated by model storm HUR3.
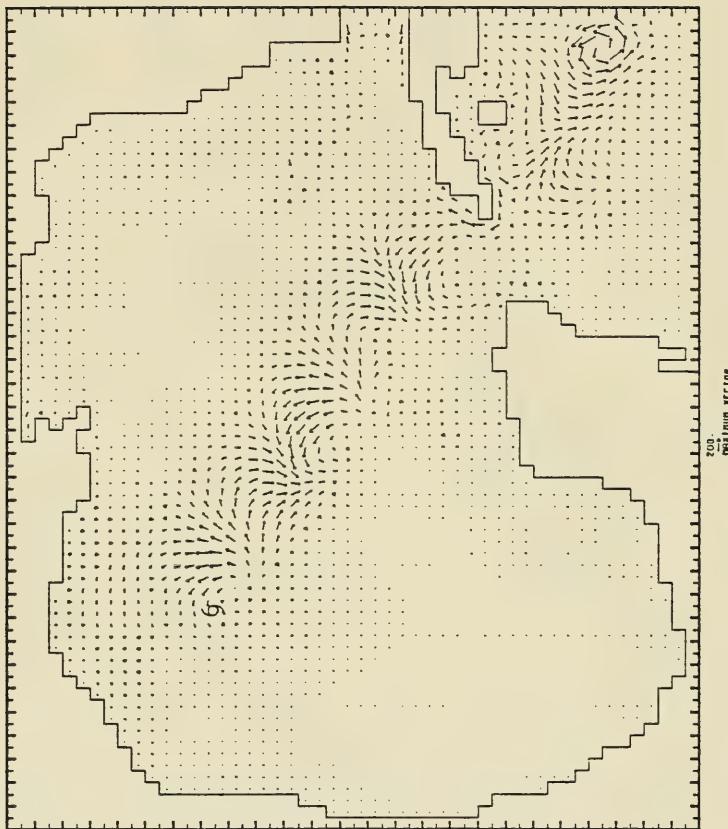
Fig. 57. Computed surface current field (cm/s) at 0000 h on day 7 generated by model storm HUR3.

January - April 1978. Dominant signals were found in the 6 day band and 3 day band. However, the Gulf-wide signal, η_G, can also be observed in the simulated hydrographs from stations on the northern part of the shelf. Figures 58 and 59 show hydrographs from Apalachicola and Cedar Key obtained from the HUR1 simulation. It is obvious from these two figures that other modes of response exist on the Florida shelf.

b) Simulated hydrographs

The following discussions are ordered according to the selected paths starting from PATH1 through PATH5. Within each path, results obtained from the storms of small radius are presented first followed by that of the large radius storms.

The time sequence of the computed water levels at Galveston obtained from the simulation of HUR1 is shown in Fig. 60. The initial rise of water level which reaches a maximum of 0.22 m at approximately 1300 h on day 4 is well-defined. Resurgence after the peak surge with an oscillation period of about 6 h is also noticeable.

The initial peak of water level in the Galveston hydrograph is in phase with the first maximum of the η_G signal as shown in Fig. 61. The first extreme of η_G, which is also the maximum peak, occurs approximately 24 h after the storm entered Yucatan Strait. The average period of this signal is 30 h. This mode is not only present in the hydrographs from all stations but also accounts for almost all of the response in the southwest sector of the Gulf as shown in Figs.

111
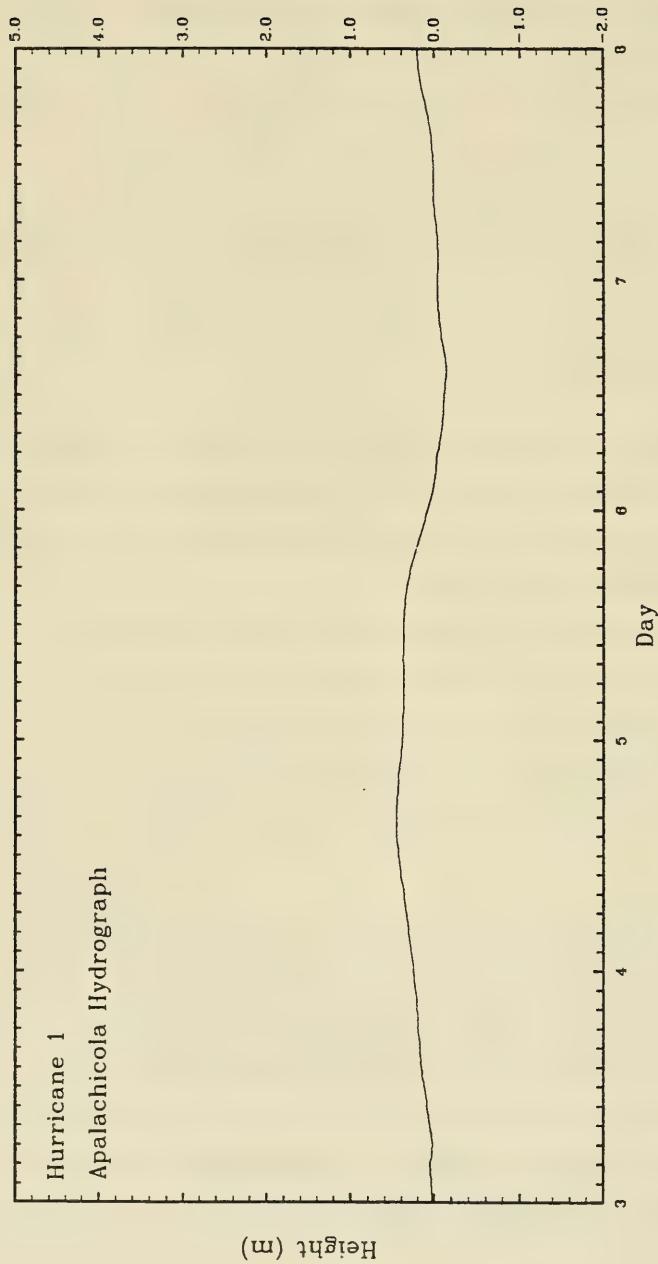
Fig. 58. Time sequence of water levels at Apalachicola obtained from the simulation of HUR1.

112
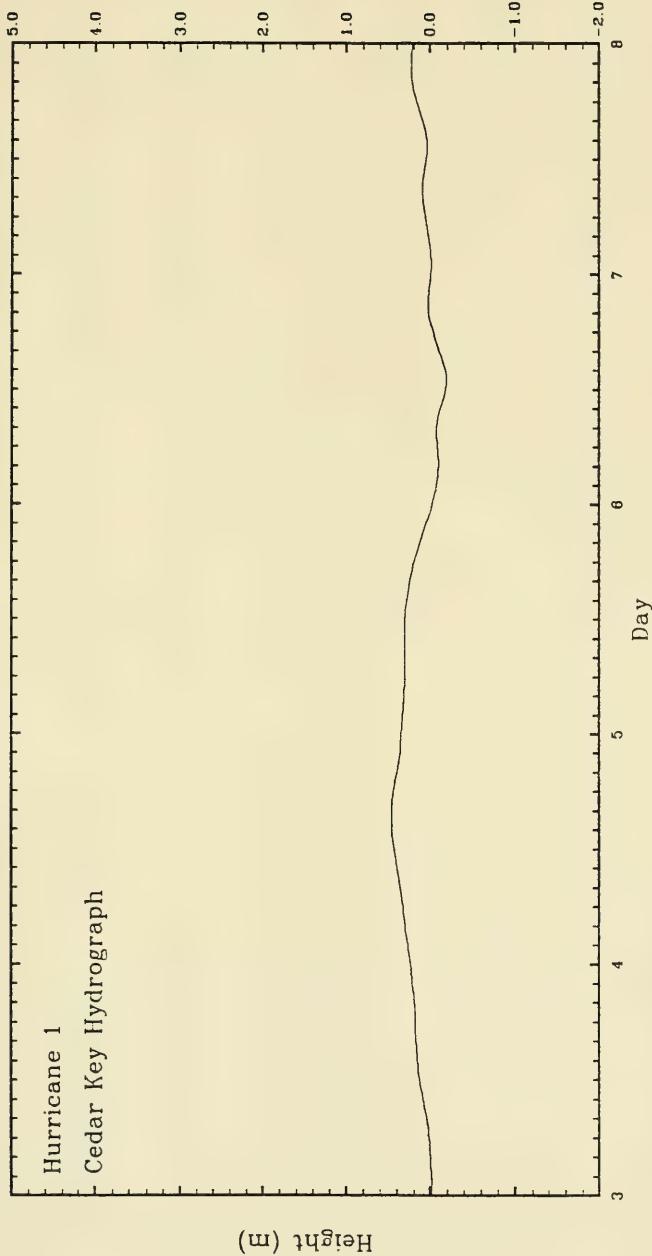
Fig. 59. Time sequence of water levels at Cedar Key obtained from the simulation of HUR1.

113
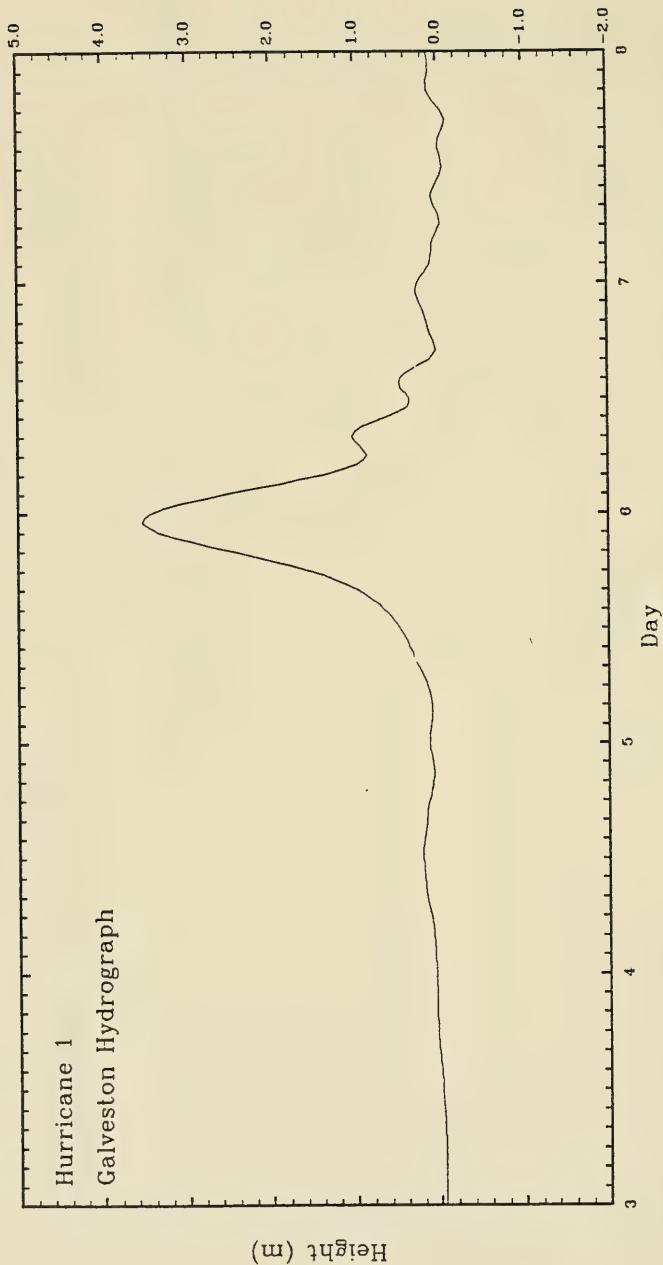
Fig. 60. Time sequence of water levels at Galveston obtained from the simulation of HUR1. The datum is mean sea level.
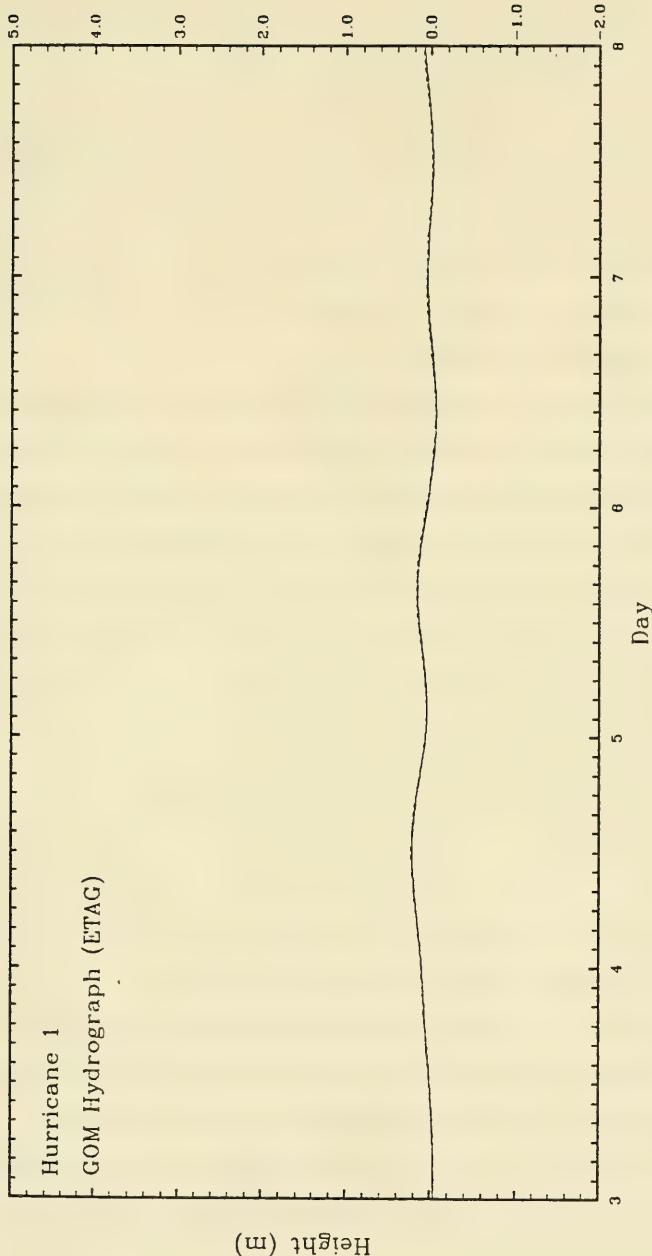
Fig. 61. Time sequences of the average water levels in the Gulf of Mexico, η_G, obtained from the simulation of HUR1. The solid line is computed by averaging water levels from every grid point in the Gulf at each time step. The dashed line is computed from the continuity equation. The datum is mean sea level.

115

62 and 63. The dashed lines represent η_G and the solid lines are the simulated water levels from the indicated station.

The maximum surges generated by HUR2 and HUR3 imply a direct relationship between peak surge at the open coast and forward speed of the storm. Jelesnianski (1972) proposed a correction factor for the effect of storm vector motion (track direction and forward speed at landfall) which is larger for a faster moving storm provided that the landfall angles are the same.

Figures 64 and 65 show the simulated hydrographs at Galveston from the HUR2 and HUR3 simulations, respectively. The initial rise of water level before the peak surges are present in both runs which are concurrent with the first maximum of their corresponding η_G signals. The maximum peaks and periods of η_G as determined from Figs. 66 and 67 are 0.22 m, 28 h and 0.21 m 30 h, respectively. The time lag, δ_G, is approximately 17 h for the faster storm (HUR2) and about 24 h for the slower storm (HUR3).

The maximum surges produced by storms of large R_{max} (HUR4,HUR5,HUR6) are on the order of 2 m larger than those corresponding to the small storm (HUR1,HUR2,HUR3) simulations. Except for a larger percentage of increase in the peak surge at the open coast, the results are in qualitative agreement with Jelesnianski (1972) in which a very simple bathymetry was employed.

The hydrograph at Galveston from the HUR4 simulation is shown in Fig. 68. The time of the peak surge and the time at which the initial rise of water level reaches the maximum are exactly the same as in the HUR1 simulation. The resurgence oscillation is concealed

116
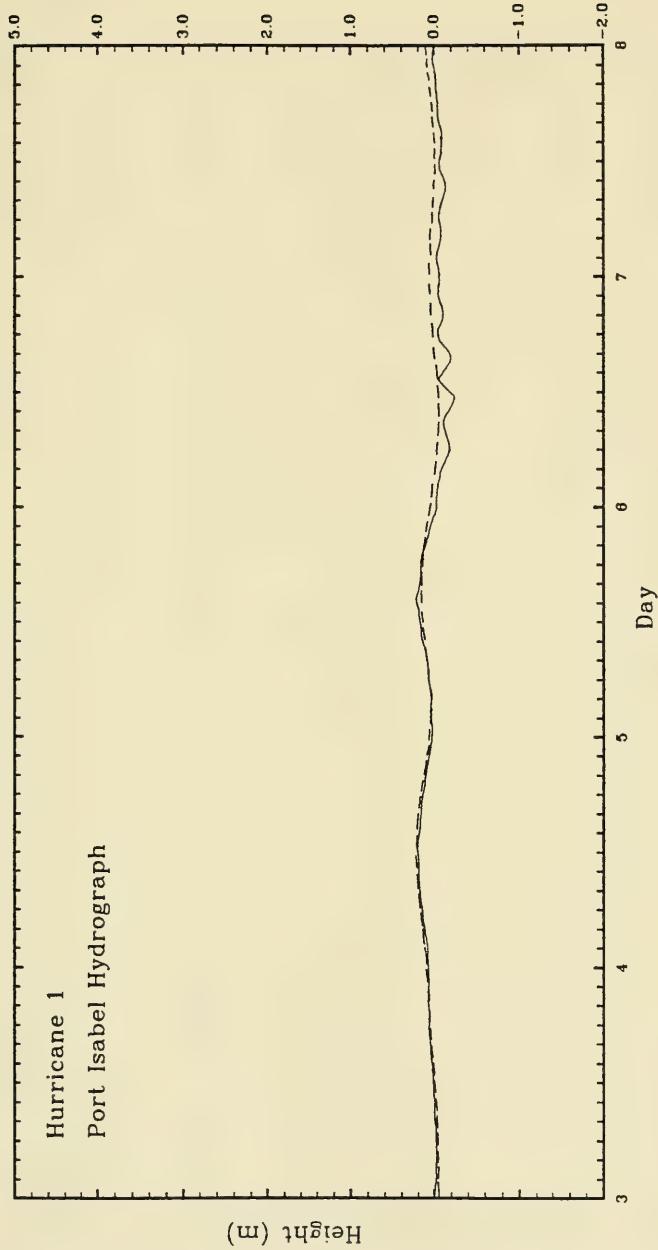
Fig. 62. Time sequences of water levels at Port Isabel (solid) and η_G (dashed) obtained from the simulation of HUR1. The datum is mean sea level.

117
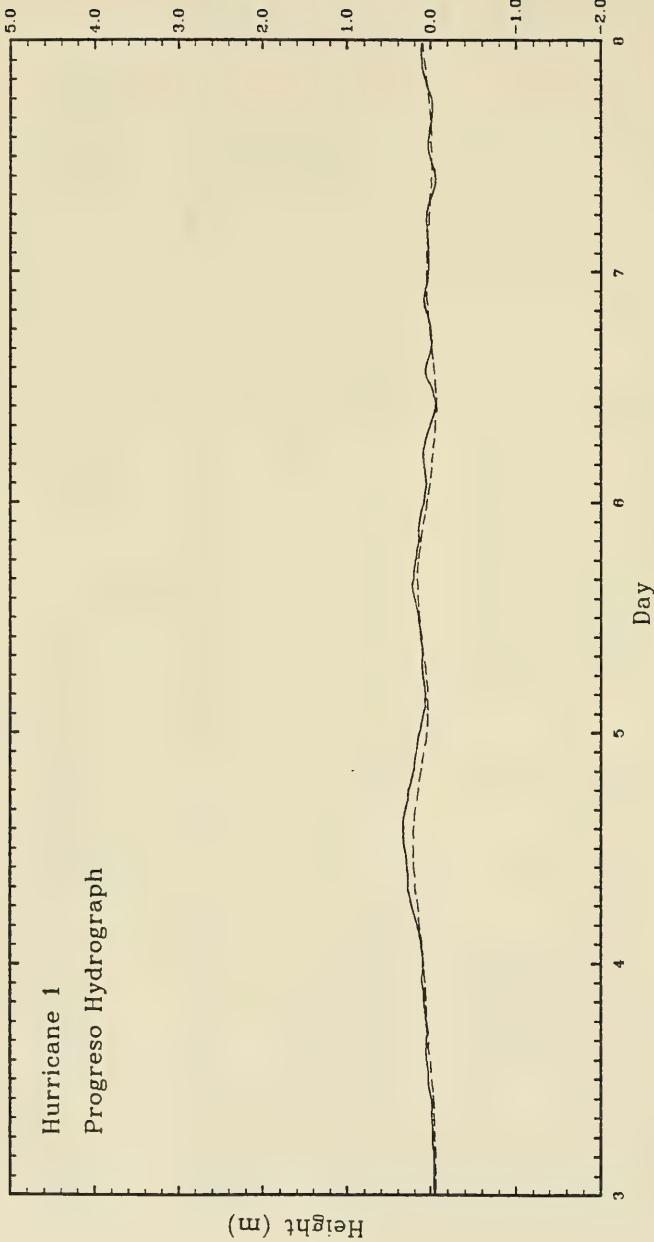
Fig. 63. Time sequences of water levels at Progreso (solid) and η_G (dashed) obtained from the simulation of HUR1. The datum is mean sea level.
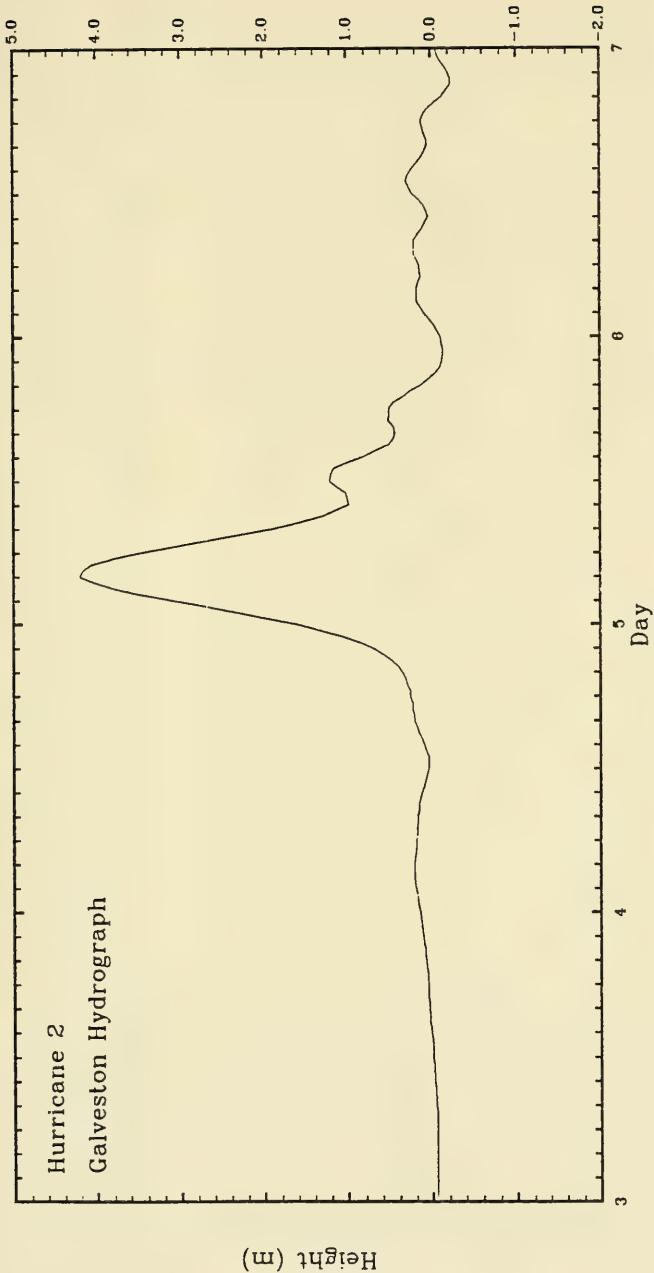
Fig. 64. Time sequence of water levels at Galveston obtained from the simulation of HUR2. The datum is mean sea level.

119
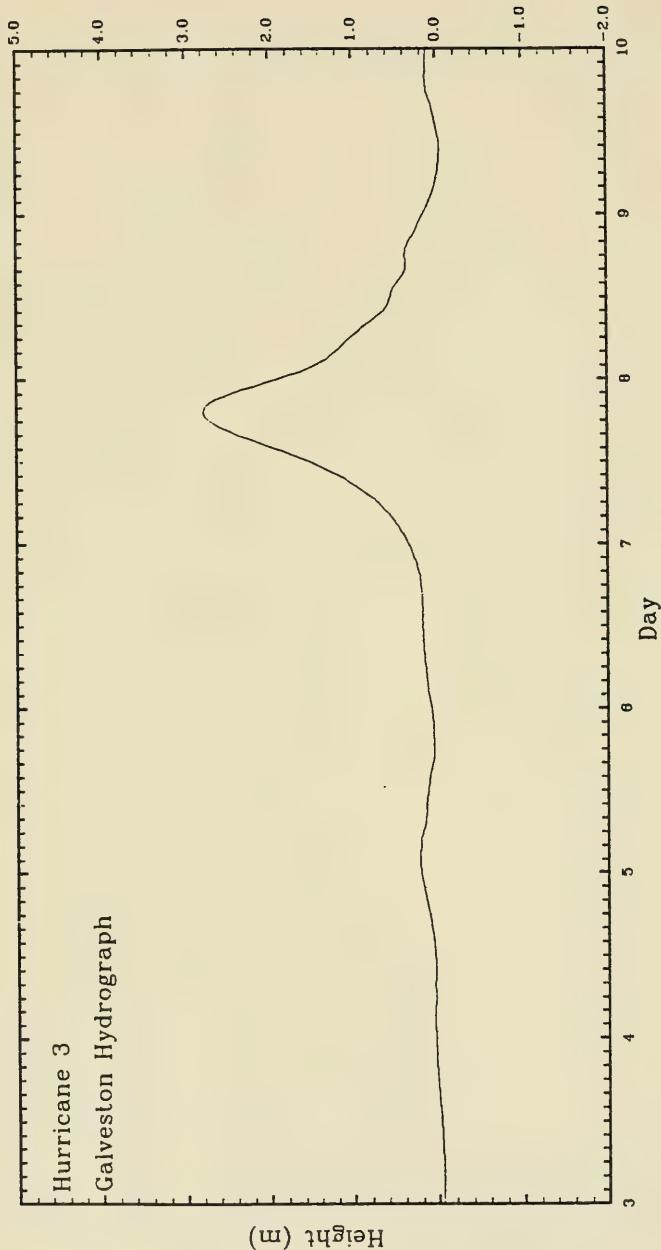
Fig. 65. Time sequence of water levels at Galveston obtained from the simulation of HUR3. The datum is mean sea level.
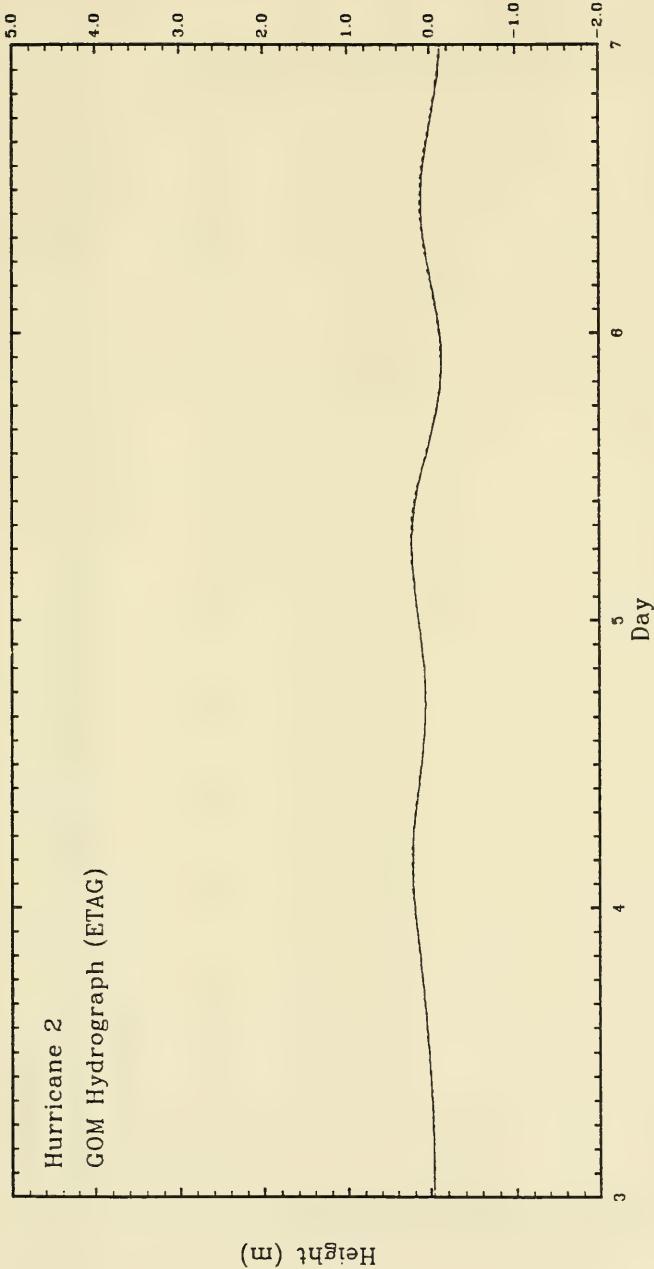
Fig. 66. Time sequences of the average water levels in the Gulf of Mexico, η_G, obtained from the simulation of HUR2. The solid line is computed by averaging water levels from every grid point in the Gulf at each time step. The dashed line is computed from the continuity equation. The datum is mean sea level.
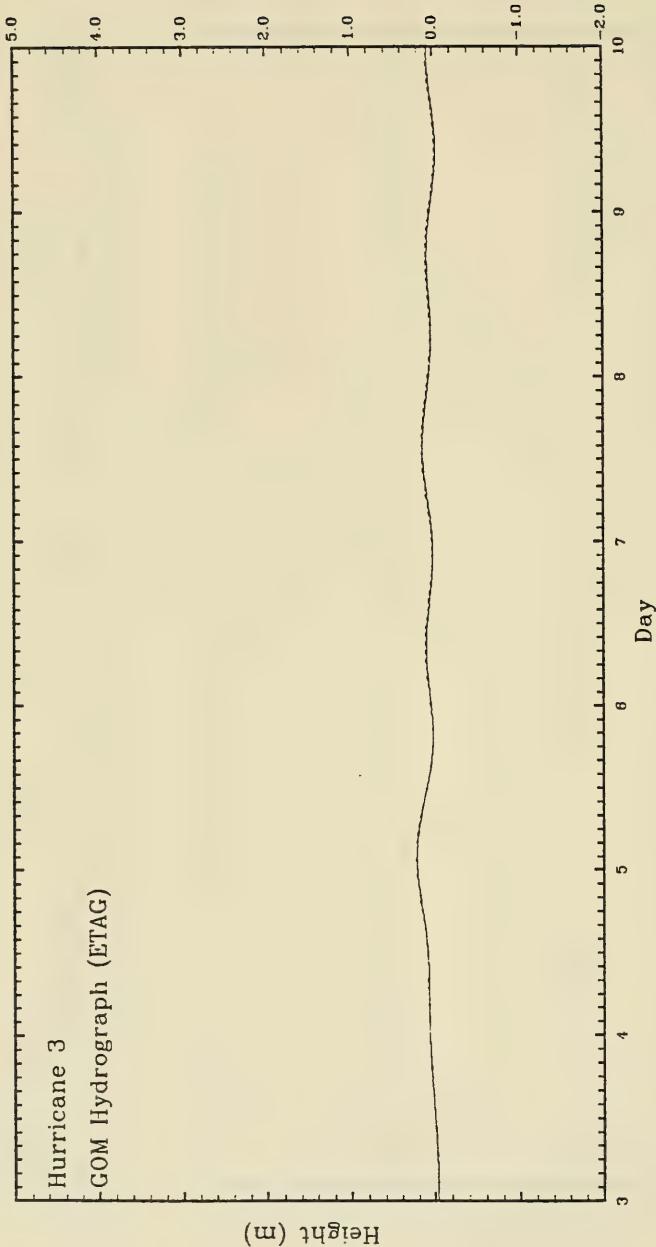
Fig. 67. Time sequences of the average water levels in the Gulf of Mexico, η_G, obtained from the simulation of HUR3. The solid line is computed by averaging water levels from every grid point in the Gulf at each time step. The dashed line is computed from the continuity equation. The datum is mean sea level.

122
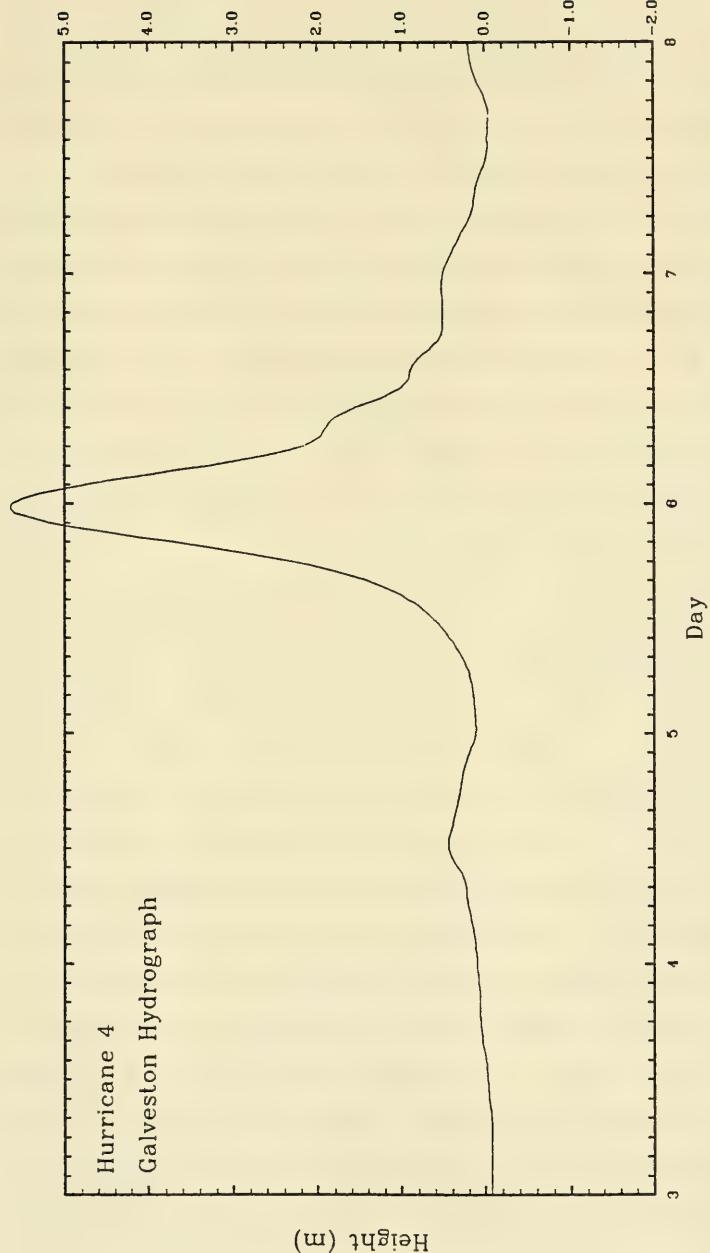
Fig. 68. Time sequence of water levels at Galveston obtained from the simulation of HUR4. The datum is mean sea level.

123

by a high peak surge but still observable. Figure 69 shows the time sequence of the Gulf-wide oscillation, η_G, generated by HUR4. The average period and δ_G are 30 h and 24 h, respectively. The maximum peak is 0.42 m, about a factor of 2 larger than in the HUR1 simulation. It is interesting to note that the largest difference in the extremes of η_G from HUR1 and HUR4 occur at their first maximum. During later stages the differences reduce to a few centimeters. The presence of η_G in the simulated hydrographs from the other stations is preserved. However, this oscillation is no longer coincident with the water levels at the individual stations as in the previous cases. Figures 70 and 71 clearly demonstrate the departure between the two curves at Port Isabel and Progreso.

A peak surge of 6.5 m at the coast is generated by a fast moving storm of large R_{max}(HUR5). The slow moving storm of the same size (HUR6) however, produces a smaller 4.71 m peak surge. Increasing the maximum surge at the coast with increasing forward speed is the same as that obtained from simulations of small storms as discussed above. Figures 72 and 73 display the computed hydrographs at Galveston obtained from the HUR5 and HUR6 simulations, respectively. Both hydrographs have an initial rise of water level prior to the peak surge that again matches the first peak of their corresponding η_G series. The time sequence of the η_G signal for HUR5 and HUR6 are shown in Figs. 74 and 75. The maximum peaks of η_G (0.4 m for HUR5 and 0.38 m for HUR6) vary slightly with the forward speed but both are approximately twice as large compared with those produced by the small storms with the same forward speed, i.e., HUR2 and HUR3,
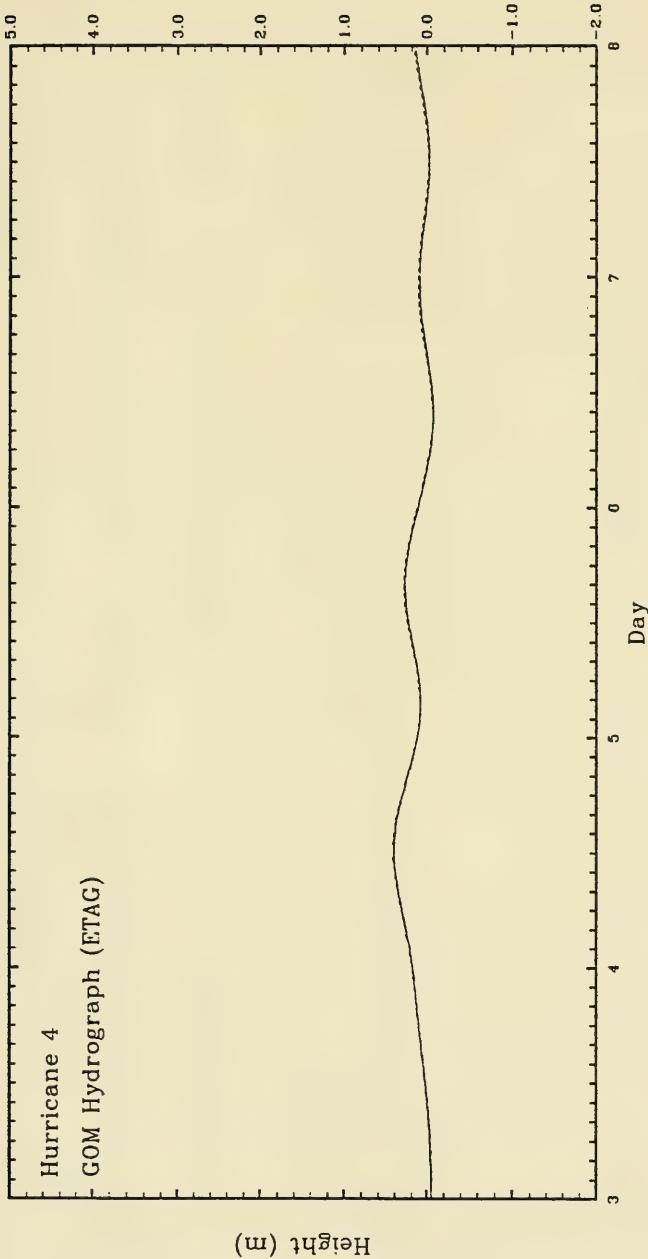
Fig. 69. Time sequences of the average water levels in the Gulf of Mexico, η_G, obtained from the simulation of HUR4. The solid line is computed by averaging water levels from every grid point in the Gulf at each time step. The dashed line is computed from the continuity equation. The datum is mean sea level.

125
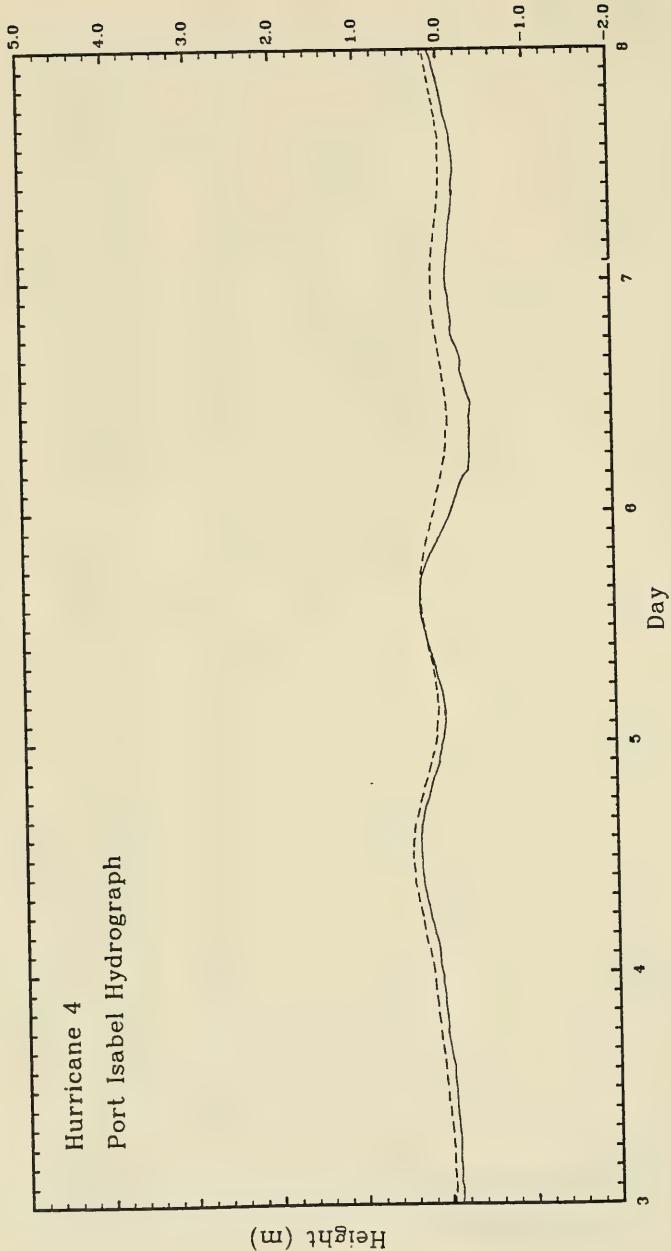
Fig. 70. Time sequences of water levels at Port Isabel (solid) and η_G (dashed) obtained from the simulation of HUR4. The datum is mean sea level.
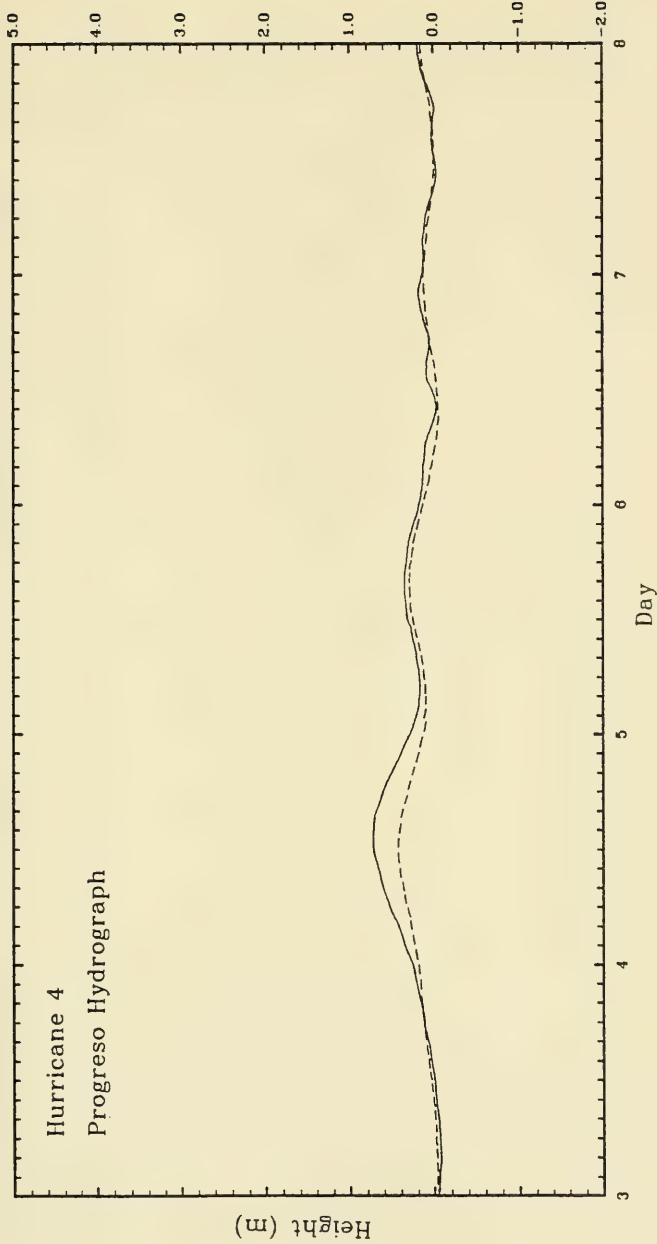
Fig. 71. Time sequences of water levels at Pregreso (solid) and η_G (dashed) obtained from the simulation of HUR4. The datum is mean sea level.
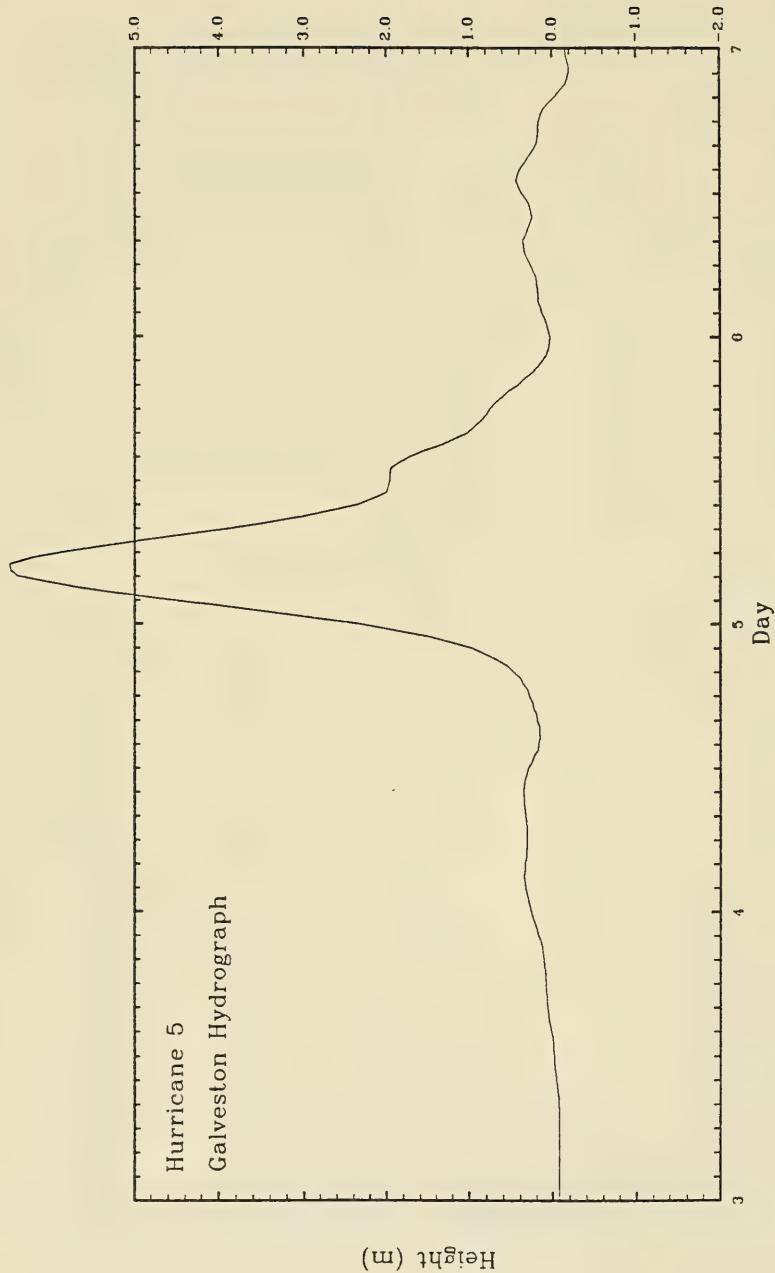
Fig. 72. Time sequence of water levels at Galveston obtained from the simulation of HUR5. The datum is mean sea level.
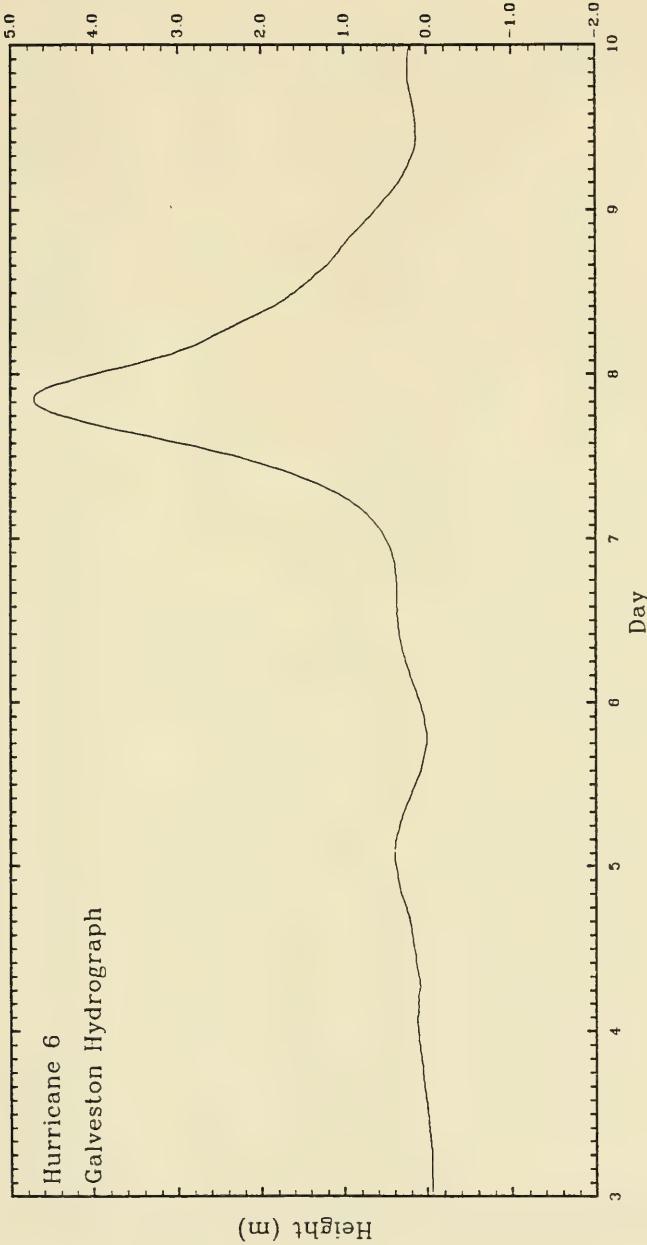
Fig. 73. Time sequence of water levels at Galveston obtained from the simulation of HUR6. The datum is mean sea level.

129
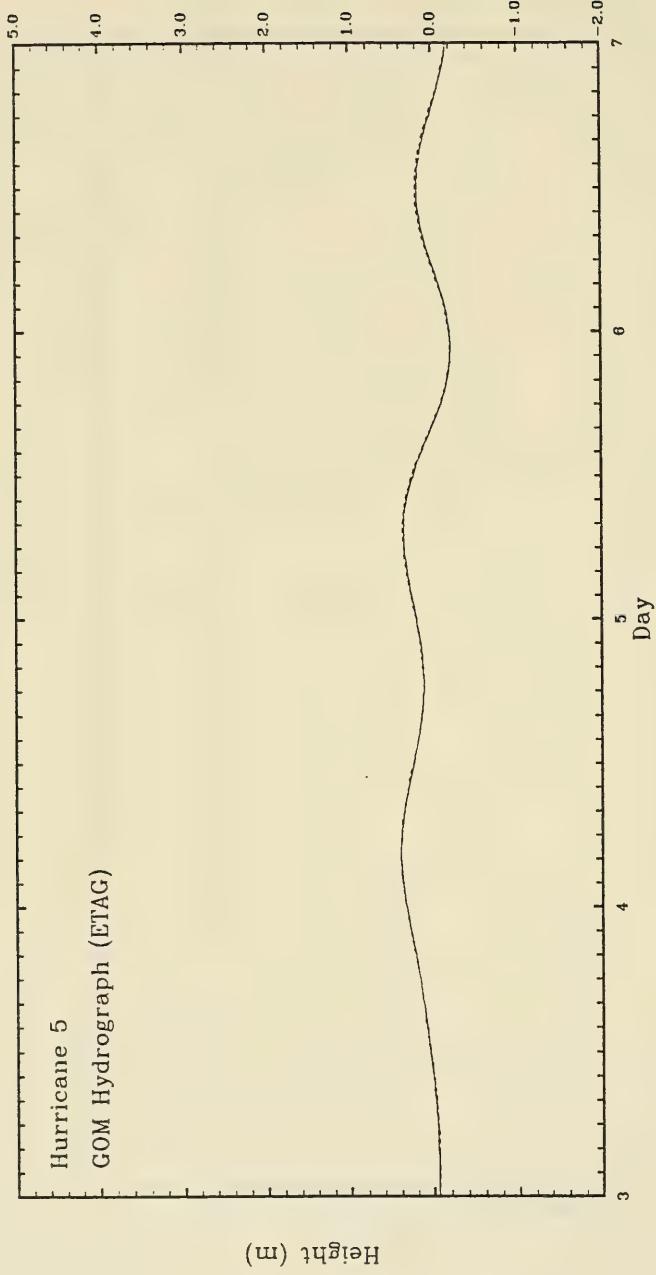
Fig. 74. Time sequences of the average water levels in the Gulf of Mexico, η_G, obtained from the simulation of HUR5. The solid line is computed by averaging water levels from every grid point in the Gulf at each time step. The dashed line is computed from the continuity equation. The datum is mean sea level.

130
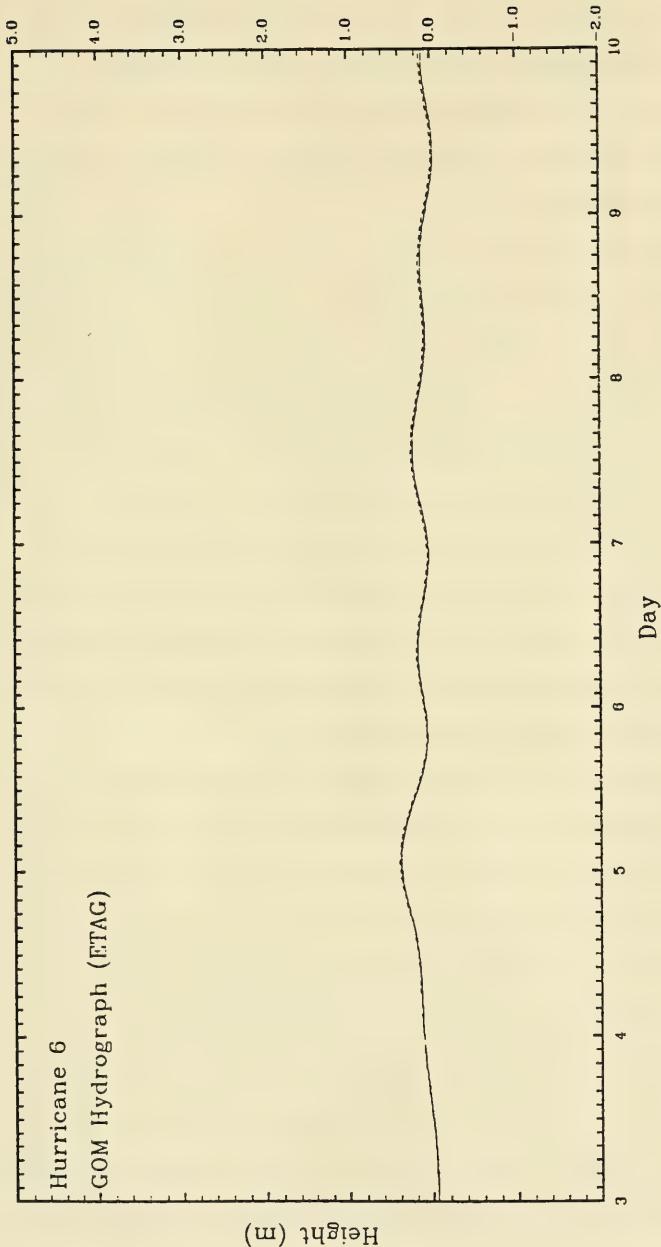
Fig. 75. Time sequences of the average water levels in the Gulf of Mexico, ηG, obtained from the simulation of HUR6. The solid line is computed by averaging water levels from every grid point in the Gulf at each time step. The dashed line is computed from the continuity equation. The datum is mean sea level.

respectively. Comparisons of the η_G hydrographs between HUR5 and HUR2 and also between HUR6 and HUR3, reveal that the largest differences occur in the early stages of the simulations. This is the same result obtained from similar comparisons between the HUR1 and HUR4 Gulf-wide modes.

Important results from the PATH1 simulations are summarized as follows. The initial rise of water level before the peak surge at Galveston exists in all cases. This rise matches the first peak of the Gulf-wide oscillation, η_G, which occurs simultaneously around the Gulf. Periods of η_G vary between 28 h to 30 h. The effects of storm size (R_{max}) are to increase both the peak surge at the coast and the magnitude of η_G. On the contrary, the effect of the storm forward speed is to increase only the peak surge at the coast (for the same size storms). Accordingly, for the remaining storm tracks (PATH2 through PATH5) only one simulation for each path using a storm of 30 km R_{max} and 25 km/h forward speed was made.

A peak surge of 4.4 m at grid point (23,46) near SW Pass, Louisiana, is obtained from the PATH2 (HUR7) simulation. The nearest station to this point is Grand Isle which is situated to the east. The time history of the computed water levels at this station is shown in Fig. 76. The highest computed water level at Grand Isle occurs a few hours earlier than the true peak surge (at grid point 23,46) while the first maximum in this hydrograph coincides with the first extreme of η_G. The sequential occurrence of the two peaks resemble the situation at Galveston in the PATH1 simulations. The η_G hydrograph shown in Fig. 77 indicates the first maximum of 0.2 m with

132
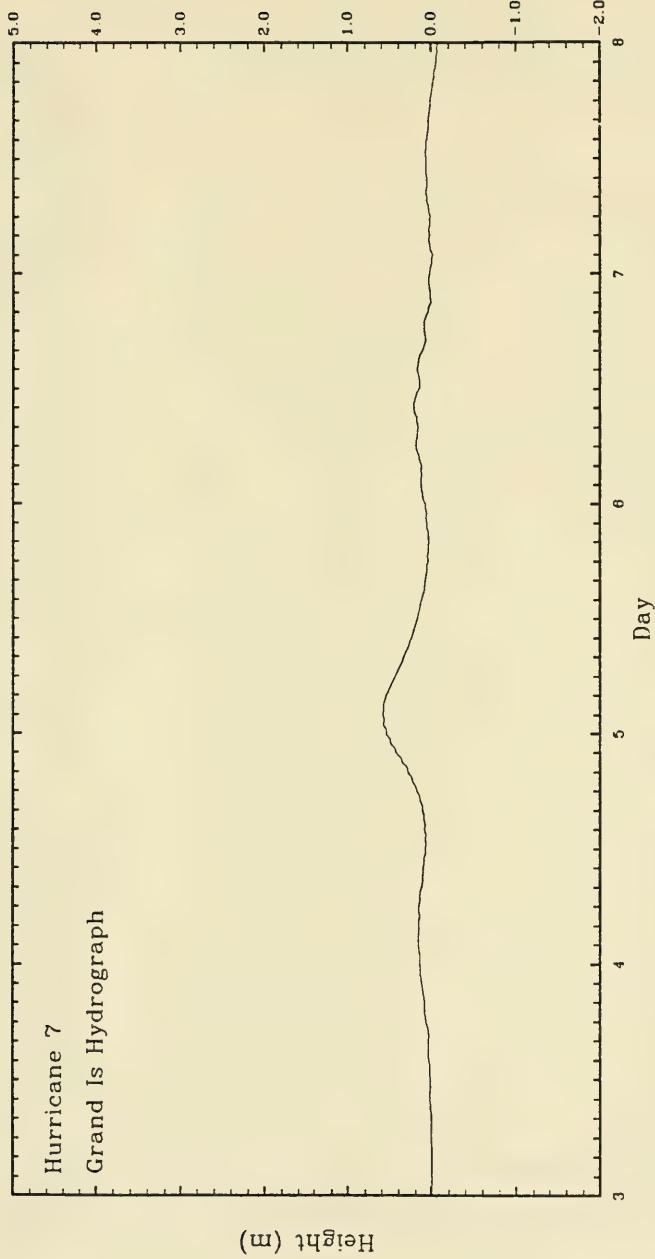
Fig. 76. Time sequence of water levels at Grand Isle obtained from the simulation of HUR7. The datum is mean sea level.
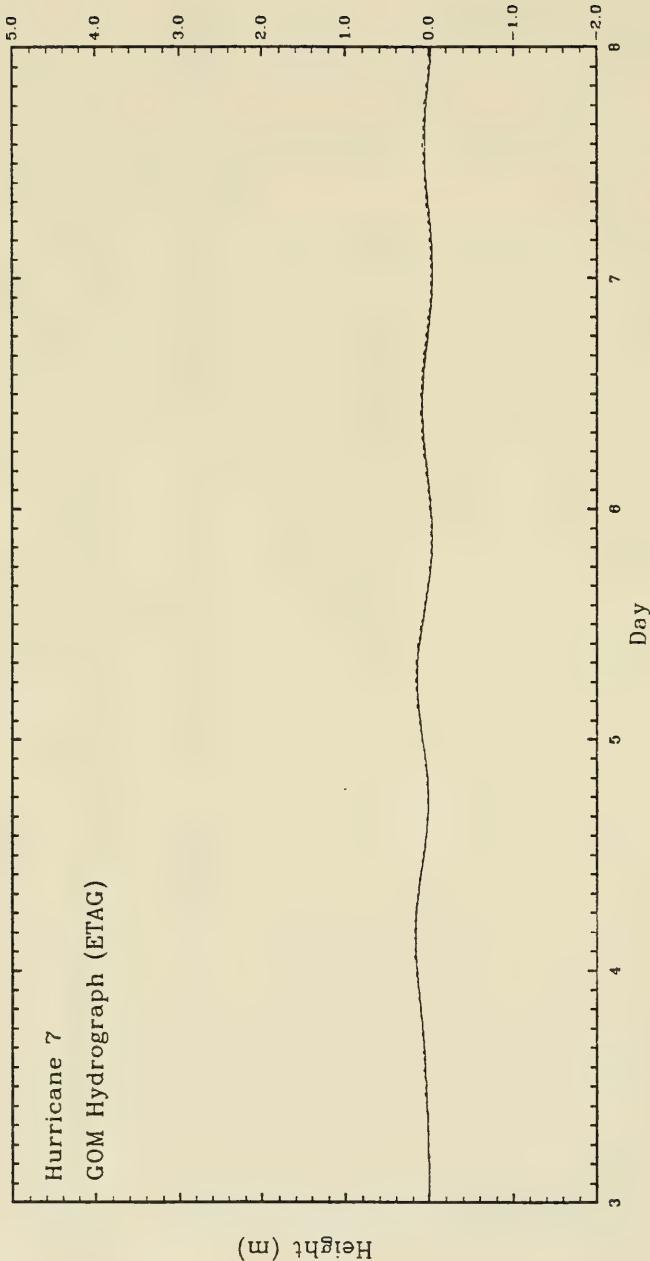
Fig. 77. Time sequences of the average water levels in the Gulf of Mexico, η_G, obtained from the simulation of HUR7. The solid line is computed by averaging water levels from every grid point in the Gulf at each time step. The dashed line is computed from the continuity equation. The datum is mean sea level.

134

δ_G of approximately 19 h. The estimated period is 28 h. This Gulf-wide oscillation resumes its dominant role in the computed hydrographs on the left side of the track from Port Isabel to Progreso.

The model storm HUR13 which traversed PATH3 produced a peak surge of 5.81 m near Burrwood (grid point 37,48). The hydrograph from Pensacola shown in Fig. 78 indicates a maximum water level of less than one meter. The difference of almost 5 m in maximum surge between Pensacola and Burrwood is probably due to the very narrow shelf width at Pensacola. The initial rise of water levels that match the first maximum of η_G is noticeable. The period, maximum peak and time lag, δ_G, determined from Fig. 79 are 26 h, 0.2 m and 11 h, respectively. The η_G signal remains detectable in the hydrographs from stations around the Gulf and again is the major part of the response at stations on the west and southwest coast.

The storm moving due north along PATH4 at 25 km/h with a 30 km radius of maximum wind (HUR19) generated a maximum surge of 6.22 m one grid block to the east of the Apalachicola sampling point. However, the simulated hydrographs show higher water levels at Cedar Key than at Apalachicola. The sampling point for Apalachicola is only half a grid block away from the path. Consequently, this station lies inside the radial distance between the storm center and the maximum wind location and is hence subjected to a smaller wind stress. The time sequence of the computed water level at Cedar Key is shown in Fig. 80. The initial rise of water level prior to the peak surge is almost undetectable. The η_G hydrograph, Fig. 81,

135
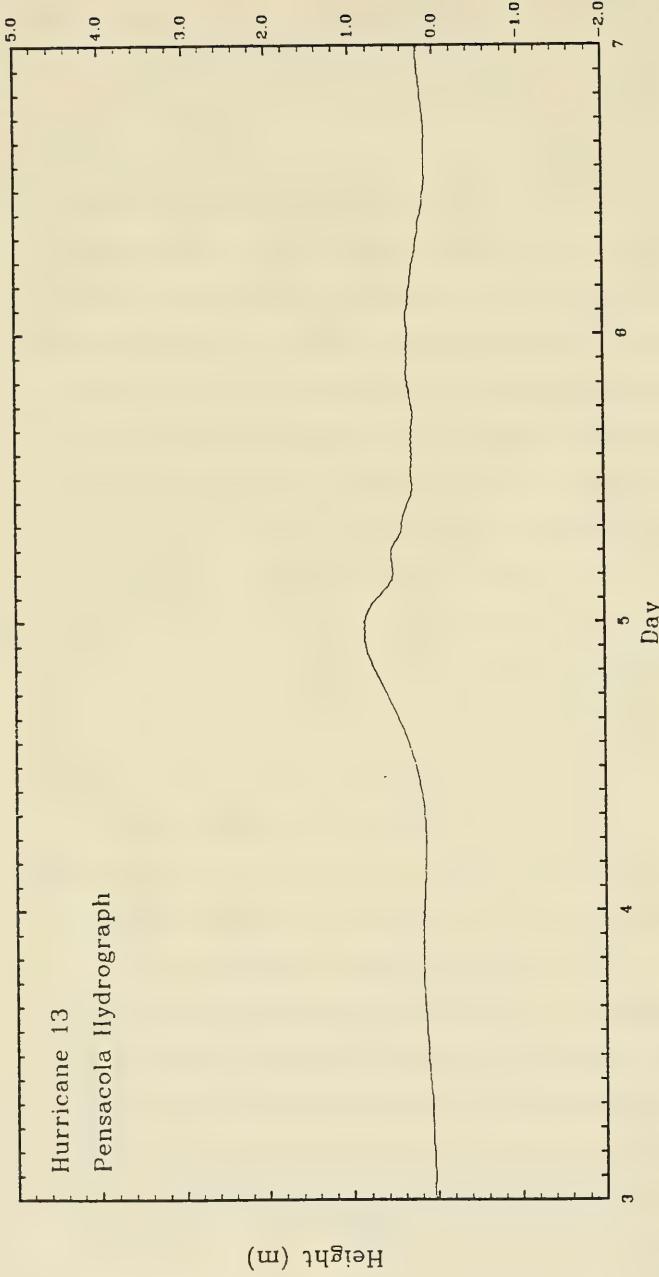
Fig. 78. Time sequence of water levels at Pensacola obtained from the simulation of HUR13. The datum is mean sea level.

136
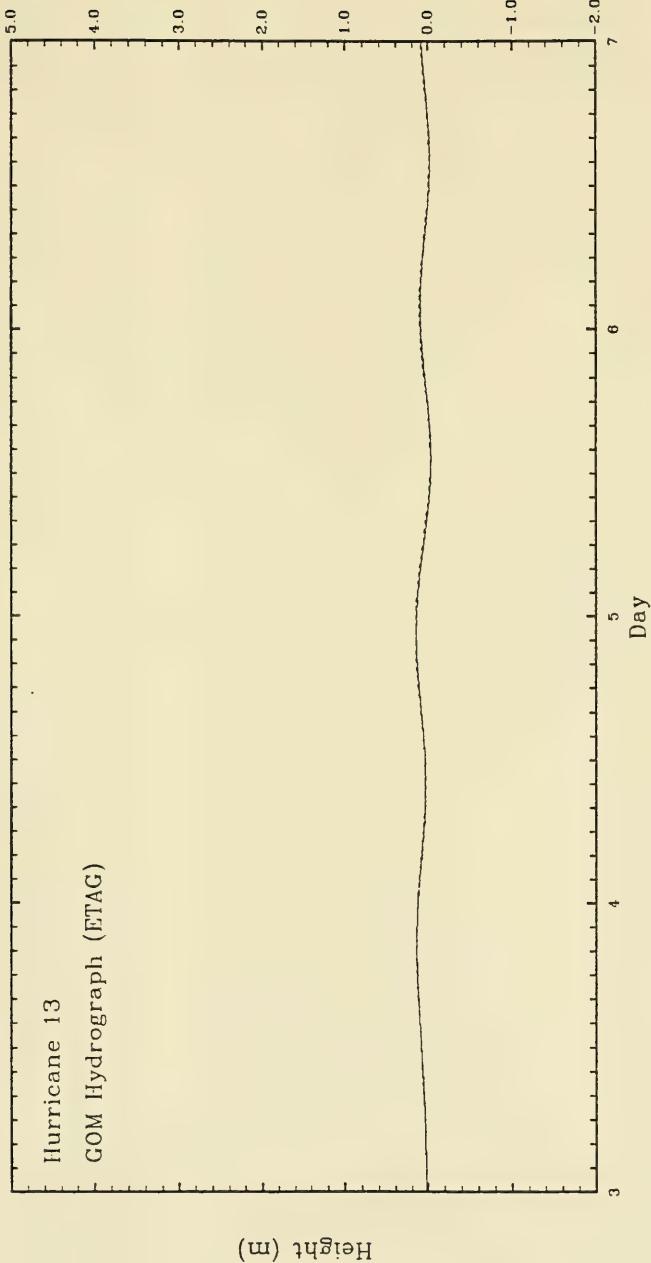
Fig. 79. Time sequences of the average water levels in the Gulf of Mexico, η_G, obtained from the simulation of HURl3. The solid line is computed by averaging water levels from every grid point in the Gulf at each time step. The dashed line is computed from the continuity equation. The datum is mean sea level.
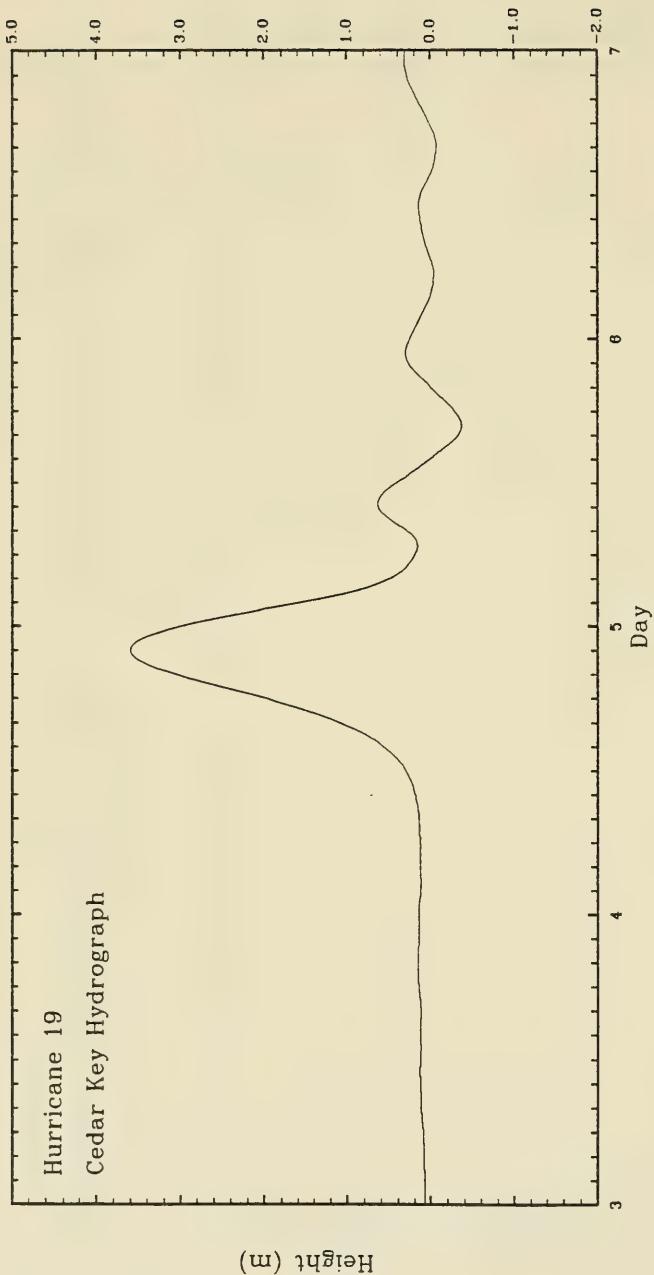
Fig. 80. Time seuqence of water levels at Cedar Key obtained from the simulation of HUR19. The datum is mean sea level.

138
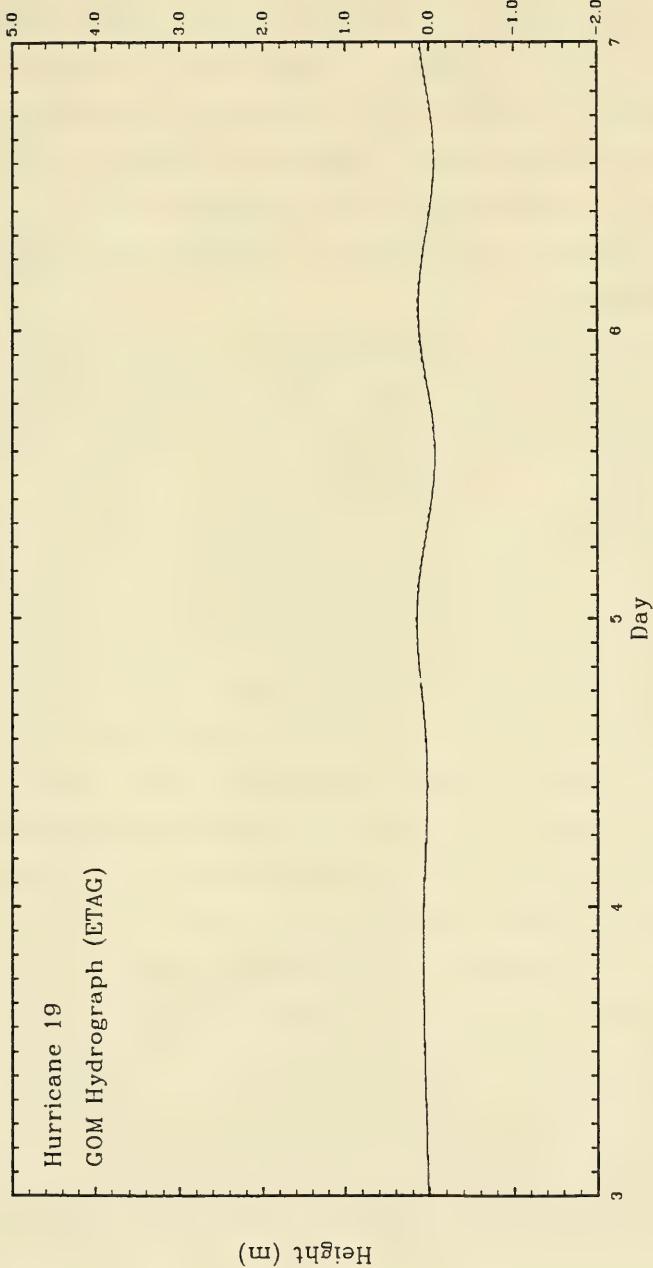
Fig. 81. Time sequences of the average water levels in the Gulf of Mexico, η_G, obtained from the simulation of HUR19. The solid line is computed by averaging water levels from every grid point in the Gulf at each time step. The dashed line is computed from the continuity equation. The datum is mean sea level.

139

indicates the first maximum of only a few centimeters. The estimated period of η_G and δ_G are 27 h and 12 h, respectively. In spite of its small amplitude, η_G still dominates the response in the hydrographs from Pensacola counterclockwise to Progreso. The striking result however, is the generation of a 12 h period oscillation after the peak surge. This mode is also observed in the Apalachicola and St. Petersburg hydrographs.

The very small initial rise of water levels along the Florida shelf prior to the peak surge, together with the generation of the 12 h period oscillation motivated three additional storm runs for PATH4. All have large R_{max}, but take three different forward speeds.

The medium speed and large radius storm (HUR22) produced a 8.53 m maximum surge to the north of Cedar Key. The simulated hydrograph at Cedar Key, Fig. 82, shows a peak surge of more than 5 m followed by a strong 12 h period oscillation. The presence of the initial rise of water level is hardly seen. Figure 83 reveals that a first maximum of less than 0.1 m occurs at approximately 1800 h on day 4. At this time the water level at Cedar Key is decreasing and reaches a minimum at 1200 h on day 4. The stipulated path and a large radius of maximum wind resulted in larger draw down of water level in the early stages due to stronger offshore directed wind preceding the storm as compared to the simulation of HUR19. The hydrograph of η_G shows a maximum peak of 0.24 m at 2300 h on day 4. An estimated period of 29 h is determined from Fig. 83. Once again, the hydrographs from stations on the left side of the track from Pensacola to Progreso seem to depart from η_G signal, the situation
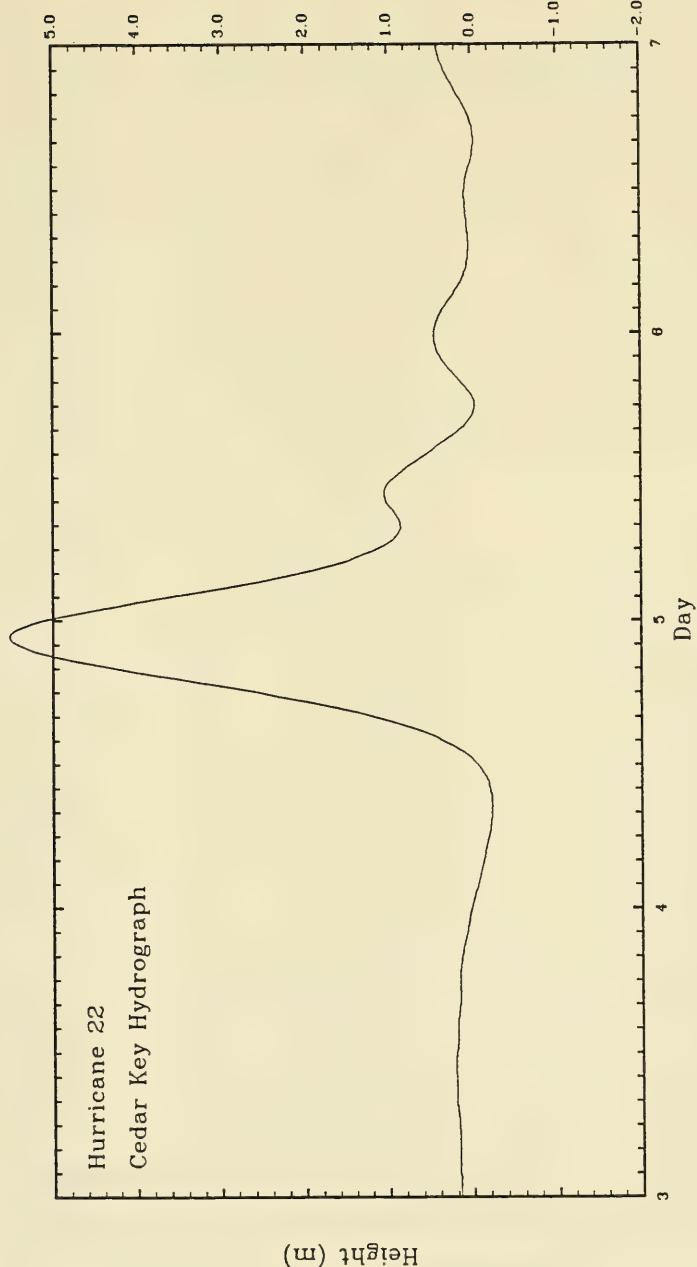
Fig. 82. Time sequence of water levels at Cedar Key obtained from the simulation of HUR22. The datum is mean sea level.

141
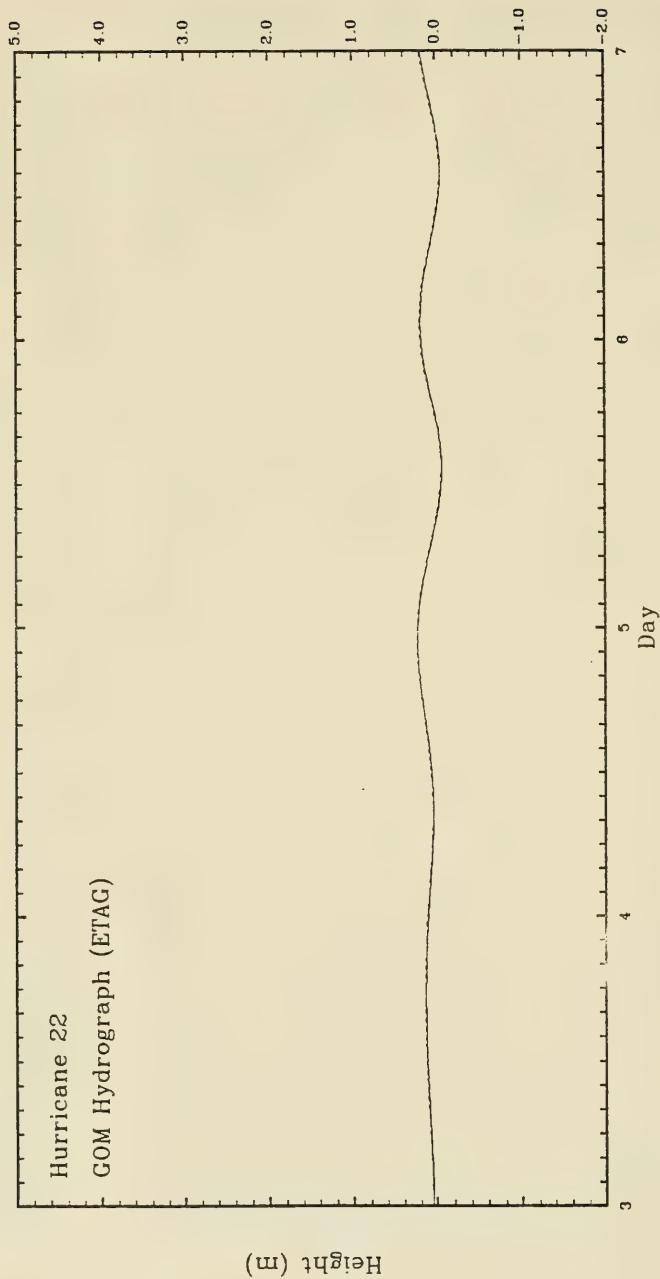
Fig. 83. Time sequences of the average water levels in the Gulf of Mexico, η_G, obtained from the simulation of HUR22. The solid line is computed by averaging water levels from every grid point in the Gulf at each time step. The dashed line is computed from the continuity equation. The datum is mean sea level.

142

found in simulating large storms on PATH1.

A maximum surge of 8.52 m occurring at the same location as in the HUR22 run was generated by HUR23. The time sequence of water levels at Cedar Key is shown in Fig. 84. Due to a fast speed and a relatively short distance across the Gulf, the maximum surge at Cedar Key occurs so early that it is not possible to identify the existence of an initial rise of water levels. The 12 h mode however, remains noticeable. The η_G signal (Fig. 85) reaches the first peak of 0.2 m at 1400 h on day 3, which is approximately 9 h after the storm passed Yucatan Strait. The highest peak of η_G is 0.23 m and the period is estimated at 25 h.

Reducing the forward speed of the storm to 15 km/h (HUR24), decreases the maximum surge to 7.32 m. Figure 86 illustrates two negligible water level maxima before the peak surge at Cedar Key. The 12 h mode after the peak surge is again excited. The 26 h period of the small amplitude η_G signal is shown in Fig. 87. It is interesting but not yet understood why the first maximum of η_G occurred before the storm center entered the Gulf. The δ_G determined from the second maximum of η_G is approximately 20 h.

These four runs on PATH4 repeatedly gave the same results regarding the effects of forward speed and radius of maximum wind. The notable result is the excitation of the 12 h mode on the Florida shelf. It is important to emphasize that this model admitted no tidal forcing. Reid and Whitaker (1981) found a near resonant response on the Florida shelf, with the greatest signal near Cedar Key, to direct forcing by the M_2 tide potential. Figure 88 (Ichiye

143
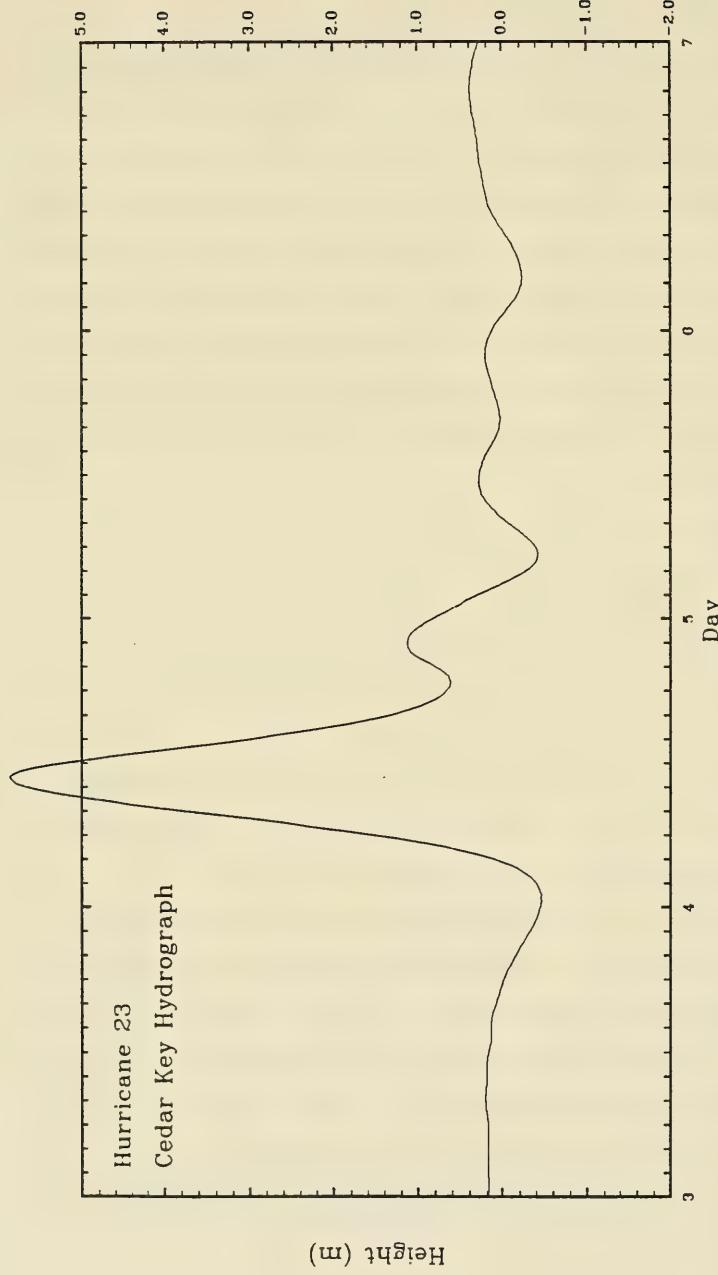
Fig. 84. Time sequence of water levels at Cedar Key obtained from the simulation of HUR23. The datum is mean sea level.

144
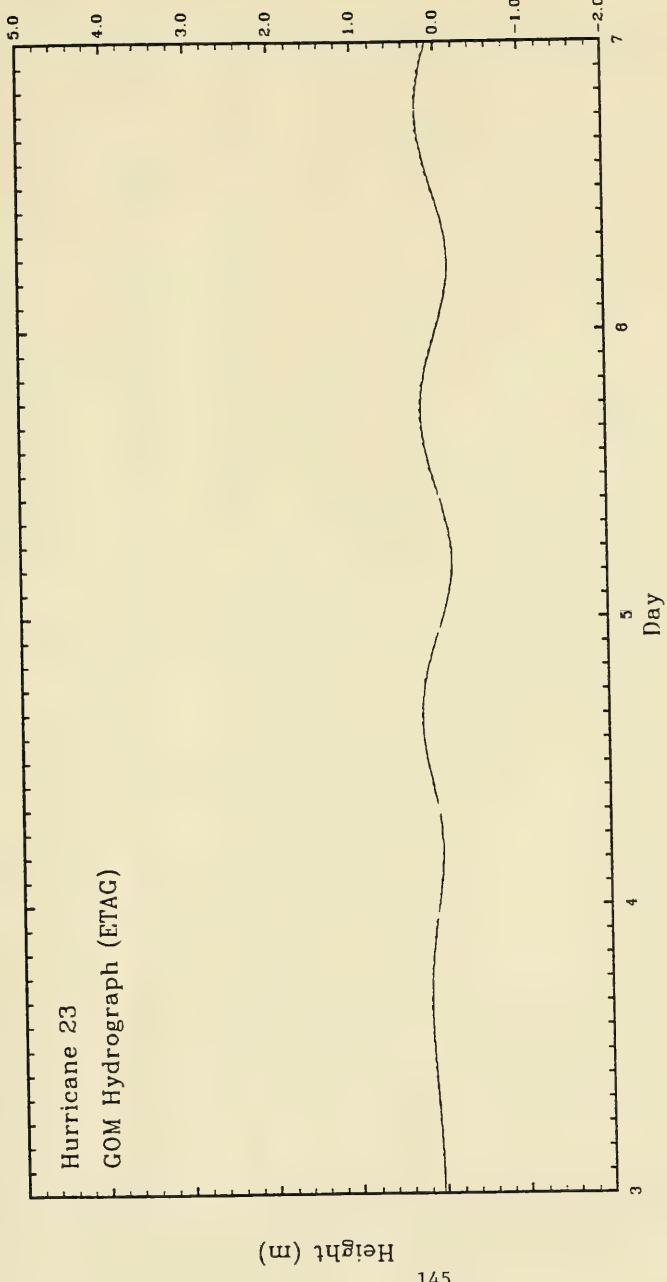
Fig. 85. Time sequences of the average water levels in the Gulf of Mexico, η_G, obtained from the simulation of HUR23. The solid line is computed by averaging water levels from every grid point in the Gulf at each time step. The dashed line is computed from the continuity equation. The datum is mean sea level.

145
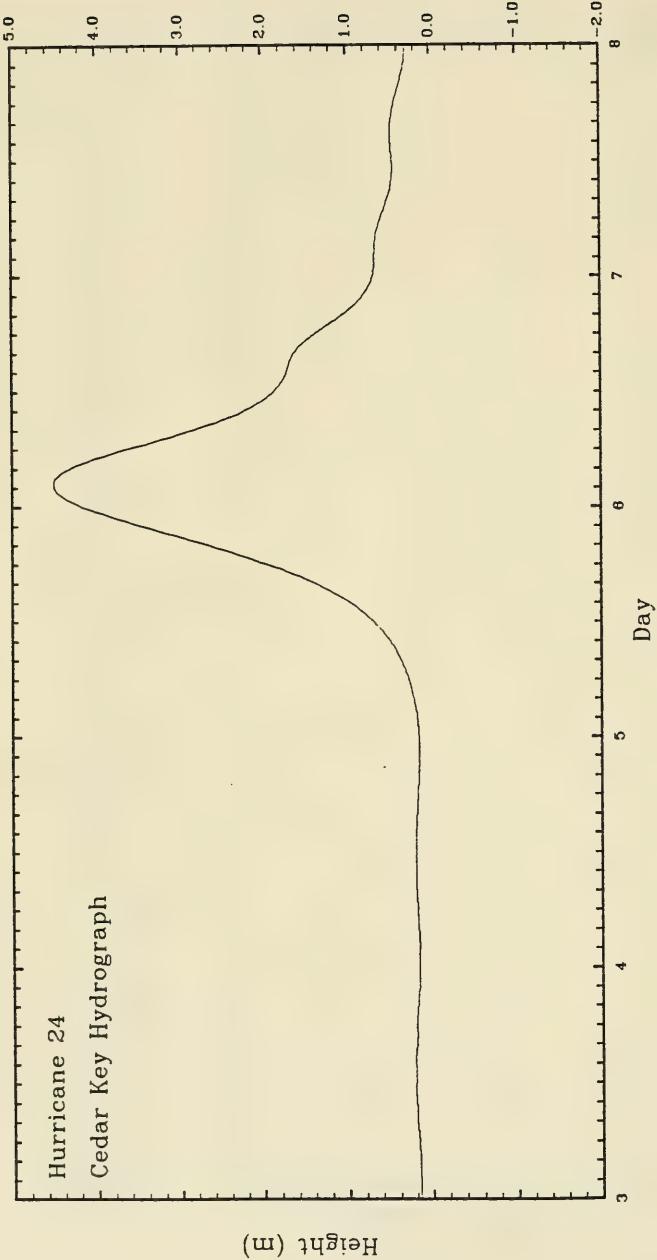
Fig. 86. Time sequence of water levels at Cedar Key obtained from the simulation of HUR24. The datum is mean sea level.
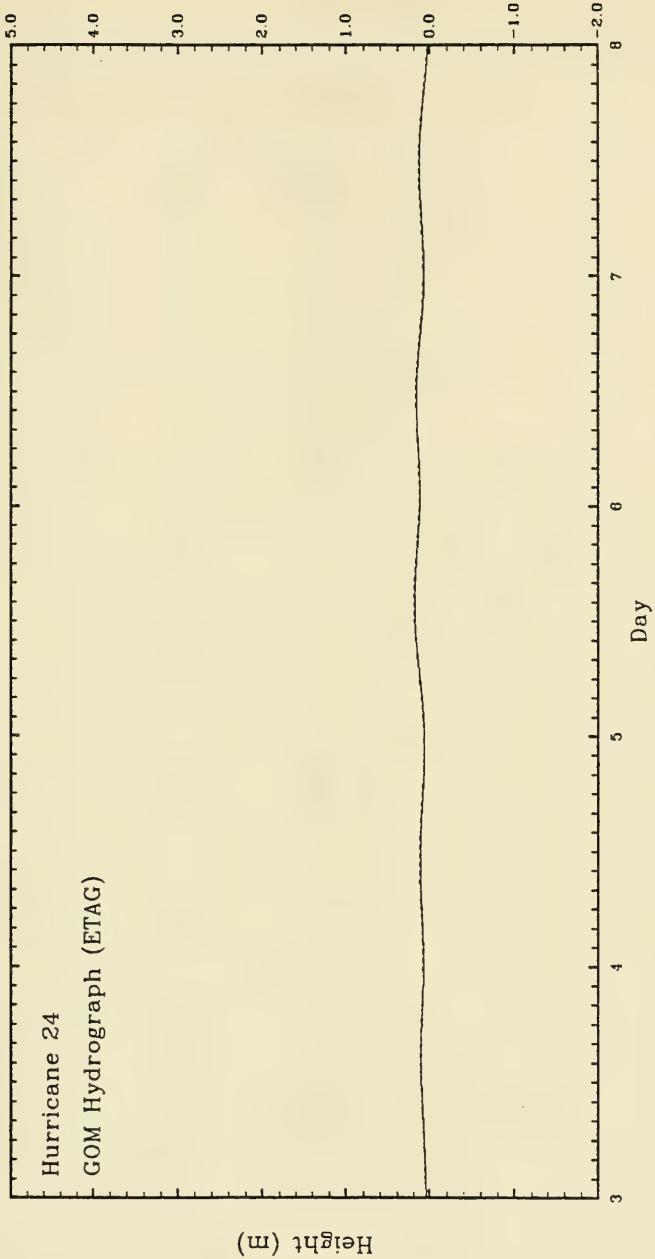
Fig. 87. Time sequences of the average water levels in the Gulf of Mexico, η_G, obtained from the simulation of HUR24. The solid line is computed by averaging water levels from every grid point in the Gulf at each time step. The dashed line is computed from the continuity equation. The datum is mean sea level.

147
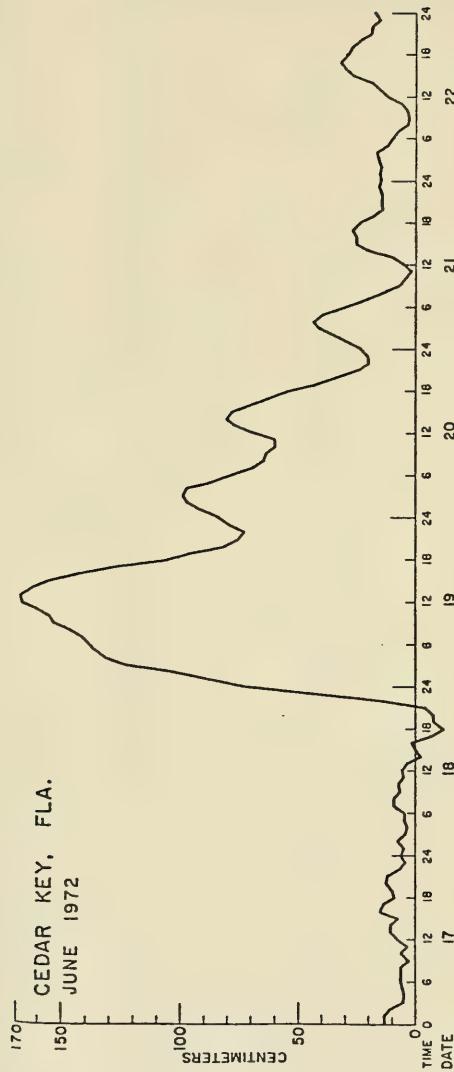
Fig. 88. Observed water levels (with tide removed) at Cedar Key during hurricane Agnes in 1972 (after Ichiye et al., 1973). The datum is gauge mean low water.

148

et al., 1973) shows the recorded water level with tidal signal removed at Cedar Key during the passage of hurricane Agnes in 1972. The 12 h period oscillation is obvious.

The maximum surges on the order of 7-8 m on the Florida shelf found in the PATH4 simulations are probably too large. Reid and Whitaker (1981) showed that the response on the Florida shelf to direct forcing by the M_2 tide potential was very sensitive to the local friction coefficient. Therefore, the simulation of HUR23 was repeated with a friction coefficient of 7.5×10^{-4} m/s. This coefficient is applied to the entire computing domain since only the response on the Florida shelf is the primary concern in this simulation. The maximum surge generated (6.23 m) is decreased by about 25 % from that generated by the same storm simulation with the smaller friction coefficient. The hydrographs from stations on the Florida shelf (not shown) clearly demonstrated the effect of larger friction. Examination of the remaining hydrographs reveals no significant changes in water levels due to increasing friction, even on the Texas-Louisiana shelf region. Presumably these stations are located too far to the left of the storm track such that the corresponding currents and bottom stress are small.

The PATH5 storm, HUR25, produced a 5.4 m maximum surge near Galveston, Fig. 89. The sharp drop of water levels before the peak surge is caused by a direct offshore wind stress. The maximum peak of η_G (Fig. 90) is less than 0.1 m .The estimated period of η_G for this run is 32 h.
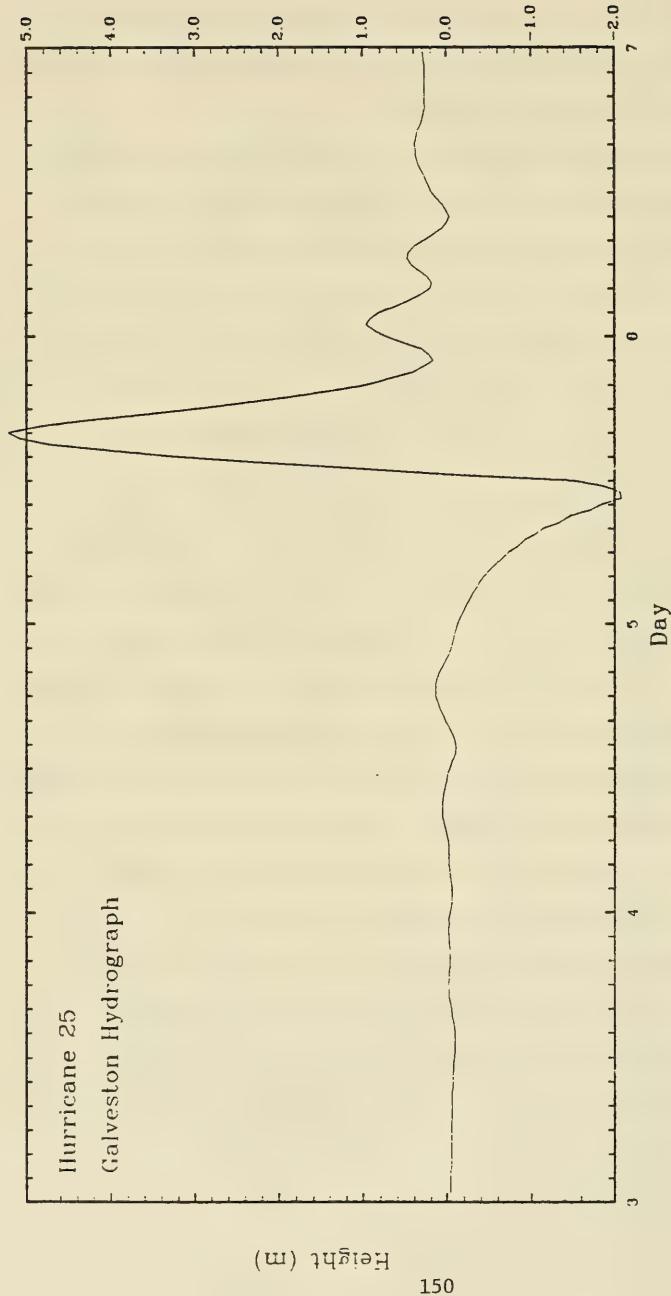
Fig. 89. Time sequence of water levels at Galveston obtained from the simulation of HUR25. The datum is mean sea level.

150
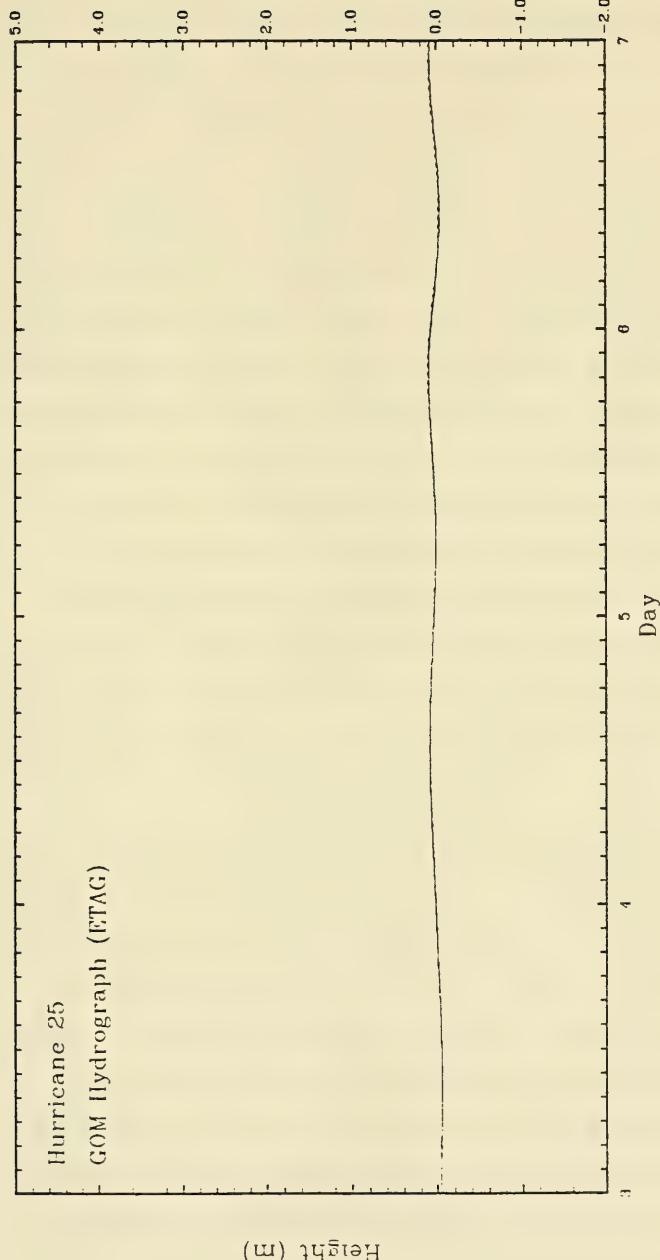
Fig. 90. Time sequences of the average water levels in the Gulf of Mexico, η_G, obtained from the simulation of HUR25. The solid line is computed by averaging water levels from every grid point in the Gulf at each time step. The dashed line is computed from the continuity equation. The datum is mean sea level.

The relationship between the magnitude of η_G and the net volume volume transport through the ports discussed in the simulation of hurricane Allen is reinvestigated. Figures 91 through 93 show the barotropic volume transport through the Florida port and Yucatan Strait, and the difference of the two components obtained from the HUR1, HUR4 and HUR25 simulations, respectively. It can be seen from the figures that the larger the net volume transport through the ports the larger the magnitude of η_G. This result should be expected based on continuity. The first maximum of the total volume transport for HUR4 is approximately 10 x 10^6 m^3/s which is about a factor of 2 larger than that produced by HUR1. The same ratio of maximum η_G obtained from the two storms provide quantitative evidence for relating η_G to the net periodic transport. Note that the volume transport from the HUR25 simulation and the associated η_G is very small. The initial position of this storm and associated wind field gives smaller flows through the two openings as compared to HUR1 and HUR4.

The average period of the net periodic volume transport in each case is about the same as the period of the corresponding η_G signals. The η_G signal however, is approximately 90° out of phase (lag) with the total periodic transport. This result resembles the uninodal seich in a one dimensional channel. However, the ubiquity of the η_G signal in the hydrographs around the Gulf implies that the net periodic transport acts like a single port forcing and excites the entire Gulf proper to oscillate with a node at the port. In other words, the η_G oscillation is a Helmholtz mode excited by the net

152
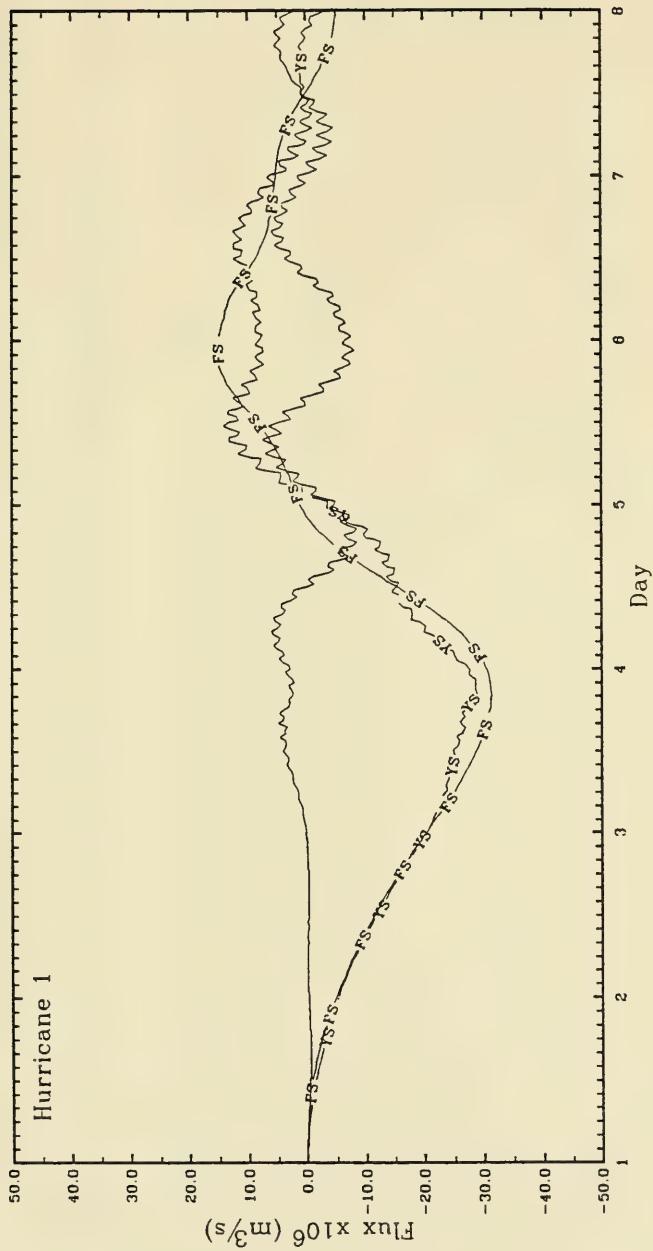
Fig. 91. Time sequences of volume transport through Florida (FS) and Yucatan (YS) Straits obtained from the simulation of HUR1. The unlabelled curve is the net differential volume transport.
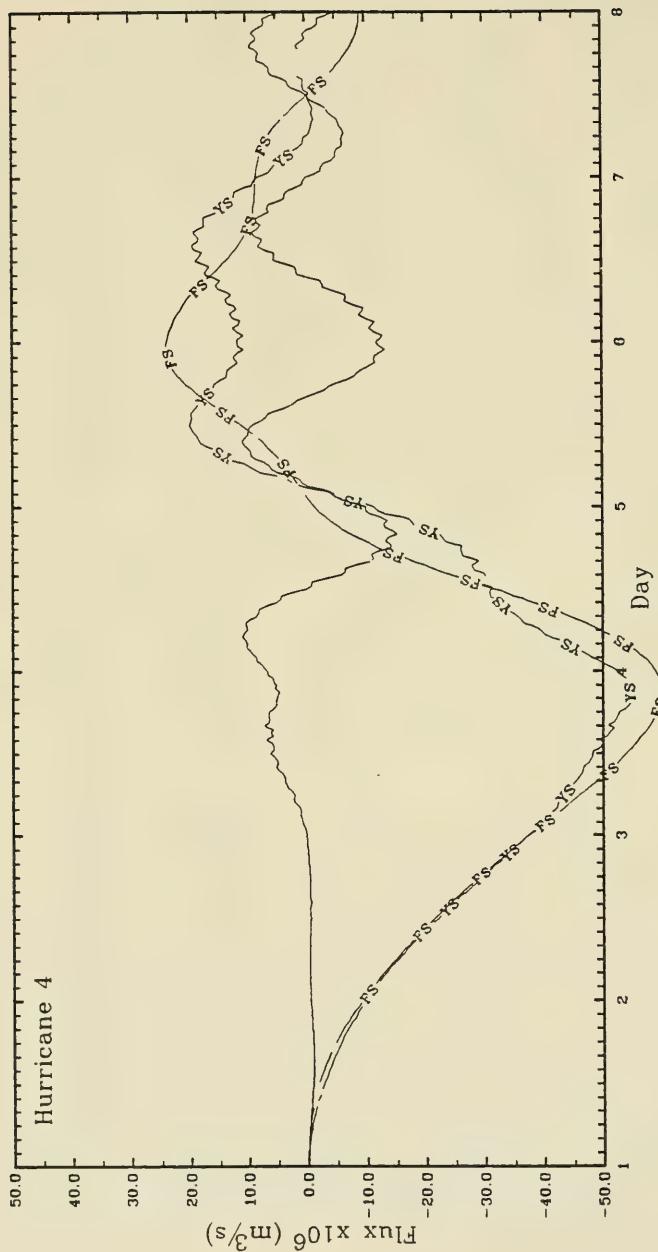
Fig. 92. Time sequences of volume transport through Florida (FS) and Yucatan (YS) Straits obtained from the simulation of HUR4. The unlabelled curve is the net differential volume transport.

154
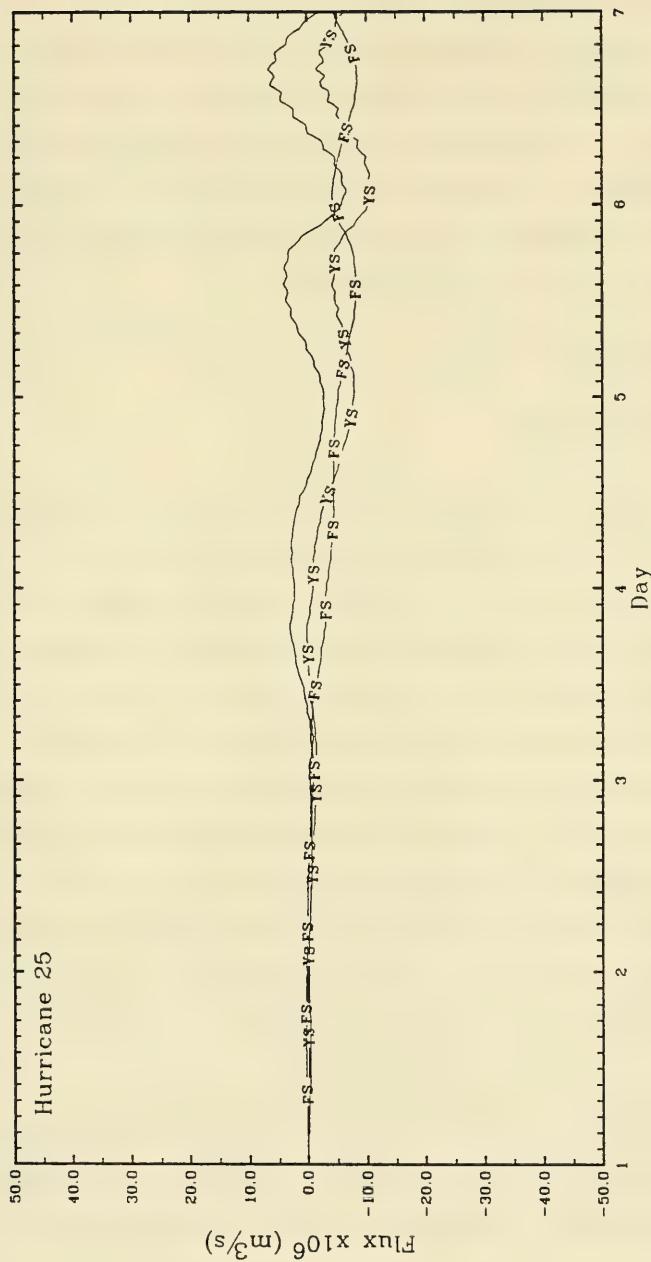
Fig. 93. Time sequences of volume transport through Florida (FS) and Yucatan (YS) Straits obtained from the simulation of HUR25. The unlabelled curve is the net differential volume transport.

155

periodic transport through the ports.

Table 2 summarizes the peak surge at the digitized coastline for each storm. Locations where the peaks occur are given in terms of the grid point (I,J). The peaks and periods (T_G) of the η_G signal obtained from each case are given in columns 7,8 and 13,14. The time lag of the first maximum of η_G after the center of the storms entered Yucatan Strait, δ_G, is also given in Table 2.

5. Long period variation of η_G

a) The 3.4 day volume mode

The η_G signals obtained from all the synthetic storm simulations have a long period variation superimposed on their average 28 h period. This slow variation is not readily observable except for the one generated by HUR5. Therefore, model HUR5 was used to investigate this long period variation of the Helmholtz mode (η_G). This simulation used the same storm characteristics of the original HUR5 hurricane. However, forcing was allowed only over the first 3 days 22 h of the simulation. The calculations were continued for a total of 21 days to provide a clear history of the free modes in the Gulf and Cayman Sea. Time histories of the mean external height anomalies of the two basins over the full simulation period are shown in Fig. 94. The arrow indicates when all forcing was set to zero. At this time HUR5 was centered at 25.44°N and 90.86°W.

The most striking feature of this simulation is the very long mode which dominates the Cayman response. The period of this mode is approximately 3.4 days. The half-cycle means of η_G over the last 7

Table 2. Summary of results from the simulations of synthetic storms traversing 5 selected paths

			R_{max} = 30 km						R_{max} = 60 km				
PATH	V_f (km/h)	STORM	PEAK† COAST (m)	AT (I,J)	PEAK§ η_G (m)	T_G (hrs)	δ_G^* (hrs)	STORM	PEAK† COAST (m)	AT (I,J)	PEAK§ η_G (m)	T_G (hrs)	δ_G^* (hrs)
1	35	HUR2	4.20	14,46	0.20	28	17	HUR5	6.50	14,46	0.40	28	17
	25	HUR1	3.52	14,46	0.22	30	24	HUR4	5.76	16,47	0.42	30	24
	15	HUR3	2.83	10,43	0.22	30	24	HUR6	4.71	14,48	0.38	30	24
2	25	HUR7	4.40	23,46	0.16	28	18	–	–	–	–	–	–
3	25	HUR13	5.81	37,48	0.14	27	11	–	–	–	–	–	–
4	35	–	–	–	–	–	–	HUR23	8.52	57,48	0.23	25	8
	25	HUR19	6.22	54,48	0.14	27	12	HUR22	8.53	57,48	0.24	29	8
	15	–	–	–	–	–	–	HUR24	7.23	57,48	0.20	27	8
5	25	HUR25	5.40	16,47	0.09	–	–	–	–	–	–	–	–

(†) is the maximum surge at the digitized coastline.
(§) is the maximum surge at the shelf break after the inverted barometric term has been removed.
(*) is the time lag between the time at which the storm enters the Gulf through Yucatan Strait to the time of the first maximum of η_G.
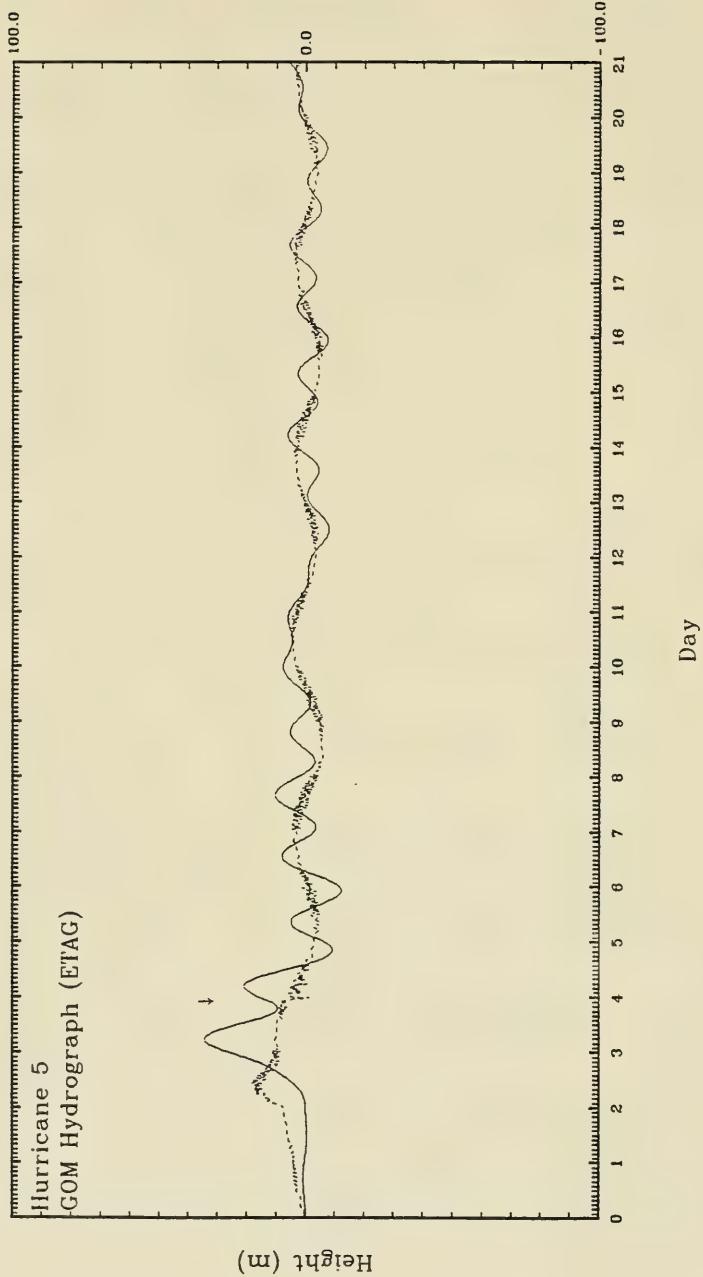
Fig. 94. Time sequences of the averaged water level in the Gulf of Mexico (solid) and in the Cayman Sea (dashed) obtained from the long term simulation of HUR5. The datum is mean sea level.

158

days of the simulation correspond very closely to the 3.4 day mode of the Cayman Sea. This implies a complicated response of the Gulf-Cayman Sea system which oscillates in unison at a period of 3.4 days. Simultaneously the Gulf of Mexico exhibits a 28 h volume mode superimposed on the long period oscillation. The latter mode can clearly affect the time-dependent amplitudes assigned to η_G.

The intriging questions of course concern the nature of the 3.4 day oscillation. Definitive answers are outside the scope of this research. However, the influence of the earth's rotation could be so readily evaluated that it was decided to repeat the above simulation with the Coriolis acceleration set to zero. These results are shown in Fig. 95.

The 3.4 day mode was not excited in the non-rotating Gulf and Cayman basins. Inspection of the accompanying digital means did not reveal a discernable 3 day mode. Moreover, the digital time series show that the 28 h volume mode in the Gulf was reduced to amplitudes on the order of a centimeter.

Notice that the paired histories of water level with (cf. Fig. 94, p. 158) and without (Fig. 95) rotation are different over the entire period of forcing (first 3 days 22 h). This suggests that the excitation mechanism for the Helmholtz mode in the Gulf and the 3.4 day Gulf-Cayman system mode is contingent on the earth's rotation.

159
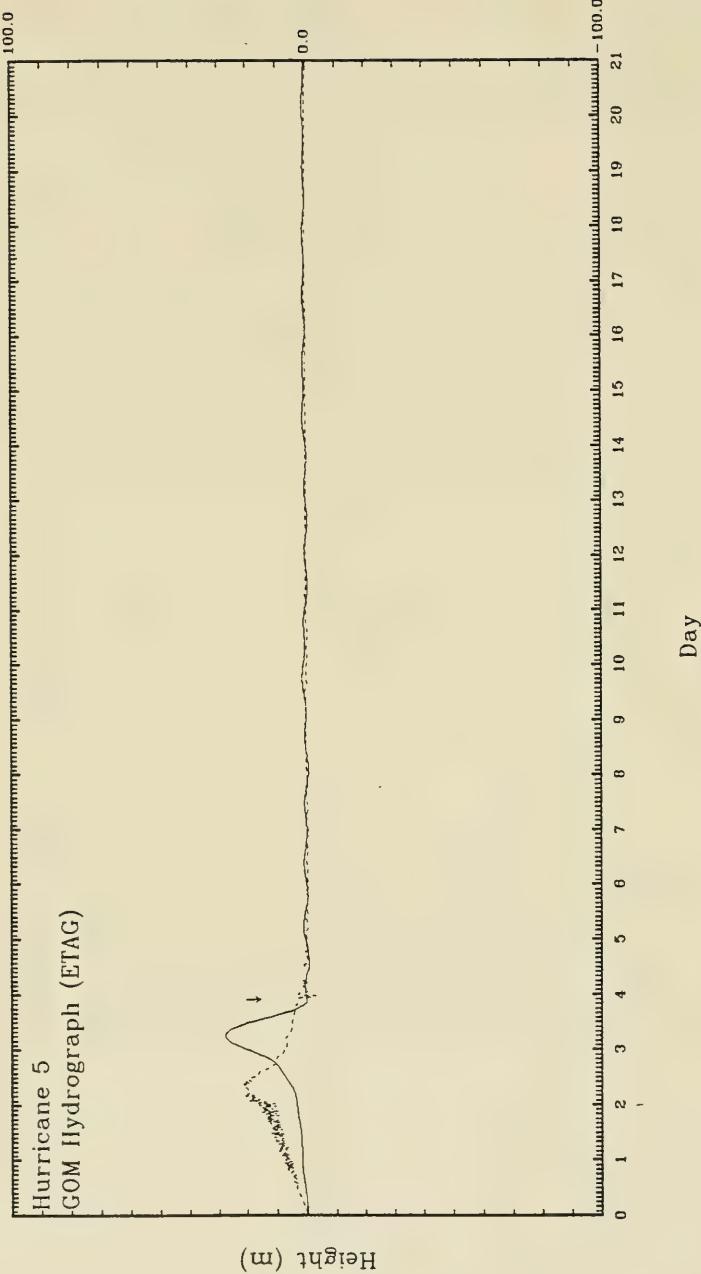
Fig. 95. Time sequences of the averaged water level in the Gulf of Mexico (solid) and in the Cayman Sea (dashed) obtained from the long term simulation of HUR5 with no rotation. The datum is mean sea level.

160

b) The 6.5 day tilt mode

Time histories of volume transport obtained from the 21 day simulation of HUR5 with rotation are presented in Fig. 96. A prominent feature is the 6.5 day period oscillation for the transports through both Florida and Yucatan Straits.

The water level from this long simulation was sampled at 12 stations, six of which are the same as those given in Fig. 12. The remaining six stations are Panama City, Tampico, Coatzacoalcas, Dimas (northern coast of Cuba), Central Gulf, Eastern Gulf and Western Gulf. The hydrograph at Key West (Fig. 97) shows a strong 6.5 day mode with an average amplitude of 0.50 m. Superimposed on this long period mode is the 28 h volume mode. Careful inspection of the remaining hydrographs indicates the presence of the 6.5 day oscillation but with a much smaller amplitude as compared to that in the Key West hydrograph. Hydrographs at Galveston (Fig. 98) and Dimas (Fig. 99) show that the water levels at the two stations are 180° out-of-phase. For example, at 1600 h on day 8 the water level at Galveston is 0.05 m while at Dimas it is -0.05 m. The three deep-water hydrographs are near zero at this time (note that the Central Gulf station is approximately midway between Dimas and Galveston). This 0.1 m differential in water surface elevation is possibly a geostrophic tilt since all the forcings were set to zero well before this time. Large space and time scales and a small surface expression are indicative of a vorticity (or quasi-geostrophic tilt) mode.

161
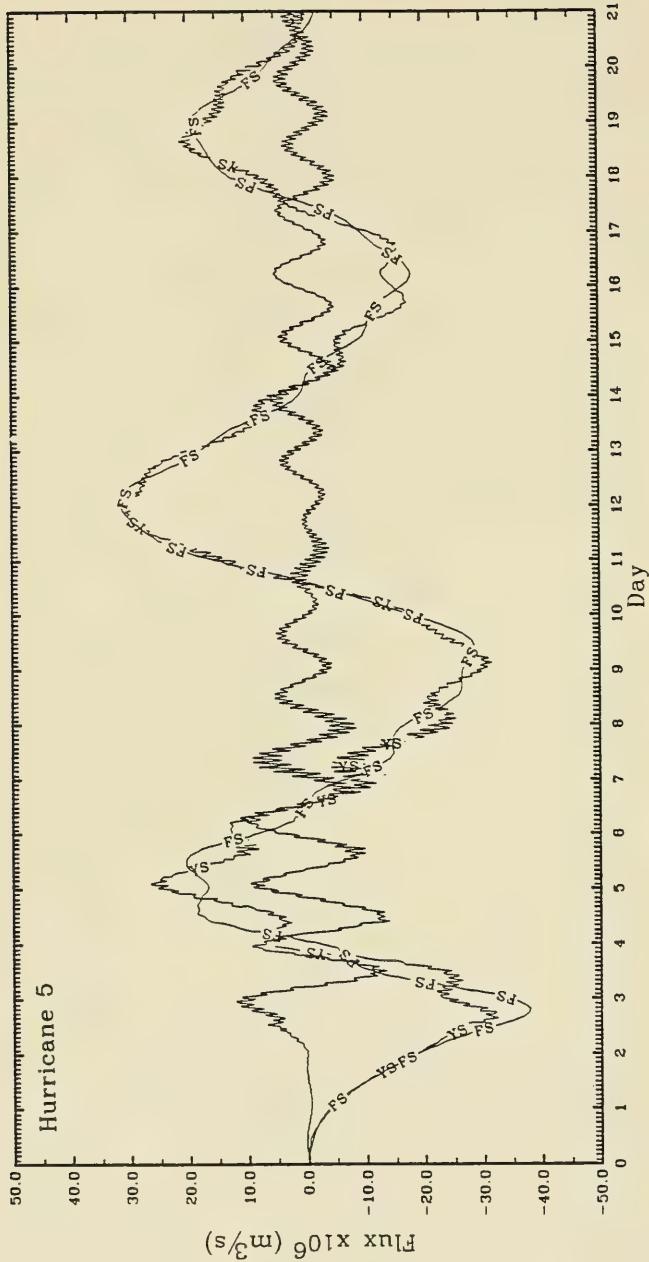
Fig. 96. Time sequences of volume transport through Florida (FS) and Yucatan (YS) Straits obtained from the long term simulation of HUR5. The unlabelled curve is the net differential volume transport.
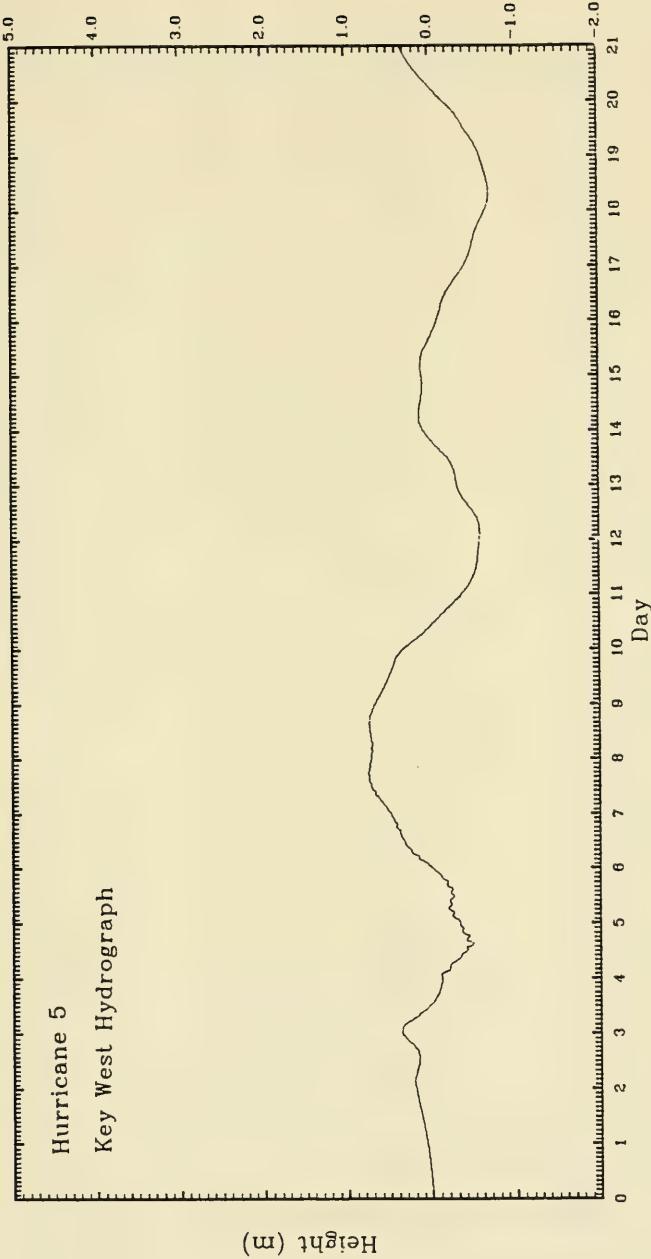
Fig. 97. Time sequence of water levels at Key West obtained from the long term simulation of HUR5. The datum is mean sea level.
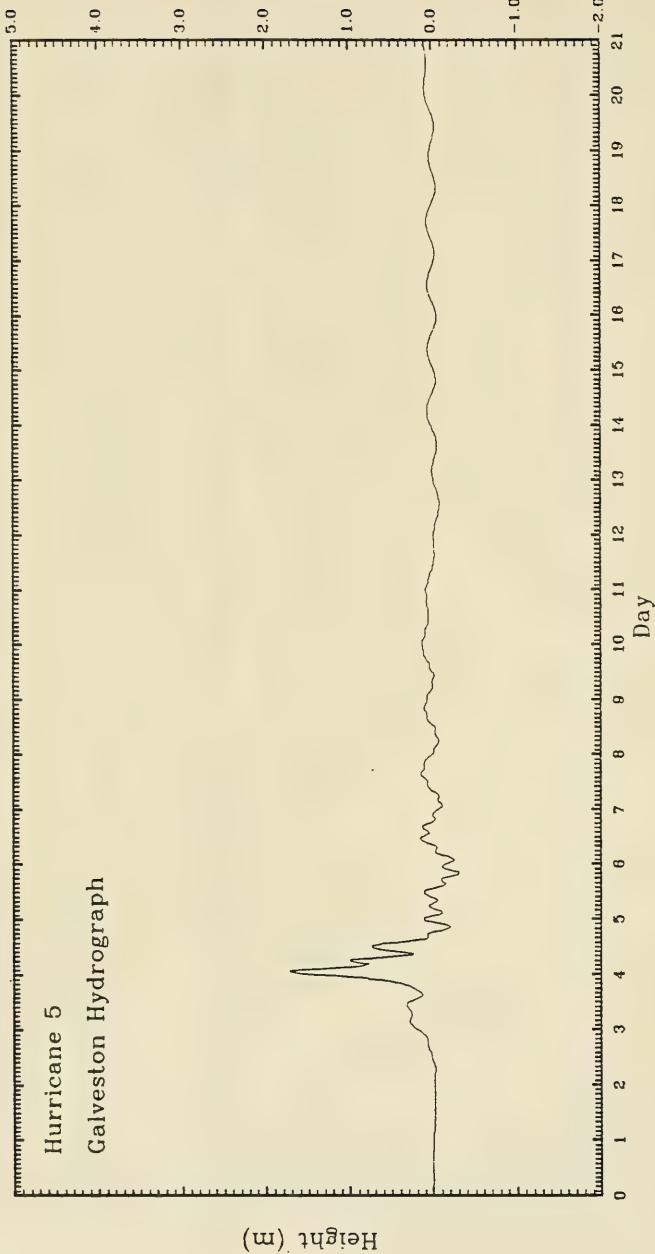
Fig. 98. Time sequence of water levels at Galveston obtained from the long term simulation of HUR5. The datum is mean sea level.
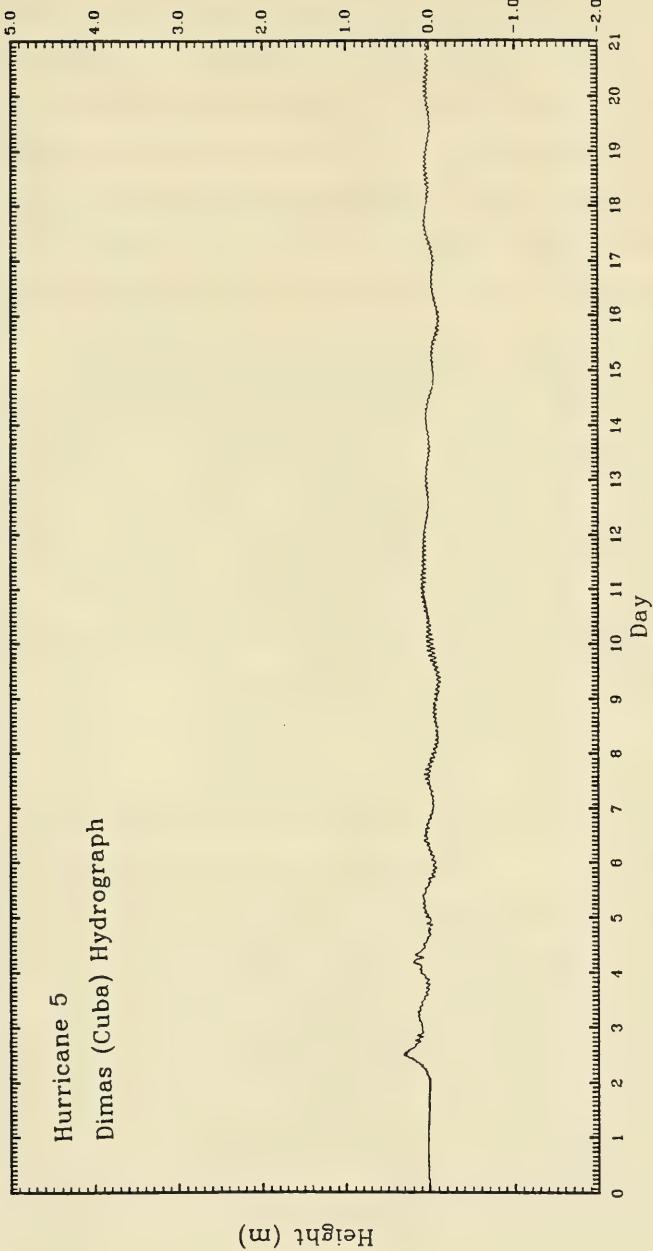
Fig. 99. Time sequence of water levels at Dimas (Cuba) obtained from the long term simulation of HUR5. The datum is mean sea level.

165

A simple geostrophic calculation using an instantaneous volume transport through Florida Strait at 1600 h on day 8 of 30×10^6 m^3/s and an average depth across the port of 950 m yield a northward surface gradient from Cuba of 0.2 m. A similar computation for the Yucatan Strait yields a surface gradient toward Campeche Bank of only 0.07 m. The surface height field is not available for comparison. However, using the mean water levels at Dimas and Key West as a rough representation of the north-south surface component of gradient reveals that the tilting of water surface across Florida Strait is on the order of 0.5 m. This result is much larger than that obtained from the simplified geostrophic calculation. It is quite possible that the current speed is not uniform across the ports. An estimate of the effect of current shear on the cross-port surface gradient by numerically integrating the geostrophic equation across the port was made. This integration is given by the relation

$$\eta_{j+1} = \eta_j + (\Delta y f U / g D_{j+\frac{1}{2}}) , \tag{79}$$

where U is the transport per unit width for each grid block across the Florida Strait and $D_{j+\frac{1}{2}}$ is the average depth for each block. Upon assuming uniform distribution of transport across the port, U is Q/W where Q is the total volume transport and W is the port width. Employing the same value of Q as in the previous calculation and taking the water level at Cuba (south of Key West) as zero yields a surface gradient between Key West and Cuba of 0.5 m. For the Yucatan Strait the tilting of water surface between Cuba and the east coast of Yucatan obtained from this computation is 0.26 m. Even though Q

166

is the same at both ports, Yucatan channel is much deeper than the Florida port so that the computed surface gradient is smaller. There is no hydrograph on the east coast of Yucatan for comparison in this case.

6. Results from related simulations

a) Variation of pressure drop

All the synthetic storms employed a constant pressure drop of 80 mb. As a sensitivity test of the model, simulations of HUR5 with a 40 mb (HUR5W) and a 120 mb (HUR5S) pressure drop were made. Maximum surges of 3.59 m and 9.35 m were generated in the simulations of HUR5W and HUR5S, respectively. Figure 100 displays the maximum surge as a function of pressure drop obtained from all simulations of HUR5. This result is consistent with Jelesnianski's (1972) inference that the peak surge is almost a linear function of the pressure drop.

Plots of η_G obtained from the HUR5W and HUR5S simulations are shown in Figs. 101 and 102, respectively. The maximum peak and the period of this oscillation are 0.2 m and 27 h for the weak storm and 0.6 m and 27 h for the intense storm.

Note that the HUR5W simulation yields a larger magnitude of η_G compared with HUR25 despite its smaller pressure drop. This implies that a major factor governing the magnitude of the η_G from these simulations is the differential wind-driven volume transport through Florida port and Yucatan Strait.

167
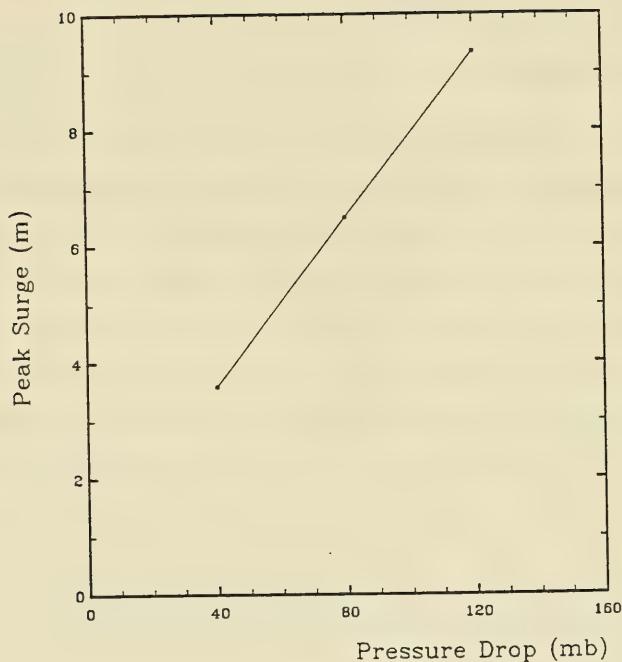
Fig. 100. Relationship between the maximum peak surge at the coast and the central pressure deficit obtained from three simulations of HUR5 with 40 mb, 80 mb and 120 mb pressure drop.
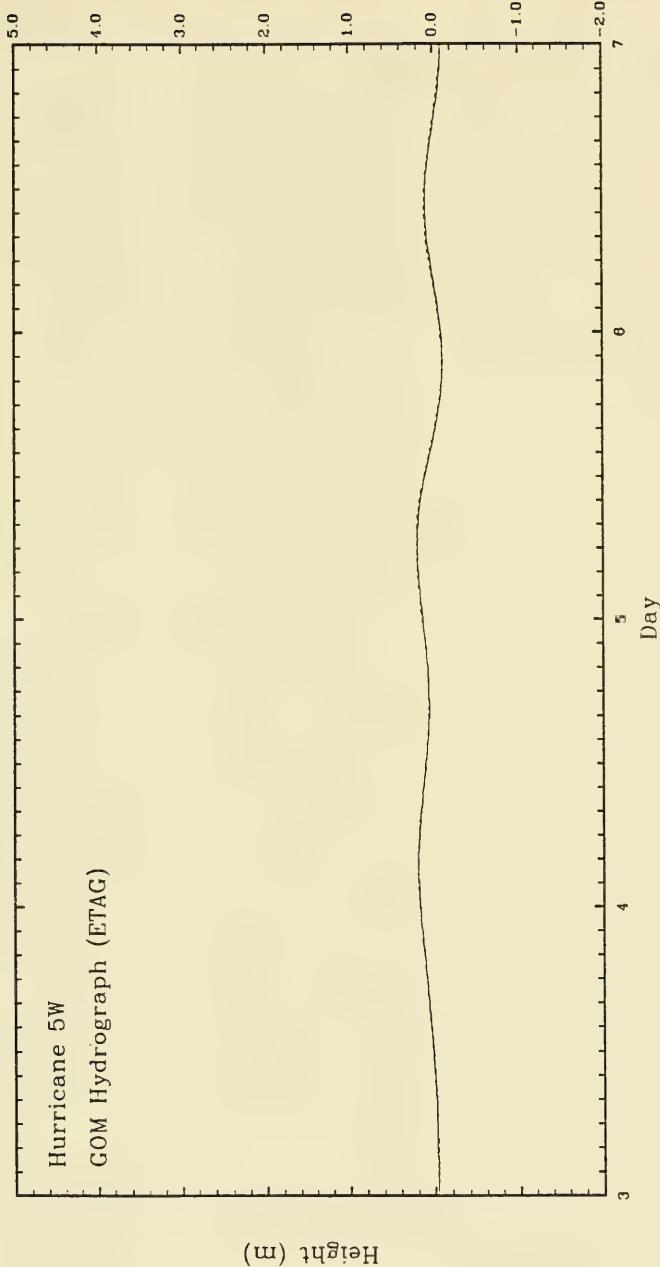
Fig. 101. Time sequences of the average water levels in the Gulf of Mexico, η_G, obtained from the simulation of HUR5 with 40 mb pressure drop (HUR5W). The solid line is computed by averaging water levels from every grid point in the Gulf at each time step. The dashed line is computed from the continuity equation. The datum is mean sea level.

169
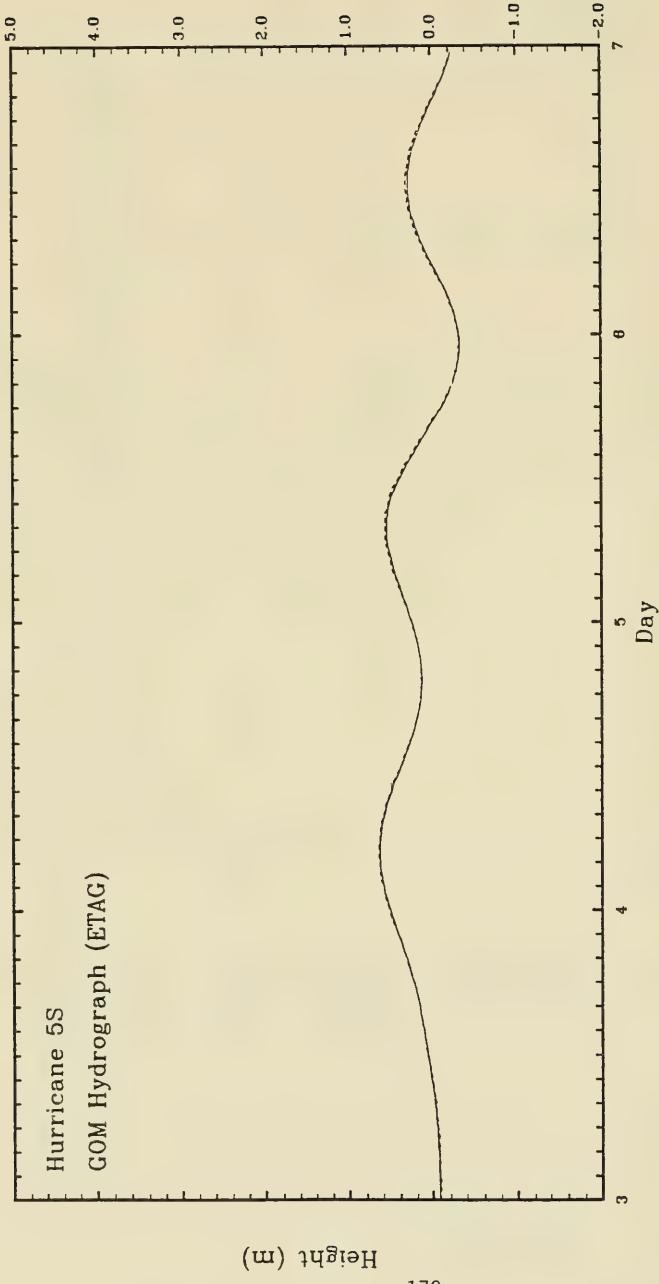
Fig. 102. Time sequences of the average water levels in the Gulf of Mexico, η_G, obtained from the simulation of HUR5 with 120 mb pressure drop (HUR5S). The solid line is computed by averaging water levels from every grid point in the Gulf at each time step. The dashed line is computed from the continuity equation. The datum is mean sea level.

170

b) Barotropic model

It is important to ascertain the effects of the baroclinic response in deep water on the maximum surge at the coast since both barotropic and baroclinic modes are coupled through the gradient terms, $\nabla(H_1/D)$. Therefore, an additional simulation of HUR5 was repeated which excluded the baroclinic mode.

A maximum peak surge of 6.42 m at grid point (14,46) was obtained from this simulation. This peak is only eight tenths of a centimeter lower than that obtained from the two mode simulation of this storm. Comparisons of the simulated hydrographs from the barotropic model and the original HUR5 reveal that the baroclinic response does not produce a significant contribution to the barotropic response on the shelf except at Key West, Naples and St. Petersburg. The solid and dashed lines in Fig. 103 and 104, respectively, represent the computed hydrographs obtained from the two mode and pure barotropic mode simulations at the indicated stations. The reason that this effect is visible on the Florida shelf rather than other locations may be due to a larger baroclinic transport (through the Florida strait) and a stronger coupling as a result of steeper slopes at the Florida shelf break.

As expected, the Gulf-wide oscillation as shown in Fig. 105 obtained from this simulation is only slightly different from that obtained from the two mode run.
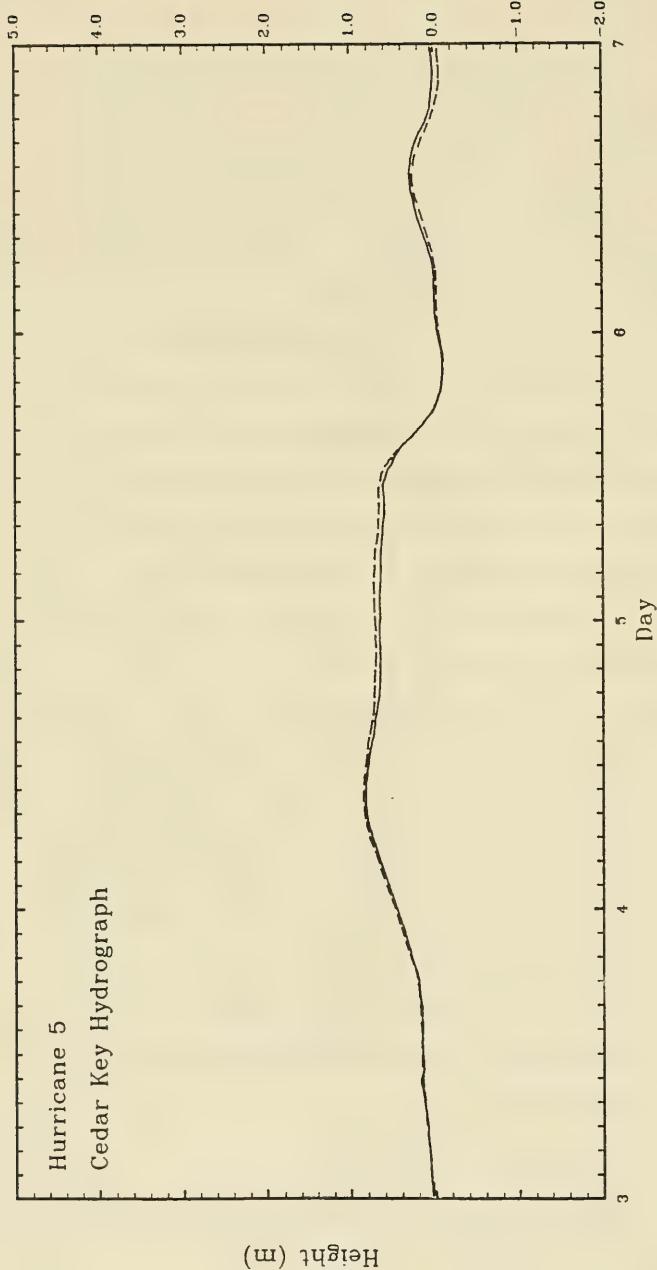
Fig. 103. Time sequences of water levels at Cedar Key obtained from the simulations of HUR5 (dashed) and the pure barotropic model of HUR5 (solid). The datum is mean sea level.
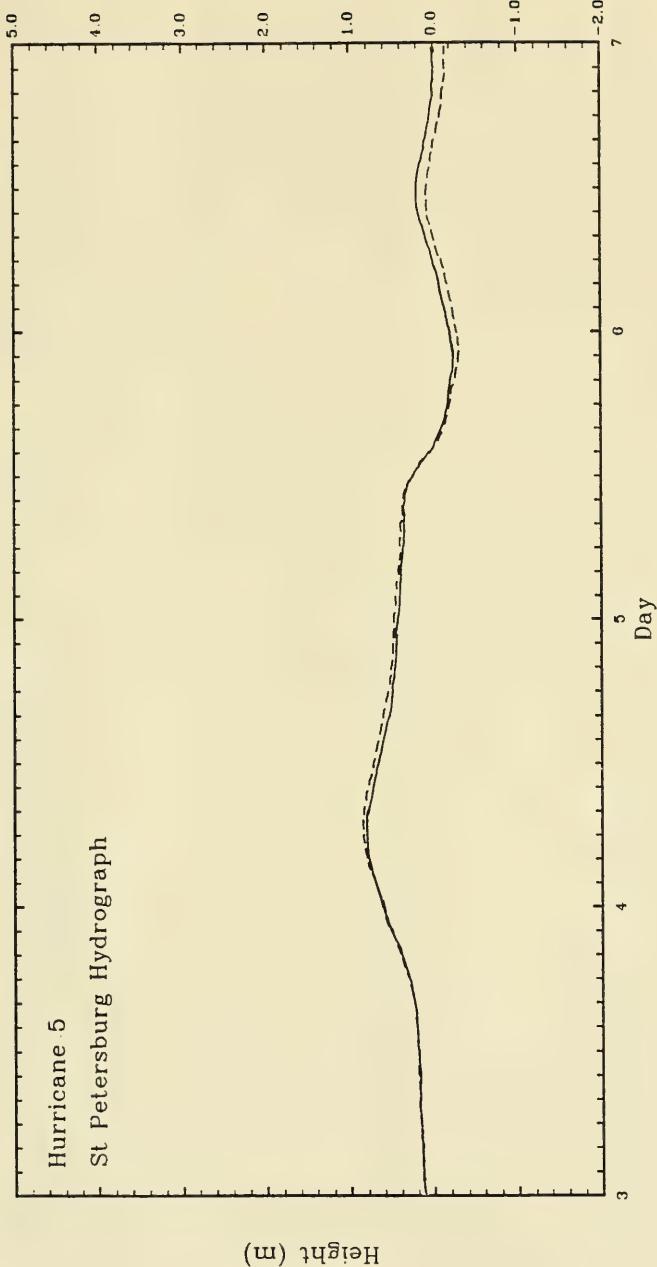
Fig. 104. Time sequences of water levels at St. Petersburg obtained from the simulations of HUR5 (dashed) and the pure barotropic model of HUR5 (solid). The datum is mean sea level.

173
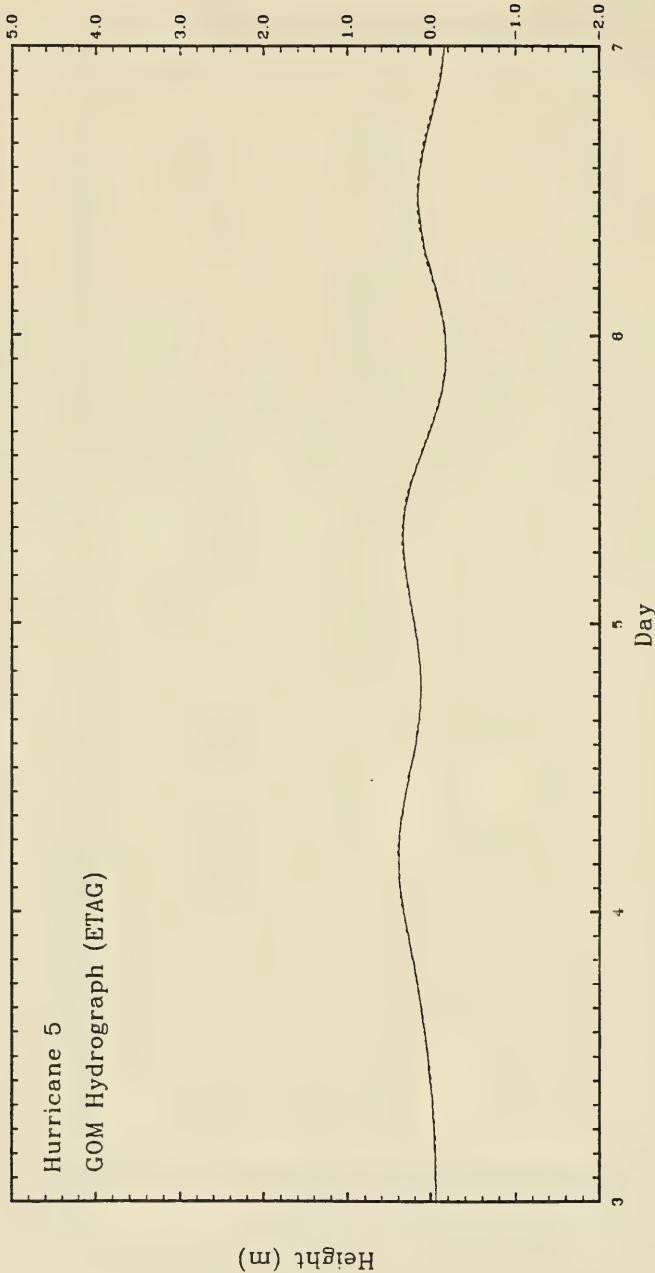
Fig. 105. Time sequences of the average water levels in the Gulf of Mexico, η_G, obtained from the simulation of the pure barotropic model of HUR5. The solid line is computed by averaging water levels from every grid point in the Gulf at each time step. The dashed line is computed from the continuity equation. The datum is mean sea level.

174

c) Radiation boundary condition

The effects of the open boundary condition employed in this study on η_G was of primary concern. In order to evaluate this effect, a pure radiation boundary condition was imposed in the simulations of HUR5, HUR23 and hurricane Allen. The names of these storms modified by (R) are used in the following discussions to distinguish them from their corresponding original simulations.

Figures 106 through 108 show the time histories of η_G obtained from the simulations of HUR5(R), HUR23(R) and hurricane Allen(R), respectively. Only the η_G signal obtained by averaging water levels in the Gulf is shown in the figures (note the changes in height scale). The radiation condition at the open boundaries effectively radiates η_G out of the Gulf. The peaks of η_G, sequentially, are 0.28 m, 0.14 m and 0.22 m for HUR5(R), HUR23(R) and hurricane Allen(R). The estimated e-folding times of the damping rate are 34 h for HUR5(R), 24 h for HUR23(R) and less than 10 h for hurricane Allen(R). The radiation condition not only drastically damps the η_G signal but also changes their periods. Reid and Whitaker (1981) experimentally determined the damping rate of the volume mode in the GOMT model to be 2.81×10^{-6} s^{-1} or an e-folding time of 2.6 days. The radiation condition employed in the GOMT model has a complex admittance coefficient in which the imaginary part governed the effective added mass of adjoining seas. The radiation condition employed in this study is a special case where only the real part of the admittance is considered. Exclusion of the imaginary part results in a much larger damping rate of the volume mode as found in this study. However, the
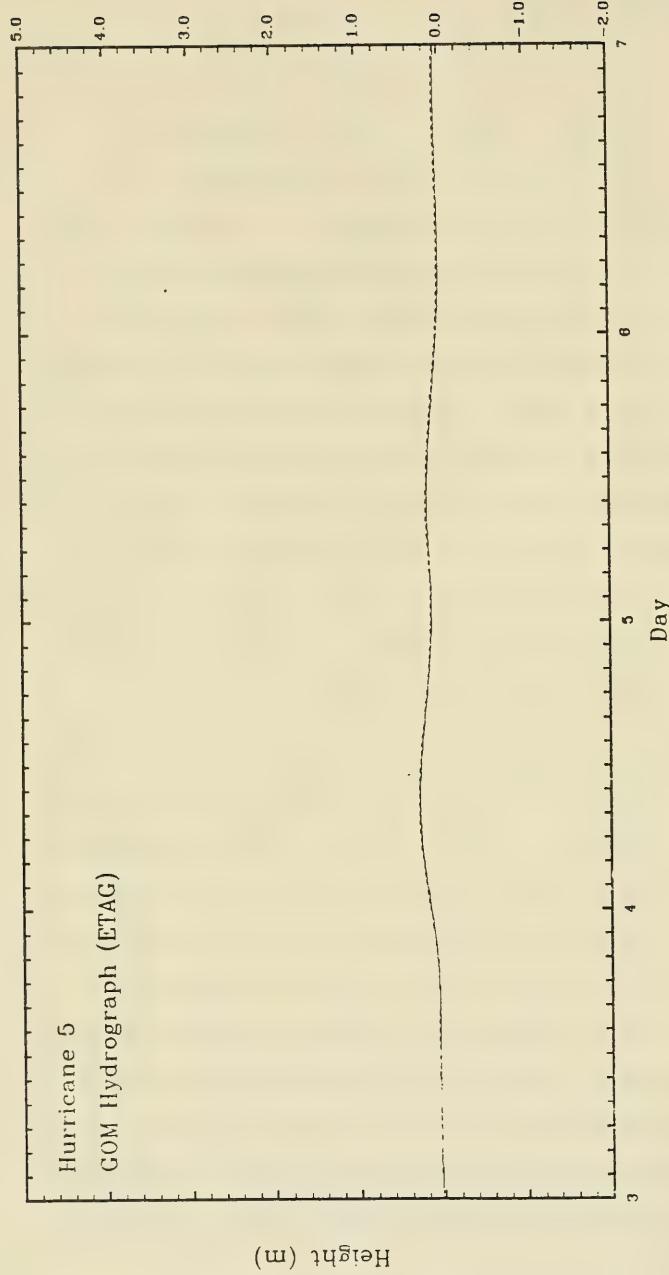
Fig. 106. Time sequences of the average water levels in the Gulf of Mexico, η_G, obtained from the simulation of HUR5 with radiation condition at the open boundaries. The solid line is computed by averaging water levels from every grid point in the Gulf at each time step. The dashed line is computed from the continuity equation. The datum is mean sea level.

176
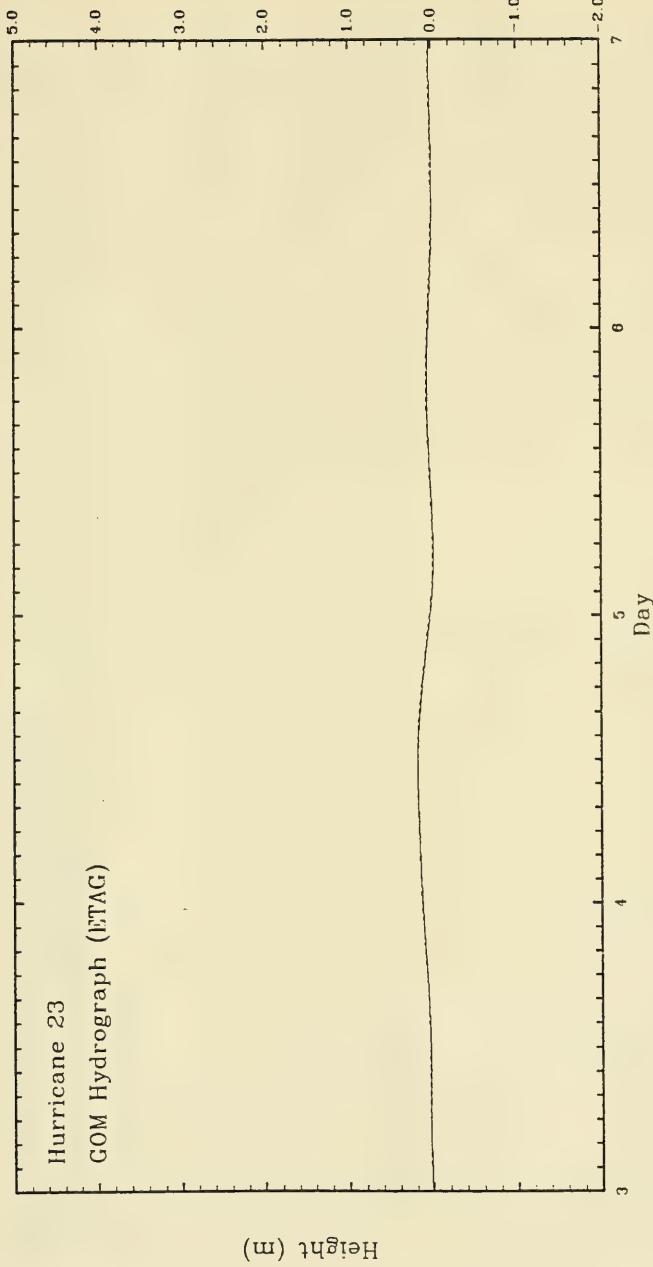
Fig. 107. Time sequences of the average water levels in the Gulf of Mexico, η_G, obtained from the simulation of HUR23 with radiation condition at the open boundaries. The solid line is computed by averaging water levels from every grid point in the Gulf at each time step. The dashed line is computed from the continuity equation. The datum is mean sea level.

177
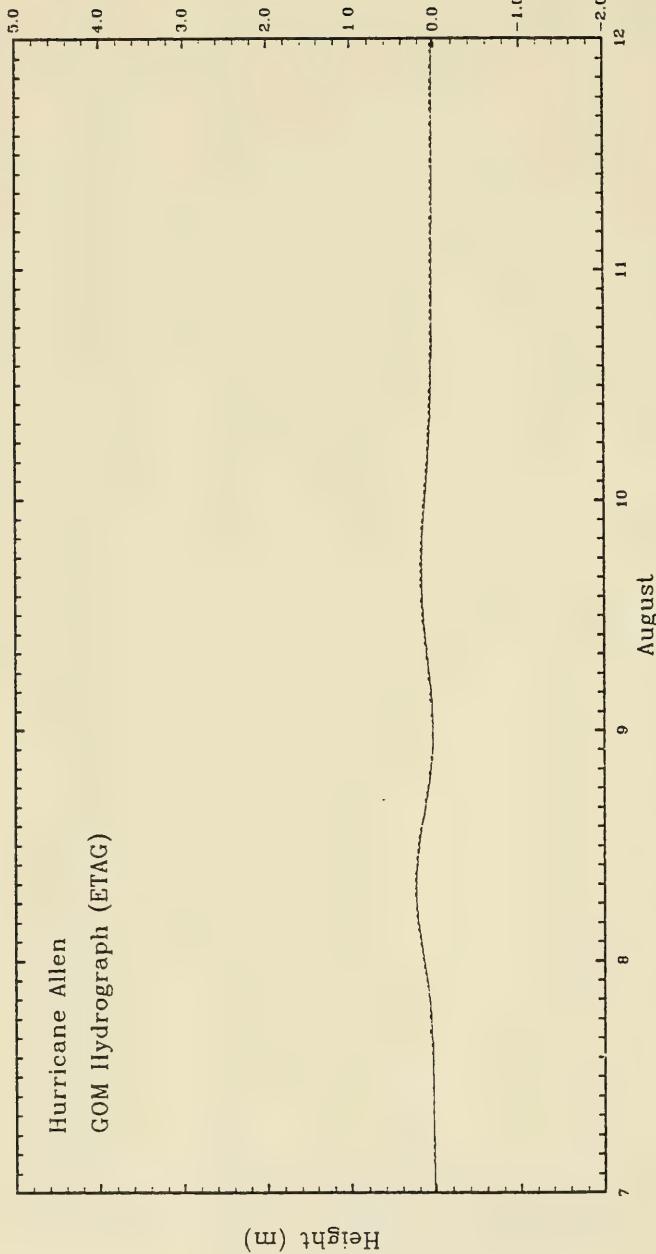
Fig. 108. Time sequences of the average water levels in the Gulf of Mexico, η_G, obtained from the simulation of hurricane Allen with radiation condition at the open boundaries. The solid line is computed by averaging water levels from every grid point in the Gulf at each time step. The dashed line is computed from the continuity equation. The datum is mean sea level.

178

initial perturbation of η_G before the maximum peak surge is retained, but is reduced on the order of 30 %. Changes in the maximum peak surge at the coast are shown in Table 3. The magnitudes of η_G ($|\eta_G|$), determined at the time of the maximum peak at the coast, are shown in column 5. The differences of $|\eta_G|$ between each pair of simulations are shown in column 6. The superscript plus or minus indicates whether $|\eta_G|$ obtained from the simulations with the radiation condition is larger or smaller with respect to the former result. The differences in $|\eta_G|$ are clearly responsible for the changes in maximum peak surge at the coast.

d) Limited area model

Results obtained from the simulations of the hurricanes of record and the synthetic storms strongly indicate close correlation between the generation of a simultaneous Gulf-wide oscillation and the net periodic volume transport through the ports. It is of interest, therefore, to determine whether η_G still exists in the absence of wind stress in the deep water, including Florida and Yucatan Straits. Therefore, simulations of HUR5, HUR23 and hurricane Carla were repeated with a modified wind field where the wind stresses are set to zero everywhere in the deep water (water depth greater than the upper layer thickness). The continental shelf regions of these modified HUR5, HUR23 and Carla resemble limited area coastal or shelf surge models. In the following discussion these models are referred to as limited area models and their designated names are followed by (L).

179

Table 3. Results of the simulations of HUR5, HUR23 and hurricane Allen with and without radiation boundary condition.

STORM	PEAK COAST (m)	PEAK η_G	RATIO OF PEAK η_G (m)	$\|\eta_G\|$ (m)	$\Delta\|\eta_G\|$ (m)
HUR5	6.50	0.40		0.35	
			0.70		0.20^-
HUR5(R)	6.31	0.28		0.15	
HUR23	8.52	0.23		0.10	
			0.74		0.10^+
HUR23(R)	8.61	0.14		0.20	
ALLEN	2.40	0.35		-0.10	
			0.69		0.20^+
ALLEN(R)	2.65	0.22		0.10	

.

180

The Gulf-wide oscillation is still excited in the absence of wind stresses in the deep water. The time sequence of the η_G response obtained from the simulation of HUR5(L) is shown in Fig. 109. The maximum peak of this signal is 0.2 m and the average period is 28 h. Magnitudes of η_G obtained from the simulations of HUR5 and HUR5(L) differ by a factor of 2. Neglecting the deep-water wind driven flow produces a dramatic drop of the total transport through the ports for HUR5(L) as compared to HUR5 (not shown). The volume transport through both Florida and Yucatan Straits obtained from HUR5(L) is caused by the tilting of the water surface toward storm center due to the atmospheric pressure.

Simulation of HUR23(L) yields an η_G response (Fig. 110) that is almost identical to that obtained from HUR23. Comparison of the time histories of the volume transports obtained from the two runs (not shown) reveals that the net periodic volume transports are about the same (6.6 x 10^6 m^3/s) at their first maxima. Figure 111 shows the gulf wide oscillation obtained from hurricane Carla(L) simulation which is again comparable to that obtained from the original hurricane Carla result. The initial positions of HUR5 and hurricane Carla appear to be a key factor in the almost duplicate η_G responses generated by the limited area model and the complete model. Both storms are initially located closer and more directly to the south of Yucatan Strait as compared to HUR5. The stronger atmospheric pressure gradient through Yucatan channel is apparently more effective in drawing water through this opening.
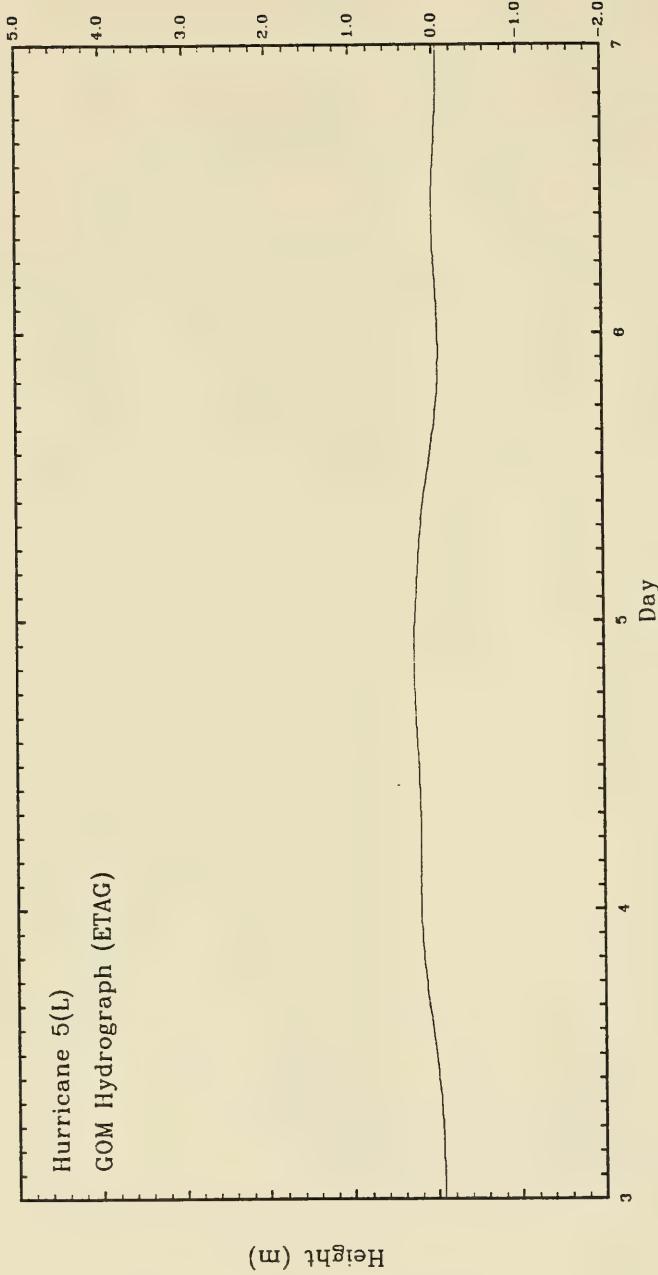
Fig. 109. Time sequences of the average water levels in the Gulf of Mexico, η_G, obtained from the simulation of HUR5(L). The solid line is computed by averaging water levels from every grid point in the Gulf at each time step. The dashed line is computed from the continuity equation. The datum is mean sea level.

182
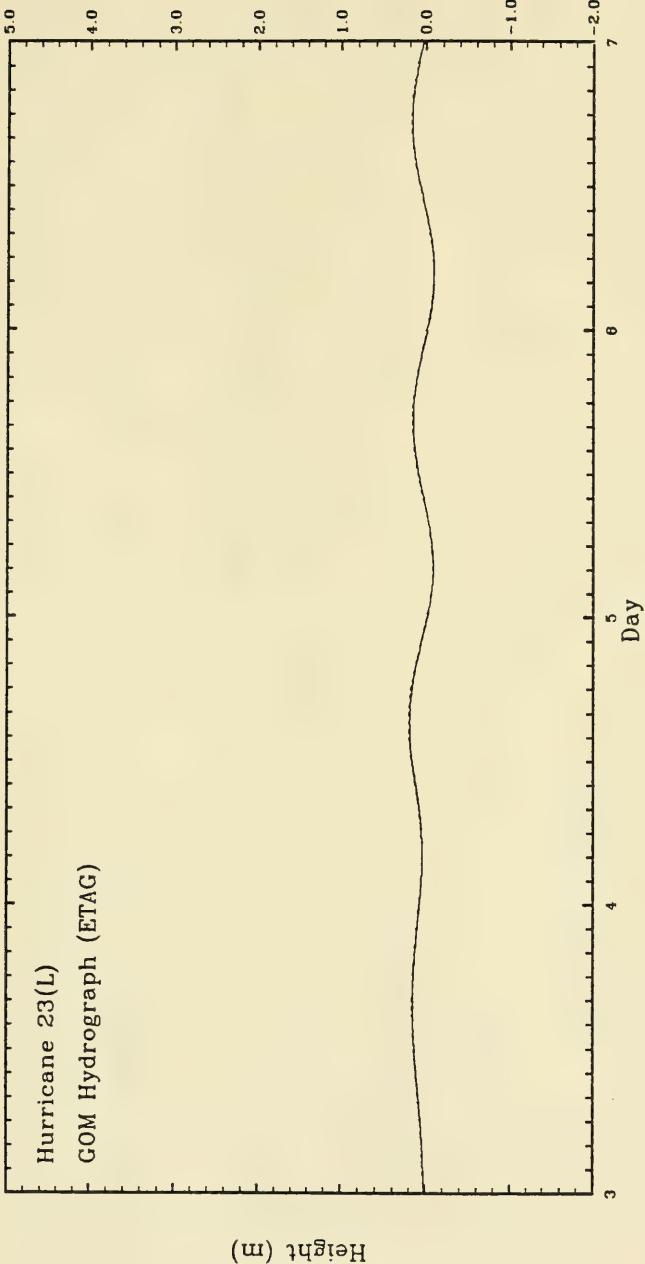
Fig. 110. Time sequences of the average water levels in the Gulf of Mexico, η_G, obtained from the simulation of HUR23(L). The solid line is computed by averaging water levels from every grid point in the Gulf at each time step. The dashed line is computed from the continuity equation. The datum is mean sea level.
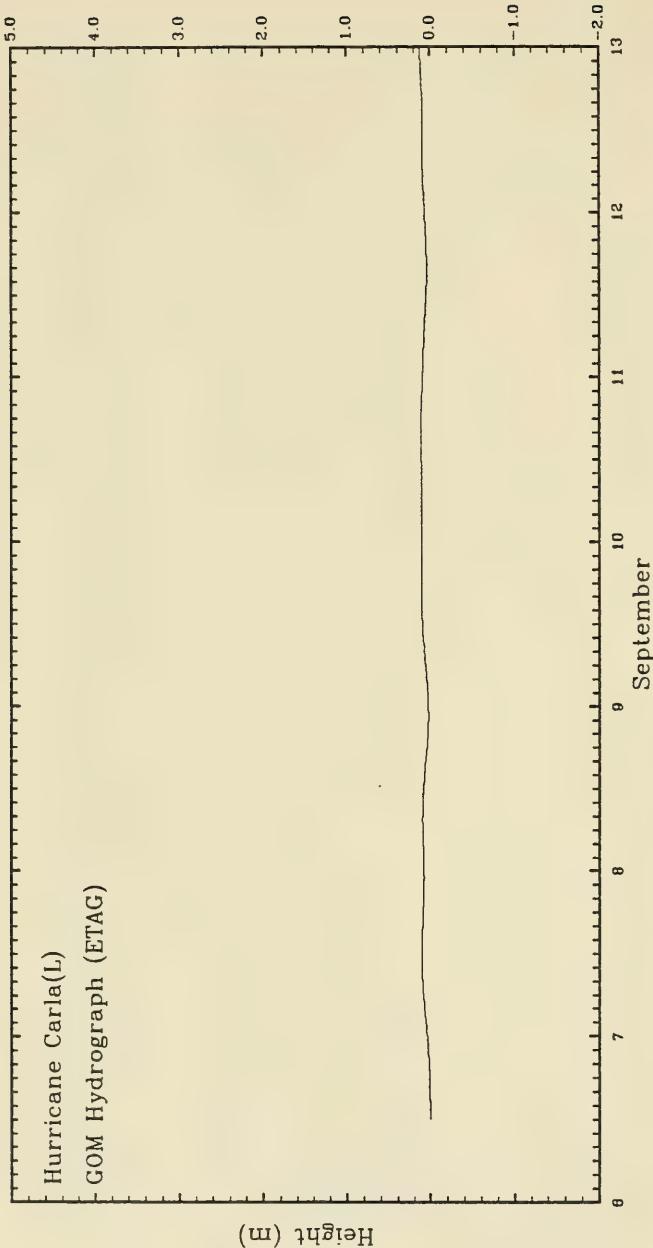
Fig. 111. Time sequence of the averaged water level in the Gulf of Mexico, η_G, obtained from the simulation of hurricane Carla(L). The datum is mean sea level.

184

Another important result found in the three limited area model simulations is the appreciable water surface elevation obtained at the edge of the shelf. This water level perturbation, excluding the inverted barometric height at the edge of the shelf, Ψ, reaches a maximum of 0.1 m - 0.3 m. In the simulations of the same storms with the actual wind field, the maximum Ψ increases to 0.7 m - 0.8 m. The maximum of Ψ and the peak surge at the coast, locations where the two peaks occur and the ratio of the two peaks obtained from all simulations are presented in Table 4.

It is important to note that the differences in the maximum peak surges at the coast between the full and limited area model simulations are comparable to the differences in the Ψ maxima. The presence of Ψ is important to a properly posed open boundary condition for limited area coastal surge models. Generally, these models neglect Ψ by specifying a constant water level, which is equivalent to the inverted barometric height, as the open boundary condition. As noted above, this condition might result in an underestimated maximum peak surge at the coast by a value comparable to the neglected Ψ. Another salient feature of Ψ pertaining to the consideration of open boundary conditions is the nonuniform distribution along the shelf break. Figs. 112 through 114 show profiles of Ψ obtained from the original versions of HUR5, HUR23 and hurricane Carla. The nonuniformity of these profiles implies that the effect of Ψ on the peak surge at the coast is different from one grid block to the other. This result ultimately prompted a question on specifying a constant water level along the shelf break as the

185

Table 4. Summary of peak surges at the coast and at the shelf break.

			R_{max} = 30 km						R_{max} = 60 km				
PATH	V_f (km/hr)	STORM	PEAK† COAST (m)	AT (I,J)	PEAK§ EDGE (m)	AT (I,J)	RATIO* (%)	STORM	PEAK† COAST (m)	AT (I,J)	PEAK§ EDGE (m)	AT (I,J)	RATIO* (%)
1	35	HUR2	4.20	14,46	0.69	11,40	16.43	HUR5	6.50	14,46	0.60	20,40	9.20
		-	-	-	-	-	-	HUR5L	5.85	16,47	0.18	12,40	3.08
	25	HUR1	3.52	14,46	0.30	11,40	8.52	HUR4	5.76	16,47	0.58	20,40	10.07
	15	HUR3	2.83	10,43	0.42	11,40	14.84	HUR6	4.71	14,46	0.75	20,40	15.92
2	25	HUR7	4.40	23,46	0.31	27,40	7.05	-	-	-	-	-	-
3	25	HUR13	5.81	37,49	0.49	37,44	8.43	-	-	-	-	-	-
4	35	-	-	-	-	-	-	HUR23	8.52	57,48	0.70	57,34	8.21
		-	-	-	-	-	-	HUR23L	8.16	57,47	0.34	50,45	4.17
	25	HUR19	6.22	54,48	0.47	57,34	7.56	HUR22	8.53	57,48	0.84	57,34	9.85
	15	-	-	-	-	-	-	HUR24	7.23	57,48	1.05	57,34	14.52
5	25	HUR25	5.40	16,47	0.30	33,40	5.56	-	-	-	-	-	-
	13	CARLA	3.19	8,42	0.59	10,39	18.50	NOTE: Hurricanes Carla and Allen do not					
		CARLAL	2.55	8,42	0.13	11,40	5.10	have R_{max} of 30 km.					
	30	ALLEN	2.40	4,33	0.38	8,39	15.83						

†, § are the same as in Table 2

* is the ratio between the peak surge at the shelf break and the peak surge at the coast.
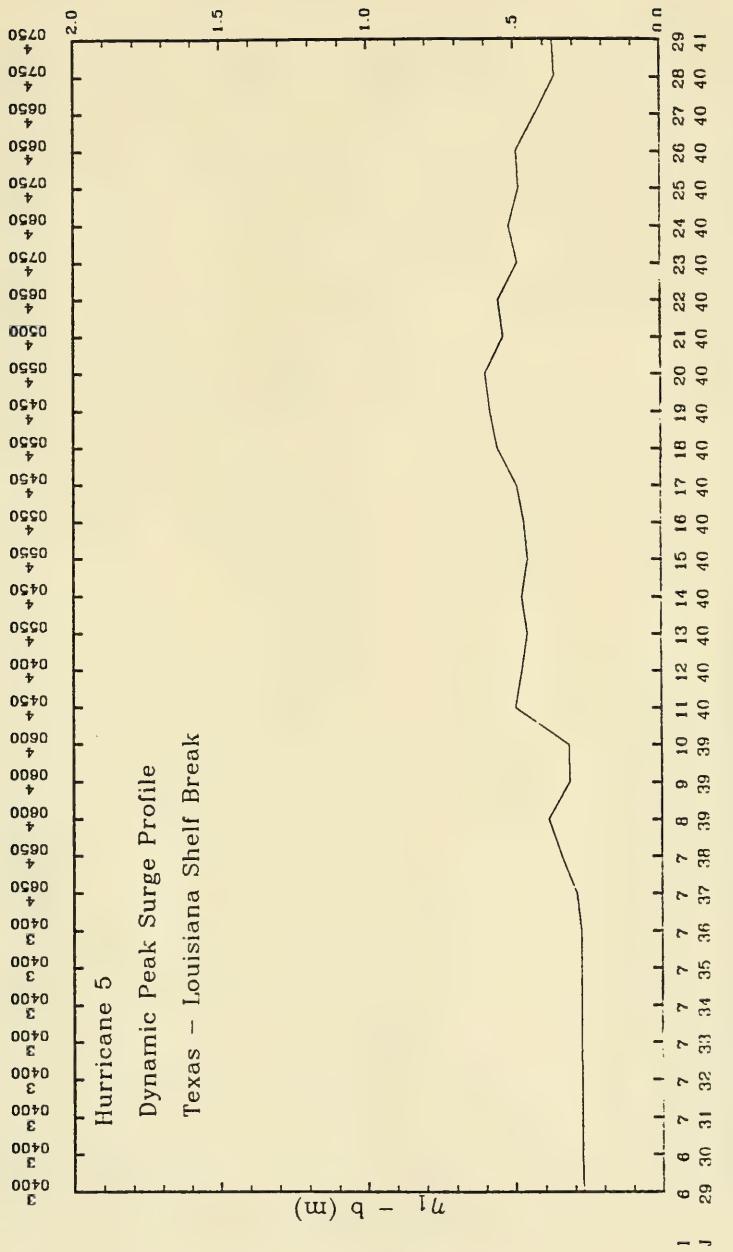
Fig. 112. Dynamic peak surge, Ψ, profile along shelf break obtained from the simulation of HUR5. Grid indicies are along the bottom and the time of peak Ψ is given by day and hour across the top. The datum is mean sea level.

187
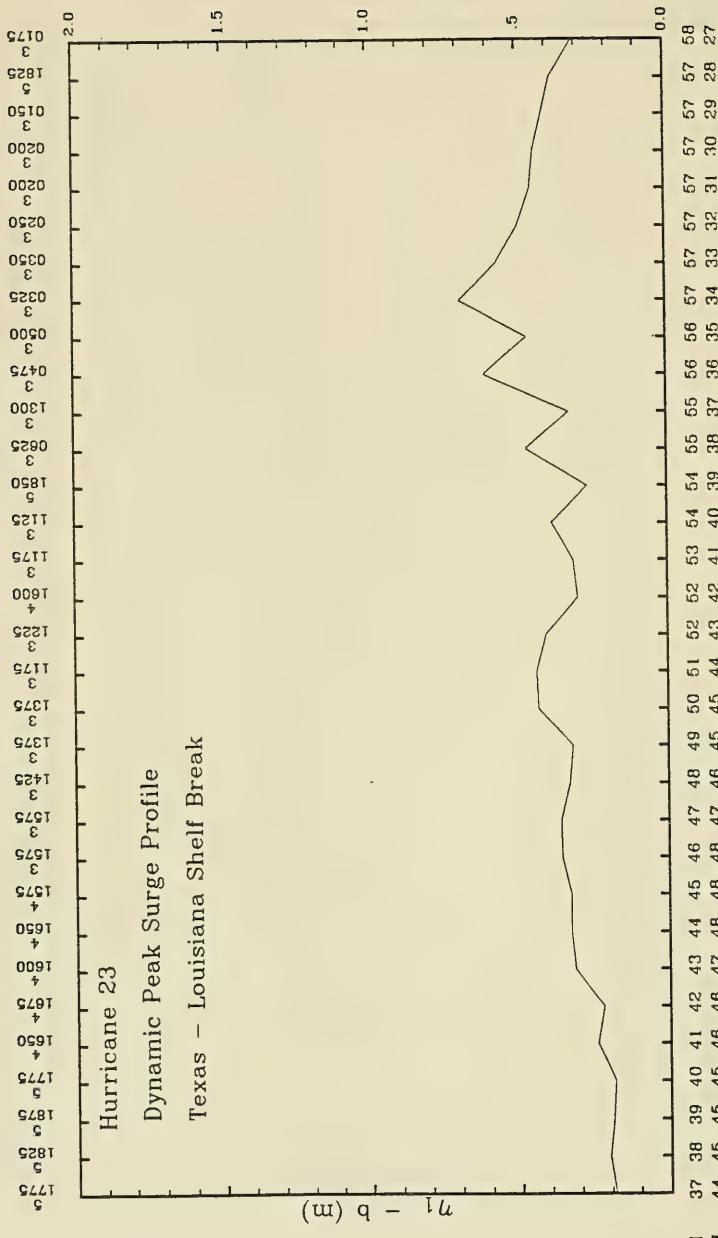
Fig. 113. Dynamic peak surge, Ψ, profile along shelf break obtained from the simulation of HUR23. Grid indicies are along the bottom and the time of peak Ψ is given by day and hour across the top. The datum is mean sea level.

188
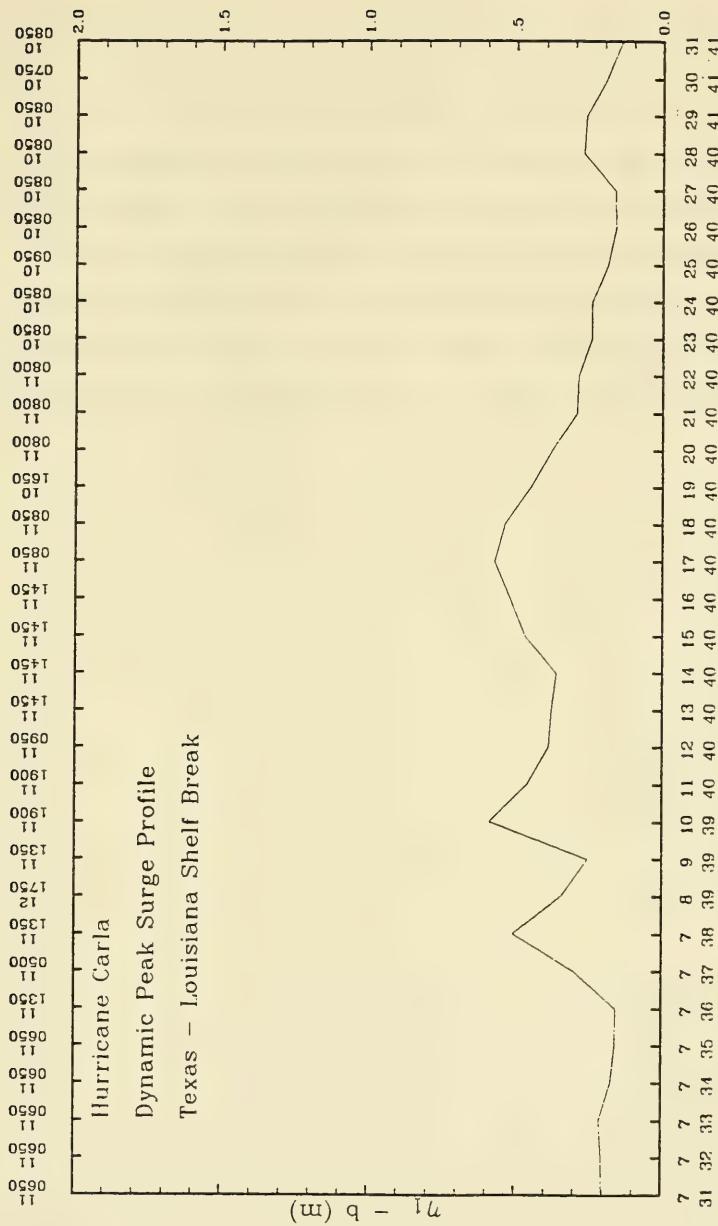
Fig. 114. Dynamic peak surge, Ψ, profile along shelf break obtained from the simulation of hurricane Carla. Grid indicies are along the bottom and the time of peak Ψ is given by day and hour across the top. The datum is mean sea level.

189

open boundary condition. The time at which the maximum Ψ occurs, shown at the top of the figures, introduces the time scale as another factor to be considered. In addition, the results shown in Table 4 indicate that the magnitude of Ψ decreases with increasing storm forward speed. Accordingly, there appears to be no simple resolution to the question of what is the proper open boundary condition for limited area coastal surge models. A possible pragmatic solution is to use the time sequence of water levels at each grid point along the shelf break obtained from an a priori simulation covering the entire basin.

CHAPTER V

SUMMARY AND CONCLUSIONS

A time-dependent, numerical, normal mode model portraying the linear (except for dissipation) physics of a two layer Gulf of Mexico has been developed, tested and verified. Comparisons of the numerical hydrographs and the known local responses produced by hurricanes Carla and Allen generally verify the barotropic surge response within the Gulf of Mexico. Those significant deviations which occur can be explained by unique gauge locations, insufficiently resolved model renditions of the coastline and bathymetry, and possible inaccuracies in the stipulated atmospheric forcing fields. The model was used to obtain the responses of the Gulf to a series of synthetic storms. These responses provided information which were used to answer basic questions on forerunner surges in the Gulf and related aspects of the surge prediction problem. These questions concerned the influence of baroclinic motions on the nearshore surge, the establishment of forerunners and the time and space scales of this initial rise in water level, and surge conditions at the shelf break.

Results from the simulations of the pure barotropic and the two mode models of HUR5 (a synthetic storm with 30 km radius of maximum wind translating at 35 km/h from the Cayman Sea through Yucatan Strait and landfalls at Corpus Christi, PATH1) demonstrate the insignificant contribution of the baroclinic responses to the water levels on the shelf areas. The maximum surges in particular are

191

scarcely affected by the baroclinic deep-ocean responses in spite of the fact that such modes contain significant energy. In addition, the initial rise of water level before the peak surge (which, by definition, is the forerunner)in the Galveston hydrographs obtained from the two versions of HUR5 show no visual differences. Based on these results, the baroclinic response is not important in the forerunner surge phenomenon.

The quasi-linear, coupled, normal mode model shows that the hurricane induced forerunner surge in the Gulf of Mexico is associated with a Gulf-wide oscillation of water level, η_G. The ubiquity of the η_G signal in the hydrographs from stations around the Gulf, except near Florida Strait, indicates that η_G is dominated by a volume (i.e., Helmholtz) mode. The Helmholtz mode is characterized by a relatively uniform amplitude and phase, except near the open ports where the amplitude and phase changes rapidly. The forerunner, therefore, has space scales comparable to the horizontal dimensions of the Gulf of Mexico.

Examination of the transport through the ports, particularly for the 21 day simulations for PATH1, reveal large and nearly equal amplitude but out-of-phase oscillations of about 6.5 day (156 h) period. Superimposed on the 6.5 day oscillations are smaller amplitude in-phase oscillations with a period of about 28 h. The out-of-phase transport implies that when the transport is in one port it is out of the other. It is the in-phase oscillations in transport which are associated with the Helmholtz mode in the Gulf. The long period out-of-phase oscillations in transport, on the other hand, are

associated with a quasi-geostrophic tilt of water level across the ports as well as a tilt from southeast to northwest across the Gulf. The 6.5 day period oscillations coincide with the natural modes on the west Florida shelf (Marmorino, 1982). The excitation of the out-of-phase transport and associated quasi-geostrophic tilt mode in the present model is due to out-of-phase wind forcing at the ports (as can be produced by the cyclonic circulation in those hurricanes which traverse the Cayman Sea). Observational evidence to confirm the existence of the 6.5 day mode in the actual Gulf is lacking (e.g., the Key West gauge records do not show clear evidence for the large amplitude 6.5 day oscillations which the model simulations for hurricane Allen or HUR5 produce). However, except for locations near the ports, the water level variations associated with the 6.5 day tilt mode are small (less than 0.1 m along the northern and western coast of the Gulf). Hence the quasi-geostrophic tilt mode is probably not important with respect to forerunners in the northern and western parts of the Gulf.

Close examination of the η_G time sequences for the long term simulations for PATH1 show that, in addition to the presence of the Helmholtz mode, a period of about 3.4 days is also present. But there is very little evidence of the 6.5 day tilt mode in η_G. The 3.4 day mode in fact shows up in the time history of the spatial mean water level for the Cayman Sea. Some observational evidence for such a mode of oscillation exists for the Gulf (Halper, 1984, Kelly, 1985, Kirwan et al., 1984). The relative excitation of these modes during the forcing stage by hurricanes depends upon the path, the storm

193

scale and intensity, and to a lesser extent on the translational speed of the hurricane. In general, the η_G during the first few days after the hurricane enters the Gulf consists of three components. The first two components (i.e., the Helmholtz mode and the 3.4 day Gulf-Cayman mode) are associated with the volume transport through the ports. The third component is a directly forced response associated with the spatial average value of b (the inverted barometer term) over the Gulf. PATH1 tends to give the largest peak η_G, particularly for larger radius storms (compare HUR1 and HUR4 results).

Results from the limited area model and the full model disclose that both the central pressure deficit and the wind induced transports through the ports can excite the Helmholtz mode. However, the relative importance of the two forcing fields in generating η_G depends upon the storms' paths and their evolution. The almost identical η_G obtained from the full and limited area models of hurricane Carla and HUR23 show that the atmospheric pressure gradient through Yucatan Strait was more important in the generation of η_G than the wind forcing. In contrast, the small η_G response in the absence of wind in deep water for HUR5(L) implies that in this case wind forcing was the major factor in generating η_G.

The average periods of the Helmholtz mode from this study are in the range of 25-32 hours. Platzman (1972) obtained a free Helmholtz mode with a period of only 21.2 hours. This difference in periods is due to the fact that η_G is composed of both forced and free components. The average period of 28 hours obtained from the 21 day

simulation of HUR5 was estimated during the later stage of the simulation for which the forced component of η_G probably has been damped out. The variation of the period of η_G, from one simulation (of the original synthetic storms HUR1 through HUR25) to the other may be caused by the variation of the period of the forced component which is subjected to different forcing. There is some indication that the period of η_G is smaller for a faster moving storm. Based on the Gulf mean tidal response in the diurnal band, the GOMT model of Reid and Whitaker (1981) used a 28.5 hour Helmholtz mode. Their volume mode period was adjustable because the radiation boundary condition employed in the GOMT model effectively takes into account the added mass of the Cayman Sea (including the Atlantic Ocean) by means of a complex ocean impedance. The 28.5 hour period used by Reid and Whitaker (1981) is close to the average period of the free component of η_G obtained from this study.

It is likely that Gulf hurricanes in general elicit the Helmholtz mode and the longer period modes, but only certain storms generate a forerunner. With the definition of a forerunner as the initial rise of water level before the peak surge, storms traversing PATH4 do not generate forerunner surges but certainly excite η_G. The synthetic storm HUR25 (along PATH5) serves as another example of the situation where η_G exists but with no forerunner. The presence of a forerunner in local hydrographs is therefore dependent upon the path, but is also dependent on the landfall position and the time of the excitation of η_G relative to the peak surge. This would explain why every hurricane of record does not have an associated forerunner.

For example, a fast moving hurricane, which is generated inside the Gulf might have an associated initial peak of η_G which is nearly in phase with the primary shelf surge.

A supplementary question addressed in the present study concerns the surge behavior at the shelf break. This is at least as important as the forerunner behavior for limited area models. In many applications of surge models the domain of the model is limited to a section of the continental shelf extending seaward from shore to the shelf break (about 200 m depth). A common boundary condition employed in such limited area models is to set the water level (η) equal to the local value of b for a given time during the traverse of the hurricane through the model domain. The present study in which the whole Gulf of Mexico (and part of the Cayman Sea) is modeled, shows that the water level at the shelf break can depart significantly from b at the shelf break. Moreover, this departure $(\eta-b)_s$ has a behavior differing from that of η_G and generally of larger magnitude. For example, large scale (R_{max} = 60 km) hurricane simulations along PATH4 yield larger values of $(\eta-b)_s$ than do those along PATH1; this is just the opposite behavior of η_G for these two paths.

In order to gain some further insight with respect to the shelf break condition, three hurricane runs (HUR5, HUR23 and Carla) were repeated with the winds turned off in the deep region of the Gulf and Cayman Sea (i.e., for depths greater than H_1). This is equivalent to having a limited area shelf model (including all shelves in the system) but allowing wave energy to radiate into the deep Gulf.

Comparison of the η_s (i.e., at the shelf break) from these runs with their counterparts for the fully forced model shows that there remains a significant difference (of order of 0.4 m) in the peak values.

The primary conclusions of this study can be summarized as follows:

(1) The surge on the shelf including the forerunner is primarily a barotropic response; very little of the baroclinic energy generated within the deep water regions is transmitted onto the shelf.

(2) The forerunner, when it occurs, is associated primarily with the Gulf-wide modes contained in η_G (the spatial average of the Gulf water level at a given time); this is a volume mode which exhibits periods of about 28 hours and 3.4 days.

(3) Forerunners are always associated with η_G, but not all hurricanes which excite η_G have an associated forerunner. Regardless of whether or not forerunners exist, η_G can, if properly phased, affect the magnitude of the peak surge.

(4) Limited area shelf models (at least within the Gulf of Mexico), which employ the seaward boundary condition $\eta = b$ (or the generalization of this which allows outward radiation of free waves) will always underestimate the peak surge at shore; the underestimate can amount to as much as 10 percent.

(5) A Gulf-wide quasi-geostrophic tilt mode of about 6.5 day
period is found in the model superimposed on the volume
mode, but verification of this from observations is lacking.

The above conclusions are based on a quasi-linear, two-layer
model of the Gulf of Mexico and a portion of the Cayman Sea. The
model used a grid size of 15' in latitude and longitude and allowed
for a variable Coriolis parameter. The lack of non-linear advection
and the *ad hoc* conditions at the open boundaries of the Cayman Sea
and Florida Strait should be borne in mind, particularly with regard
to conclusion (5). Long period, quasi-geostrophic (planetary) modes
are known to exist in the ocean; however, their spatial structure
and behavior is known to be sensitive to open boundary conditions and
to non-linear phenomena such as advection of vorticity (which is not
admitted in the present model). Indeed, the effect of the strong
quasi-steady Loop Current within the eastern Gulf is missing in the
present linear model. Regardless of these limitations, it is felt
that conclusions (1) through (4) remain valid.

REFERENCES

Buffler, R.T., S.D. Locker, W.R. Bryant, S.A. Hall and D.H. Pilger Jr., 1984: Ocean Margin Drilling Program Regional Atlas Series, Gulf of Mexico, Atlas 6, *Marine Sci. Internat.*, *Woods Hole*, 36 pp.

Chang, S.W. and R.A. Anthes, 1978: Numerical simulations of the oceans's nonlinear baroclinic response to translating hurricanes. *J. Phys. Oceanogr.*, *8*, 468-480.

Cline, I.M., 1920: Relation of changes in storm tides on the coast of the Gulf of Mexico to the center and movement of Hurricanes. *Mon. Wea. Rev.*, *48*, 127-145.

Dunn, G.E. and staff, 1962: The hurricane season of 1961. *Mon. wea. Rev.*, *90*, 107-119.

Geisler, J.E., 1970: Linear theory of the response of a two layer to a moving hurricane. *Gephys. Fluid Dyn.*, *1*, 249-272.

Halper, F.B., 1984: The effect of storms on the sediment resuspension and transport on the outer continental shelf, Northwest Gulf of Mexico. Ph.D. Dissertation, *Dep. Oceanogr.*, *Texas A&M University.*, 131 pp.

Ho, F.P. and J.F. Miller, 1980: Pertinent meteorological data for Hurricane Allen of 1980. *NOAA Tech. Rep. NWS-32*, Silver Spring, MD, 50 pp.

Holland, G.J., 1980: An analytic model of the wind and pressure profiles in hurricanes. *Mon. Wea. Rev.*, *108*, 1212-1218.

Ichiye, T., 1955: On the variation of ocean circulation (V). *Geophys. Mag.* (Tokyo Japan), *26*, 283-342.

————, H.H. Kuo and M.R. Carnes, 1973: Assessment of currents and hydrography of the Eastern Gulf of Mexico. *Contri. 601, Texas A&M University.*

Jelesnianski, C.P., 1972: SPLASH (Special Program to List Amplitudes of Surges from Hurricanes) I. Landfall Storms. *NOAA Tech. Memo. NWS TDL-46*, Silver Spring, MD, 52 pp.

Kelly, F.J., 1985: Offshore oceanographic and environmental monitoring services for the Strategic Petroleum Reserve, II, Annual Rep. for the Bryan Mound site from Sept. 1983 through Aug. 1984, *Texas A&M University*, 434 pp.

Kirwan, A.D., W.J. Merrell Jr., J.K. Lewis and R.E. Whitaker, 1984:
    Langrangian observations of an anticyclonic ring in the Western
    Gulf of Mexico. *J. Geophys. Res.*, *89*, 3425-3438.

Lawrence, M.B. and J.M. Pelissier, 1981: Atlantic hurricane season of
    1980. *Mon. Wea. Rev.*, *109*, 1567-1582.

Leipper, D.F., 1967: Observed ocean conditions and Hurricane Hilda,
    1964. *J. Atmos. Sci.*, *24*, 182-196.

Leendertse, J.J., 1967: Aspects of a computational model for long
    period water wave propagation. *The Rand Coporation, Santa Monica,
    RM-5294-PR*, 165 pp.

Marmorino, G.O., 1982: Wind-forced sea level variability along the
    West Florida Shelf (Winter, 1978). *J. Phys. Oceanogr.*, *12*, 389-405.

Miyasaki, M., 1963: A numerical computation of the storm surge of
    Hurricane Carla in 1961 in the Gulf of Mexico. *Tech. Rep. 10, Dep.
    Geophys. Sci. University of Chicago*, 61 pp.

Muller, P. and C. Frankignoul, 1981: Direct Atmospheric forcing of
    geostrophic eddies, *J. Phys. Oceanogr.*, *11*, 287-308.

Platzman, G.W., 1972: Two dimensional free oscillations in a natural
    basin. *J. Phys. Oceanogr.*, *12*, 117-138.

Redfield, A.C. and A.R. Miller, 1957: Water level accompanying
    Atlantic coast hurricanes. *Meteo. Mono.*, *2*, 1-23.

Reid, R.O., and B.R. Bodine, 1968: Numerical model for storm surges
    in Galveston Bay. *Proc. ASCE, J. Waterway and Harbors Div.*, *94*,
    WW1, paper 5805, 33-57.

————— and R.E. Whitaker, 1981: Numerical model for astronomical
    tides in the Gulf of Mexico. *Unpubl. Rep.* submitted to *U.S. Army
    Waterways Experiment Station* under contract *DACW39-79-C-0074*.

Saylor, J.H., J.C. Huang and R.O.Reid, 1980: Vortex modes in southern
    Lake Michigan. *J.Phys. Oceanogr.*, *10*, 1814-1823.

Schwerdt, R.W., F.P. Ho and R. Watkins, 1979: Meteorological criteria
    for standard project hurricane and probable maximum hurricane wind
    fields, Gulf and East Coast of the United State. *NOAA Tech. Rep.
    NWS-23*, Silver Spring, MD, 317 pp.

Stevenson, R.E. and R.S. Armstrong, 1965: Heat loss from the waters
    of the Northwest Gulf of Mexico during Hurricane Carla. *Geophys.
    Internat. (Mexico City, Mex.)*, *5*, 49-57.

Veronis, G. and H. Stommel, 1956: The action of variable wind stress *on a stratified ocean*. J. Mar. Res., 15, *43-75*.

Wanstrath, J.J., 1975: Storm surge simulation in transformed coordinates. Ph.D. Dissertation, *Dep. Oceanogr., Texas A&M University*, 190 pp.